SANDIA REPORT
SAND2014-0669
Unlimited Release
Printed February 2014

Geomechanical Analysis to Predict the Oil Leak at the Wellbores in Big Hill Strategic Petroleum Reserve

Byoung Yoon Park

Prepared by
Sandia National Laboratories
Albuquerque, New Mexico 87185 and Livermore, California 94550

Sandia National Laboratories is a multi-program laboratory managed and operated by Sandia Corporation, a wholly owned subsidiary of Lockheed Martin Corporation, for the U.S. Department of Energy's National Nuclear Security Administration under contract DE-AC04-94AL85000.

Sandia National Laboratories

Issued by Sandia National Laboratories, operated for the United States Department of Energy by Sandia Corporation.

Printed in the United States of America. This report has been reproduced directly from the best available copy.

Available to DOE and DOE contractors from
U.S. Department of Energy
Office of Scientific and Technical Information
P.O. Box 62
Oak Ridge, TN 37831

Telephone: (865) 576-8401
Facsimile: (865) 576-5728
E-Mail: reports@adonis.osti.gov
Online ordering: http://www.osti.gov/bridge

Available to the public from
U.S. Department of Commerce
National Technical Information Service
5285 Port Royal Rd.
Springfield, VA 22161

Telephone: (800) 553-6847
Facsimile: (703) 605-6900
E-Mail: orders@ntis.fedworld.gov
Online order: http://www.ntis.gov/help/ordermethods.asp?loc=7-4-0#online

SAND2014-0669
Unlimited Release
Printed February 2014

Geomechanical Analysis to Predict the Oil Leak at the Wellbores in Big Hill Strategic Petroleum Reserve

Byoung Yoon Park

Geomechanics Department
Sandia National Laboratories
P.O. Box 5800
Albuquerque, NM 87185-MS0751

Abstract

Oil leaks were found in wellbores of Caverns 105 and 109 at the Big Hill Strategic Petroleum Reserve site. According to the field observations, two instances of casing damage occurred at the depth of the interbed between the caprock bottom and salt top. A three dimensional finite element model, which contains wellbore element blocks and allows each cavern to be configured individually, is constructed to investigate the wellbore damage mechanism. The model also contains element blocks to represent interface between each lithology and a shear zone to examine the interbed behavior in a realistic manner. The causes of the damaged casing segments are a result of vertical and horizontal movements of the interbed between the caprock and salt dome. The salt top subsides because the volume of caverns below the salt top decrease with time due to salt creep closure, while the caprock subsides at a slower rate because the caprock is thick and stiffer. This discrepancy yields a deformation of the well. The deformed wellbore may fail at some time. An oil leak occurs when the wellbore fails. A possible oil leak date of each well is determined using the equivalent plastic strain failure criterion. A well grading system for a remediation plan is developed based on the predicted leak dates of each wellbore.

ACKNOWLEDGMENTS

This research is funded by SPR programs administered by the Office of Fossil Energy (FE) of the U.S. Department of Energy.

Dr. Courtney G. Herrick (SNL, Dept. 6211) provided technical reviews and Dr. David J. Borns (SNL, Dept. 6912) and Dr. Moo Y. Lee (SNL, Dept. 6914) provided management reviews. This report has been improved by these individuals.

CONTENTS

FIGURES

TABLES

NOMENCLATURE

bbl	barrels
BH	Big Hill
CPU	Central Processing Unit
DM	Dyn McDermott
DOE	Department of Energy
D-P	Drucker-Prager
EPQS	Equivalent Plastic Strain
FEM	Finite Element Method
ID	Inside Diameter
MMB	Million Barrels
MSC	Multi-Sensor Caliper
OD	Outside Diameter
RF	Reduction Factor
SMF	Structural Multiplication Factor
SNL	Sandia National Laboratories
SPR	Strategic Petroleum Reserve
UTM	Universal Transverse Mercator
WIPP	Waste Isolation Pilot Plant
WH	West Hackberry

Intentionally Blank

1. INTRODUCTION

1.1. Background

The US Strategic Petroleum Reserve (SPR) stores crude oil in 62 caverns located at four different sites in Texas and Louisiana. The reserve currently contains over 700 million barrels (MMB). Most of the caverns were solution mined by the Department of Energy (DOE). Oil leaks were found in the wells of Big Hill (BH) Caverns 105B and 109B by interpreting Caveman[†] pressure data from Dyn McDermott[‡] [Ehgartner, 2010; Ehgartner 2011]. The Well 105B leak started after December 3, 2009, and had progressed to 8600 barrels (bbl) on May 14, 2010 before the leak was brought under control by reducing cavern pressure. The rate increased both episodically and exponentially to over 150 bbl per day. The location of the leak is at about 1636 ft below the surface, which is close to the interbed between the caprock and the salt dome. The Well 109B leak started on October 8, 2010. The total amount of oil leaked is estimated to be 2700 bbl. This occurred over an 88 day period resulting in an average leakage rate of 31 bbl per day. The location of the leak is at about 1630 ft below the surface at the joint. These leaks at Wells 105B and 109B could be caused by interbed movement induced by cavern volume closure due to salt creep.

1.2. Previous Work

This report summarizes a series of three-dimensional structural simulations of the BH SPR wellbores. Park and Ehgartner [2012] developed three-dimensional finite element model, which allows each cavern to be configured individually, to investigate shear and vertical displacements across the interbed at the center of each cavern. The model contained interbeds between each lithologic unit and a shear zone to examine the interbed behavior in a realistic manner. It is hypothesized that well casing damage at the interbed would be caused by large scale salt rock mass movements brought about by cavern volume closure. The results from that analysis indicated that the casings of Caverns 105 and 109 failed, respectively, by shear stress that exceeded the casing shear strength due to the horizontal movement of the top of salt relative to the caprock, and tensile stress due to the downward movement of the top of salt from the caprock. However, that model did not consider the stiffness of the well casings which would impede the movement of the top of the salt dome. That model did not calculate the resultant displacement of the salt dome top relative to the caprock bottom either, i.e. the horizontal and vertical displacements were calculated separately. For a more realistic simulation, two new models were constructed for this study: another global model which includes representations of the wellbore casings for all the caverns to calculate large-scale displacements, and a single-cavern wellbore model to evaluate the effect of those displacements on the as-built casing designs. In this report, the model and the analyses results from the global model are described.

---

† Cavern pressure monitoring program developed by Sandia National Laboratories (SNL).

‡ Petroleum Operations Company of New Orleans to maintain the readiness of the SPR's four crude oil storage facilities in Louisiana and Texas.

1.3. Approach

The advanced model in this report is a full 3-D rendering of the site and includes the lithologic interfaces and the fault, needed to simulate the wellbore motion between the caprock and the salt dome. The new global model considers actual geometries and locations of fourteen SPR caverns and salt dome interfaces between two caprock lithologies, caprock and salt dome, dome and surrounding rock, and a shear zone in the overburden and caprock layers. In addition, fourteen simplified wellbore blocks are included in the model. The equivalent plastic strain (EQPS) of the each wellbore in the interbed between caprock and salt dome will be calculated and compared to the field data. The evolution of the EQPS of each wellbore will be investigated.

To figure out how the wellbore impedes the movement of the salt dome top, the analyses results from two global models with/without the wellbore element blocks will be compared. This comparison will show whether the sophisticated global model including wellbore blocks needs to be constructed for other SPR site simulations.

2. MODEL DESCRIPTION

2.1. Assumptions

In any numerical simulation of physical processes it is frequently necessary to invoke a number of assumptions which render the analysis tractable. Analyses involving geologic materials are well known to be very challenging due to the extreme variability of rock quality (e.g. degree of fracturing) and the inability to fully characterize the in-situ response of the rock when subjected to events such as leaching and mining. While laboratory tests can be performed under controlled conditions to give insight into the stress-strain behavior, there are always questions about the degree of sample disturbance caused during the retrieval of the sample from the ground or even the relevance of the tests since the lab samples do not usually incorporate features such as discontinuities.

The finite element mesh developed for these analyses represents a region 10,128 by 12,884 feet in lateral dimension and extending vertically from the ground surface down to the depth of 6000 ft. There are various assumptions for the computer simulations documented in this section:

- Use the simplified geometries such as an elliptical salt dome, cylindrical caverns, vertical shear zone (fault), planar layer for each interface between the lithologies, etc.
- All materials are assumed to be isotropic and homogeneous.
- Use the material properties of sand for the interfaces between the lithologies.
- Use a thickness of 14 ft for every interface.
- Apply a simplified workover cycle (5 years) to all caverns.
- Use a simplified workover duration (3 months). The wellhead pressure is dropped to zero during the workover.
- Use an equivalent wellbore section (one steel casing and one cement annulus rather than the as-built double steel casings and double cement annuli).
- The steel casing is assumed to be perfectly centered in the borehole and bonded to the cement.
- The cement is assumed to be perfectly bonded to the surrounding rock formation.
- No account for post-yield hardening in the steel is considered (an elastic/perfectly-plastic material model is used).

2.2. Geomechanical Model

2.2.1. Salt dome geometry

Figure 1 shows a plan view of the BH site with contour lines defining the approximate location of the salt dome top. The locations of fourteen SPR cavern currently in-use (101-114) and five potential expansion caverns (X1-X5) are indicated. The figure also specifies the undeveloped area north of the DOE property line (Sabine Pass Terminal). The horizontal shape of the dome is approximated as being elliptical. The major and minor ellipse axes are measured as 6422 ft and 5064 ft, respectively. The West-East cross-section #1 through the northern-most row of caverns (Cavern 101-105) provides a geologic representation near the middle of the dome (Figure 2). The site has a thin overburden layer consisting of sandy soil; and an exceptionally thick caprock sequence comprised of two layers. The upper caprock is comprised mainly of gypsum and limestone, whereas the lower caprock is mostly anhydrite. A major fault extends approximately North-South along the entire length of the caprock and for an unknown depth into the salt. This fault zone has a pronounced effect on the subsidence measured above the site and is a consideration for future cavern placement [Ehgartner and Bauer, 2004]. For analysis purposes, the top layer of overburden is modeled as having a thickness of 300 ft, the upper caprock 900 ft thick, and the lower caprock 430 ft thick. The salt thickness over the caverns is approximately 660 ft. The bottom boundary of the present analysis model is set at 6000 ft below the ground surface.

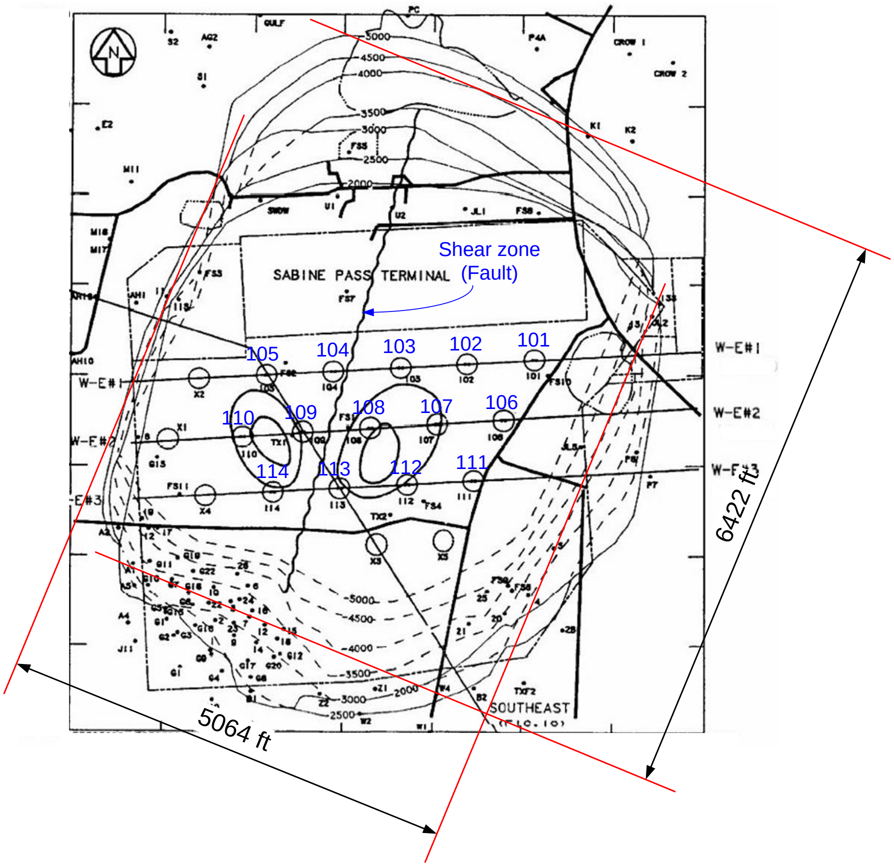

Figure 1: Big Hill site plan view [Magorian and Neal, 1988]

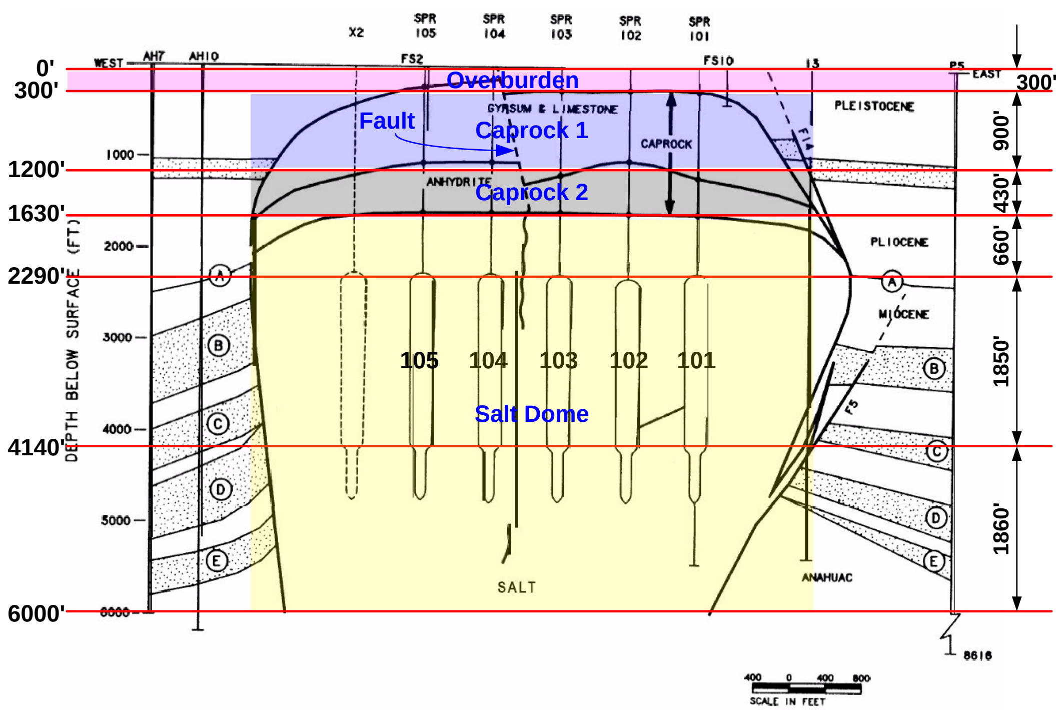

Figure 2: Cross-section (W-E #1 in Figure 1) near middle of dome [Magorian and Neal, 1988] looking north.

2.2.2. Salt Constitutive model and parameter values

Data for the creep constant, the stress exponent, and the thermal constant for the power law creep model used to describe the geomechanical behavior of the BH salt are very limited. Where needed, the data from the West Hackberry (WH) site has been used to augment the BH data, since both BH and WH salts are classified as soft salts [Munson, 1998] and are assumed to be mechanically similar for the purpose of this study. The salt data were derived through mechanical property testing of salt cores collected from boreholes [Wawersik and Zeuch, 1984]. The creep constitutive model considers only secondary or steady-state creep. The creep strain rate is determined from the effective stress as follows:

$$\dot{\varepsilon} = A\left(\frac{\sigma}{\mu}\right)^n \exp\left(-\frac{Q}{RT}\right) \quad (1)$$

where, $\dot{\varepsilon} =$ creep strain rate,

$\sigma =$ von Mises equivalent stress,

$\mu =$ shear modulus = E/2(1+ν), where E is Young's modulus and ν is Poisson's ratio

T = absolute temperature,

A = power law creep constant determined from back-fitting the model to creep data

n = stress exponent,

Q = effective activation energy,

R = universal gas constant.

The creep constant, A, in Eq. (1) is adjusted by a structural multiplication factor (SMF) which is used to match the volumetric closure of caverns. Through a number of back-fitting analyses [Park et al., 2005], a calibrated power law creep constant was determined. The values used as input data in the present analyses are listed in Table 1.

Table 1. Material properties of Big Hill salt used in the analysis.

Parameter	Unit	Value	Reference
Young's modulus (E)	GPa	31	Krieg, 1984
Density (ρ)	kg/m^3	2300	Krieg, 1984
Poisson's ratio (v)	-	0.25	Krieg, 1984
Elastic modulus reduction factor (RF)	-	12.5	Krieg, 1984
Bulk modulus (K)	GPa	20.67	Using E, v
Shear modulus (μ)	GPa	12.40	Using E, v
Creep constant (A)	$Pa^{-4.9}/s$	5.79×10^{-36}	Krieg, 1984
Structural multiplication factor (SMF)	-	1.5	Park et al., 2005
Calibrated creep constant	$Pa^{-4.9}/s$	8.69×10^{-36}	Park et al., 2005
Stress exponent (n)	-	4.9	Krieg, 1984
Thermal constant (Q)	cal/mol	12000	Krieg, 1984
Universal gas constant (R)	cal/(mol·K)	1.987	Mohr et al., 2011
Input thermal constant (Q/R)	K	6039	Using Q and R

2.2.3. Lithologies around the salt dome

The surface overburden layer, which is mostly comprised of sandy soil, is modeled as exhibiting linear elastic material behavior. The layer is also considered isotropic, and has no assumed failure criteria. The upper caprock layer, consisting of gypsum and limestone, is also assumed to be linear elastic. The rock surrounding the salt dome is assumed to be isotropic, homogeneous, linear elastic sandstone.

The anhydrite in the lower caprock layer is expected to experience inelastic material behavior. The anhydrite layer is considered isotropic and elastic until yield occurs [Butcher, 1997]. Once the yield stress is reached, plastic strain begins to accumulate. Yield is assumed to be governed by the Drucker-Prager (D-P) criterion:

$$\sqrt{J_2} = C - aI_1 \tag{2}$$

where $I_1 = \sigma_1 + \sigma_2 + \sigma_3 = 3\sigma_m$ is the first invariant of the stress tensor;

$\sqrt{J_2} = \sqrt{\frac{(\sigma_1 - \sigma_2)^2 + (\sigma_2 - \sigma_3)^2 + (\sigma_3 - \sigma_1)^2}{6}}$ is the square root of the second invariant of the deviatoric stress tensor; σ_1, σ_2, and σ_3 are the maximum, intermediate, and minimum principal stresses, respectively; σ_m is the mean stress; and C and a are D-P constants.

Again, the material properties of the BH anhydrite are not known. Therefore, the behavior of the BH anhydrite is assumed to be the same as the Waste Isolation Pilot Plant (WIPP) anhydrite. A non-associative flow rule is used to determine the plastic strain components. A soils and foams model is used for the lower caprock. The input parameters, A_0 and A_1, are derived from the elastic properties and the D-P constants, C and a [Park et al., 2005].

The material properties for the lithologies overlying and surrounding the BH salt dome used as input data for the two SNL-developed 3D solid mechanics codes used in the present analyses, JAS3D[§] and Adagio**, are listed in Table 1 and Table 2.

§ JAS3D is a three dimensional (3D) iterative solid mechanics code developed by SNL.

** Adagio is the most recently SNL-developed 3D solid mechanics code. It is written for parallel computing environments.

Table 2. Material properties of lithologies around salt dome used in the analyses.

		Unit	Overburden (Sandy soil)	Caprock 1 (Limestone and gypsum)	Caprock 2 (Anhydrite)	Surrounding Rock (Sandstone)
Young's modulus (*E*)		GPa	0.1	21	75.1	70
Density (*ρ*)		kg/m^3	1874	2500	2300	2500
Poisson's ratio (*v*)		0.25	0.33	0.29	0.35	0.33
Drucker-Prager constants	*C*	MPa	N/A	N/A	1.35	N/A
	a	-	N/A	N/A	0.45	N/A
Bulk modulus (*K*)		GPa	N/A	N/A	83.44	N/A
Shear modulus (*μ*)		GPa	N/A	N/A	27.82	N/A
Soil and forms model constants	A_0	MPa	N/A	N/A	2338	N/A
	A_1	-	N/A	N/A	2.338	N/A
	A_2	-	N/A	N/A	0	N/A

2.2.4. Interfaces and Fault Model

To investigate causes of well casing damage between the salt dome and the caprock, horizontal shear displacements and vertical strains at the interfaces need to be examined. Thus, interface blocks, special purpose analysis tools, are used to represent the interfaces between Caprock 1 and Caprock 2; Caprock 2 and Salt Dome; Surrounding Rock and Dome. The material behavior away from the interfaces is represented by material properties of Caprock 1, Caprock 2, and Salt. The fault, which was ignored for the simplification in previous analyses [Park et al., 2005], is included in this model to perhaps better represent the large scale deformation considered in this study.

There is no interface geometry and material property data obtained from the field. The interfaces and fault are assumed to behave mechanically like sandy soil, thus the overburden material properties (Table 2) are used in the analyses for the interfaces and fault. In this study, the thicknesses of the interface materials are assumed to be a uniform 14 ft based on the measured largest thickness of the salt/caprock interbed from a Weatherford multi-arm caliper survey data [Sattler and Ehgartner, 2011]. The thickness of fault varies from a millimeter to a hundred meters with fault displacement (Figure 3). The fault thickness is also assumed to be a uniform 14 ft for simplification. These model attributes were incorporated into the finite element method (FEM) mesh described in Chapter 3.

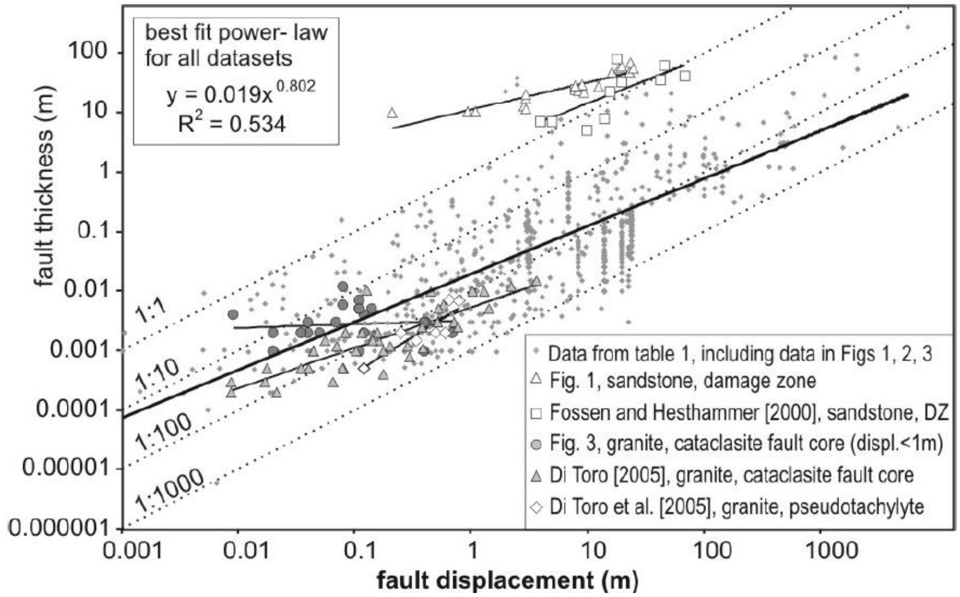

Figure 3: Log-log plot of a compilation of 16 fault thickness datasets [Hull, 1988; Shipton, et al., 2006].

2.3. Cavern Model

2.3.1. Cavern geometry and layout

The cavern shapes are approximately cylindrical and the cavern array regular as shown in Figure 4. The cavern dimensions used in the model are simplified and are listed in Table 3 based on sonar data. The completion date for the initial leach of each cavern is also listed. The X- and Y-coordinates for the center of each cavern were calculated by subtracting the Universal Transverse Mercator (UTM) coordinates at the center of the dome from UTM coordinates of each cavern. That is, the origin for the coordinate system of the model is the center of the dome.

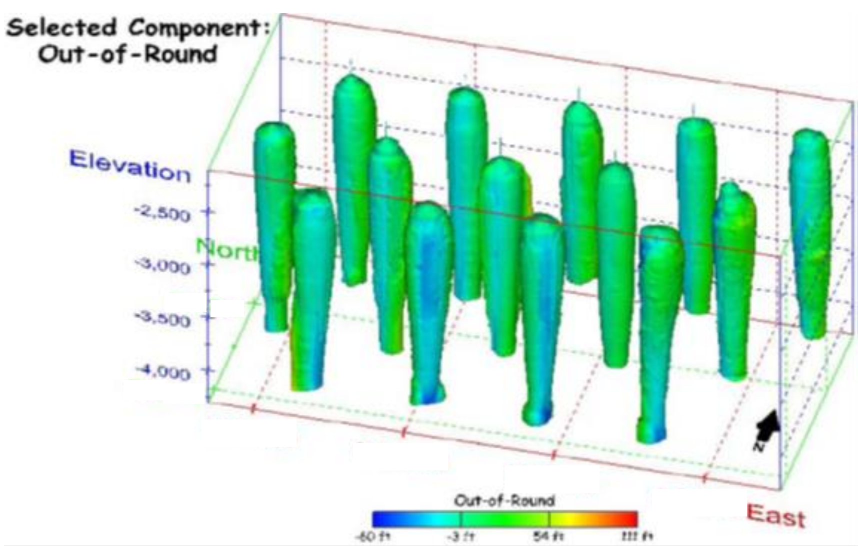

Figure 4: Perspective view of the cavern field at the Big Hill SPR site from the southeast [Rautman and Lord, 2007]. Elevation units are feet.

Table 3: Geometric parameters and initial leach completion dates for the fourteen extant caverns. The bold fonts indicate the baseline dates.

Cavern ID	X (East)	Y (North)	Z (Vertical Center)	Diameter	Radius	Cavern Top	Cavern Bottom	Cavern Height	Leach Completion Date
	ft	ft	ft	ft	ft	ft	ft	ft	mm/dd/yyyy
101	1875	-551	-3215	220	110	-2290	-4140	1850	9/18/1990
102	1125	-551	-3215	220	110	-2290	-4140	1850	10/21/1990
103	375	-551	-3215	220	110	-2290	-4140	1850	11/28/1990
104	-375	-551	-3215	220	110	-2290	-4140	1850	10/21/1990
105	-1125	-551	-3215	220	110	-2290	-4140	1850	**11/11/1990**
106	1500	-1200	-3215	220	110	-2290	-4140	1850	10/16/1990
107	750	-1200	-3215	220	110	-2290	-4140	1850	4/24/1990
108	0	-1200	-3215	220	110	-2290	-4140	1850	6/14/1990
109	-750	-1200	-3215	220	110	-2290	-4140	1850	**7/24/1990**
110	-1500	-1200	-3215	220	110	-2290	-4140	1850	4/19/1990
111	1124	-1849	-3215	220	110	-2290	-4140	1850	7/15/1991
112	374	-1850	-3215	220	110	-2290	-4140	1850	6/19/1991
113	-376	-1849	-3215	220	110	-2290	-4140	1850	5/1/1991
114	-1126	-1849	-3215	220	110	-2290	-4140	1850	8/29/1991

2.3.2. Model history

The caverns were leached from April 1990 through August 1991 as listed in Table 3. To investigate the cause of oil leaks and evaluate the condition of the other casings at the site, the slick well casing above the caverns were recently inspected with a Weatherford multi-arm caliper. The leak date of Cavern 109 is regarded as a critical baseline for wellbore failure in this simulation. For example, July 24, 1990, when the Cavern 109 leach was completed, is 242.66 months (21.22 years) before October 8, 2010, when the oil leak occurred at Well 109. The simulation results will be generated every month i.e., the smallest output time unit is one month. 242.66 months can be rounded off to 243 months (21.25 years) which is calculated to be July 13, 1990. Thus the leach completion date of Cavern 109 is assumed to be July 13, 1990 rather than July 24, 1990 (actual date). To simplify the model history for the purposes of the present simulation, it is assumed that all existing caverns were initially leached on July 13, 1990, which is the leach completion date of Cavern 109 and considered time t = 1 year in the simulation. The analysis simulates caverns that were leached to full size over a one year period by means of gradually switching from salt to fresh water in the caverns. It was assumed that the SPR caverns were filled with petroleum one year after their initial leaches start. The water head pressure, a pressure gradient of 0.43 psi/ft of depth, is applied to the wellbore wall during the initial leach. The caverns are simulated as creeping for fifty years. Figure 5 shows the time sequence for this study of the BH site.

Table 4 lists the number of days in a five year period used for workovers[††], fluid transfers, and normal operation with the internal pressure ranges in each cavern. The pressure condition applied to each cavern is based on an average wellhead pressure of 905 psi which occurs when the wells are operated at normal or static conditions. An analysis of cavern pressures at BH between the

†† "Workover" is when the wellhead pressure in the cavern is dropped to zero for maintenance.

years 1990 to 2010 indicates a cavern is pressurized within its normal operating range 74.0% of the time (1351 days during each five year period between drawdown leaches). Other operations, such as fluid transfers and workovers, require lower cavern pressures. Therefore, pressure drops are periodically included to simulate times during workover conditions. For simulation purposes, the pressure drop to a wellhead pressure of 0 psi within each cavern lasts for 3 months which is about 4.9% of the time (89 days) during each 5-year period. Rather than complicating the analyses, the following assumptions were made for the workover scenario. To better simulate actual field conditions, not all caverns are in workover mode at the same time.

Drawdowns‡‡ are not considered in this simulation. The simulation is conducted for 51 years. The pressure condition applied to each cavern and wellbore is based on an average wellhead pressure of 905 psi which occurs when the wells are operated at normal or static conditions. Figure 6 shows the wellhead pressure histories for each cavern. For workover conditions, the wellhead pressure is dropped to zero. The workover durations are 3 months for all caverns. This workover cycle is repeated every 5 years. For both normal and workover conditions, the caverns and wellbore are assumed to be full of oil having a pressure gradient of 0.37 psi/ft of depth. The pressure due to the oil head plus the wellhead is applied on the cavern and wellbore boundary during the normal operation. Creep closure is allowed to occur in all caverns during the simulation period.

Workover scenario:

- A constant pressure (905 psi) indicating a normal condition is applied for the majority of the time.
- For cavern workover, the wellhead pressure is dropped to zero.
- Workover of Cavern 101 begins one year after the initial leach is completed. After that, workovers are performed on Caverns 102 through 114 in numerical order. Workovers begin as soon as the workover of the prior cavern is completed.
- Workover durations are 3 month for all caverns.
- This workover cycle is repeated every 5 years.
- For both normal and workover conditions, the caverns are assumed to be full of oil having a pressure gradient of 0.37 psi/ft of depth.
- Pressure due to the oil head plus the wellhead is applied on the cavern boundary during the normal operation.

‡‡ "Drawdown" is when the crude oil is withdrawn from the cavern. Fresh water is used to withdraw the crude oil. Because the cavern enlarges due to salt dissolving from the cavern walls, it is called a "drawdown leach".

Table 4: Days in five year period with internal pressure ranges.

Cavern	Internal Pressure			days in 5 year period		
	0 to 400 psi	400 to 800 psi	800 + psi	workovers	Fluid transfers	Normal operation
BH101	5.1%	22.7%	71.8%	93	415	1310
BH102	2.7%	16.7%	80.3%	50	305	1466
BH103	3.6%	20.1%	76.1%	66	366	1390
BH104	3.1%	21.9%	74.8%	56	400	1365
BH105	5.9%	16.7%	77.1%	108	304	1407
BH106	4.8%	16.1%	79.0%	88	294	1441
BH107	4.4%	20.5%	74.8%	80	374	1366
BH108	7.0%	20.1%	72.9%	127	366	1330
BH109	6.4%	20.1%	73.4%	116	366	1339
BH110	6.1%	30.6%	63.1%	110	558	1152
BH111	3.7%	14.4%	81.6%	68	264	1490
BH112	4.9%	24.2%	70.7%	89	441	1290
BH113	4.2%	29.8%	65.8%	76	544	1202
BH114	6.8%	17.8%	75.1%	124	325	1371
Average	4.9%	20.8%	74.0%	89	380	1351

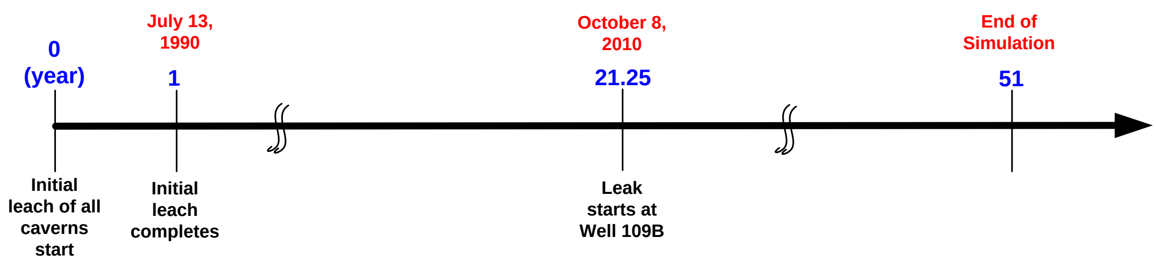

Figure 5: Time sequence for the simulation.

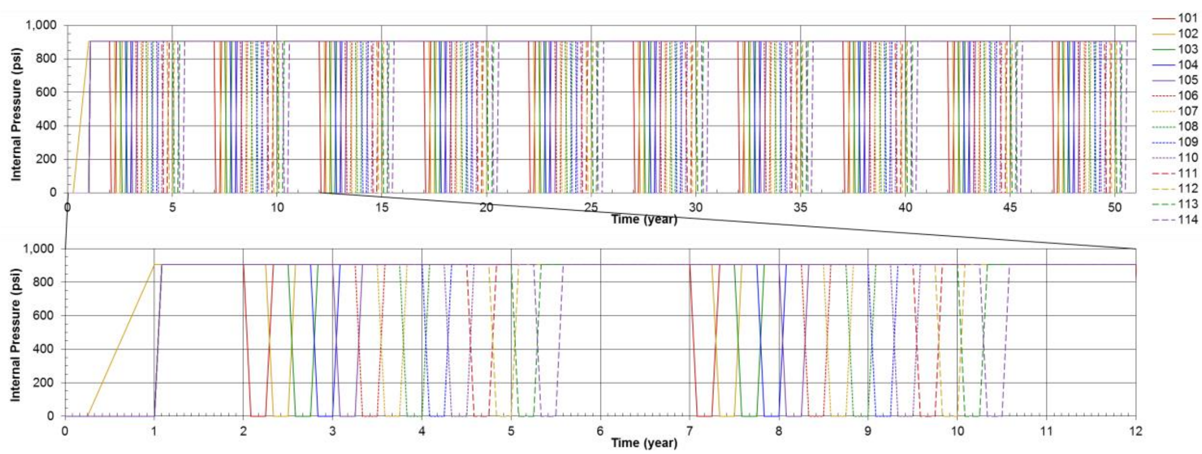

Figure 6: Applied wellhead pressure change on each cavern boundary over time.

2.4. Wellbores

The previous Big Hill model [Park and Ehgartner, 2012] calculated large-scale displacements in the salt dome structure caused by the creep-induced closure of the storage caverns. To investigate causes of wellbore damage between the salt dome and the caprock, interface blocks, special purpose analysis tools, were implemented in the model for the caprock-salt interbed. However, the wellbore casings were not included in the previous model, and this omission led to questions about the effect of those casings on the interaction between the salt and caprock. To figure out how the wellbore impedes the movement of the salt dome top, a global model, which contains the wellbore blocks, was reconstructed.

Figures 7 and 8 show the well completion configuration of BH-109 A and B, respectively, as examples. At Big Hill, each cavern has two wellbores (Well A and Well B) near the center of each cavern that consist of double steel casings and double cement annuli as shown in Figure 9. The thicknesses of inner and outer steel casings are about 0.430 inches and 0.635 inches, respectively. The thicknesses of inner and outer cement annuli are about 2.678 inches and 4.5 inches, respectively. These thicknesses are obtained from the drawing information in Figures 7 and 8. The nominal weight of inner steel casing is 61 lbs/ft between the depth of 1222 ft and 1710 ft. The nominal weight of outer steel casing is 133 lbs/ft between the depth of 1205 ft and 1841 ft. The dimensions of the various steel casings are listed in the API Casing Chart provided in Appendix I.

The thicknesses of steel casings and cement annuli are very small relative to the global model size. The maximum size of global model will be 12,844 ft, while the thickness of inner steel casing is about 0.43 inches. This size difference necessarily produces a poor quality mesh. To improve the mesh quality, the blocks would have to be divided into smaller sizes of elements. Then, the number of elements in the mesh would be more than tens of millions. A mesh with such a large number of elements would consume an extraordinary amount of computer CPU (Central Processing Unit) time.

To avoid this inefficiency, the well casings in the global model were constructed using an equivalent wellbore model. This model, which consists of a single steel casing and single cement annulus, was constructed using the combined moment of inertia of the areas of casings from two boreholes, as shown Figure 9. The moments of inertia I_X, I_Y, and I_{XY} for a single steel casing in the equivalent wellbore are calculated to be the same as the summation of I_X, I_Y, and I_{XY} for double steel casings in two wellbores, to obtain the area of the steel casing in the equivalent wellbore. In the same manner, the area of the single cement annulus in the equivalent wellbore is calculated from the areas of double cement annuli in two wellbores. Then, the equivalent wellbore behaves structurally the same as two wellbores because of the same moment of inertia of the areas. The thicknesses of the equivalent single steel casing and single cement annulus are calculated to be 2.028 inches and 7.622 inches, respectively, which result in a mesh with fewer elements and acceptable quality to conserve CPU time consumption.

The two materials comprising the wellbore configuration, namely the steel and cement, were modeled numerically using two different constitutive models. The K55 steel was modeled with an elastic-plastic constitutive model. The cement was modeled with the Kayenta model, a generalized cap-plasticity model.

2.4.1. Steel Casings

The elastic-plastic model used here is based on a standard von Mises type yield condition and uses combined kinematic and isotropic hardening, in the most general case. This model is widely used in many finite element computer programs and the many details of its derivation and implementation are scattered throughout the literature [e.g., Krieg and Krieg, 1977 and Schreyer et. al, 1979]. Taylor and Flanagan [1989] provide details of the model, as implemented within the SNL codes. For purposes of the calculations herein, hardening was not allowed, thereby rendering the model to be elastic perfectly-plastic. Table 5 shows the K55 steel material parameters used in the calculations for the elastic-plastic model.

Table 5: Elastic-Plastic Material Model Parameters used for K55 Steel.

Parameter	Value
Density (ρ)	7860 kg/m^3 (490.7 lb/ft^3)
Young's Modulus (E)	1.999x10^{11} Pa (2.899x10^7 psi)
Poisson's Ratio (ν)	0.3
Yield Stress	4.277x10^8 Pa (62000 psi)
Isotropic/Kinematic Hardening Parameter (β)	0.5
Hardening Modulus	0.0 Pa

2.4.2. Cement Annuli

The overarching goal of the Sandia Geomodel developed by Fossum and Brannon [2004] is to provide a unified general-purpose constitutive model that can be used for any geological or rock-like material that is predictive over a wide range of porosities and strain rates. The details of the Sandia Geomodel, which is implemented in JAS3D, are provided in Fossum and Brannon [2004]. Being a unified theory, the Sandia Geomodel can simultaneously model multiple failure mechanisms or it can duplicate simpler idealized yield models such as classic Von Mises plasticity and Mohr-Coulomb failure. For natural geomaterials, as well as for some engineered materials (e.g., ceramics and concretes), common features are the presence of microscale flaws, such as porosity, and networks of microcracks. Microscale flaws permit inelasticity even in purely hydrostatic loading. Networks of microcracks lead to low strength in the absence of confining pressure and to noticeable nonlinear elasticity, rate-sensitivity, and differences in material deformation under triaxial extension when compared to triaxial compression. Simpler models that do not include this phenomenology are incapable of accurately predicting the response of rock-like materials such as the cement [Arguello et al., 2009].

The Kayenta model is the successor of the Sandia Geomodel in Adagio. The Kayenta model includes features and fitting functions appropriate to a broad class of materials including rocks, rock-like engineered materials such as concretes and ceramics, and metals. Fundamentally, the Kayenta model is a computational framework for generalized plasticity models. As such, it includes a yield surface, but the term "yield" is generalized to include any form of inelastic material response including microcrack growth and pore collapse. The Kayenta model supports optional anisotropic elasticity associated with ubiquitous joint sets. The Kayenta model supports optional deformation-induced anisotropy through kinematic hardening. The governing equations are otherwise isotropic. Because the Kayenta is a unification and generalization of simpler models, it can be run using as few as two parameters (for linear elasticity) to as many as 40 material and control parameters in the exceptionally rare case when all features are used. For high-strain-rate applications, the Kayenta model supports rate dependence through an overstress model. Isotropic damage is modeled through loss of stiffness and strength [Brannon et al., 2009].

The cement material response in the calculations was modeled using the parameters given in Brannon et al. [2009], Appendix B for “Conventional Strength Portland Concrete.” Table 6 shows the material parameters for the Kayenta model used in the calculations to simulate the cement. The parameters *B0* and *G0* given in the table correspond to the elastic bulk and shear modulus, respectively. These values convert to a corresponding Young’s modulus, *E*, of 18.4 GPa ($2.67x10^6$ psi) and Poisson’s ratio, ν of 0.22.

Table 6: Material properties of cement [Brannon et al., 2009; Arguello et al., 2009].

Parameter	Value	Description
ρ	2250 kg/m^3 (140.5 lb/ft^3)	Density
ν	0.22	Poisson's Ratio
B0	$1.0954x10^{10}$ Pa (1588743 psi)	Initial elastic bulk modulus
B1	0 Pa	High pressure coefficient in nonlinear elastic bulk modulus function
B2	0 Pa	Curvature parameter in nonlinear elastic bulk modulus function
B3	0 Pa	Coefficient in nonlinear elastic bulk modulus to allow for plastic softening
B4	0	Power in nonlinear elastic bulk modulus softening
G0	$7.5434x10^{9}$ Pa (1094078 psi)	Initial elastic shear modulus
G1	0	Coefficient in shear modulus hardening
G2	0 Pa^{-1}	Curvature parameter in shear modulus hardening
G3	0 Pa	Coefficient in shear modulus softening
G4	0	Power in shear modulus softening
RJS	0 m	Joint spacing
RKS	0 Pa/m	Joint shear stiffness
RKN	0 Pa/m	Joint normal stiffness
A1	$4.26455x10^{8}$ Pa (61852 psi)	Constant term for meridional profile function of ultimate shear limit surface
A2	$7.51x10^{-10}$ Pa^{-1} ($5.178x10^{-6}$ psi^{-1})	Curvature decay parameter in the meridional profile function
A3	$4.19116x10^{8}$ Pa (60788 psi)	Parameter in the meridional profile function
A4	$1.0x10^{-10}$ rad	High-pressure slope parameter in meridional profile function
P0	$-1.9552x10^{8}$ Pa (-28358 psi)	One third of the elastic limit pressure parameter at onset of pore collapse
P1	$1.2354x10^{-9}$ Pa^{-1} ($8.518x10^{-6}$ psi^{-1})	One third of slope of porosity vs. pressure crush curve at elastic limit
P2	0 Pa^{-2}	Parameter for hydrostatic crush curve
P3	0.065714	Asymptote of the plastic volumetric strain for hydrostatic crush
CR	12.0	Parameter for porosity affecting shear strength
RK	1	Triaxial extension strength to compression strength ratio
RN	0 Pa	Initial shear yield offset [non negative]
HC	0 Pa	Kinematic hardening parameter
CUTI1	$3.0x10^{6}$ Pa (435 psi)	Tension cut-off value of I1
CUTPS	$1.0x10^{6}$ Pa (145 psi)	Tension cut-off value of principal stress
T1	0 s	Relaxation time constant 1
T2	0 s^{-1}	Relaxation time constant 2
T3	0	No longer used. Set to zero
T4	0 s^{-1}	No longer used. Set to zero
T5	0 Pa	Relaxation time constant 5 (stress)
T6	0 s	Relaxation time constant 6 (time)
T7	0 Pa^{-1}	Relaxation time constant 7 (1/stress)
J3TYPE	3	Type of 3^{rd} deviatoric stress invariant function (1-Gudehus,2-Willam-Warnke,3-Mohr-Coulomb)
A2PF	0 Pa^{-1}	Potential function parameter 1 (default=A2)
A4PF	0 rad	Potential function parameter 2 (default=A4)
CRPF	0	Potential function parameter 3 (default=CR)
RKPF	0	Potential function parameter 4 (default=RK)
SUBX	-1	Subcycle step size increment parameter

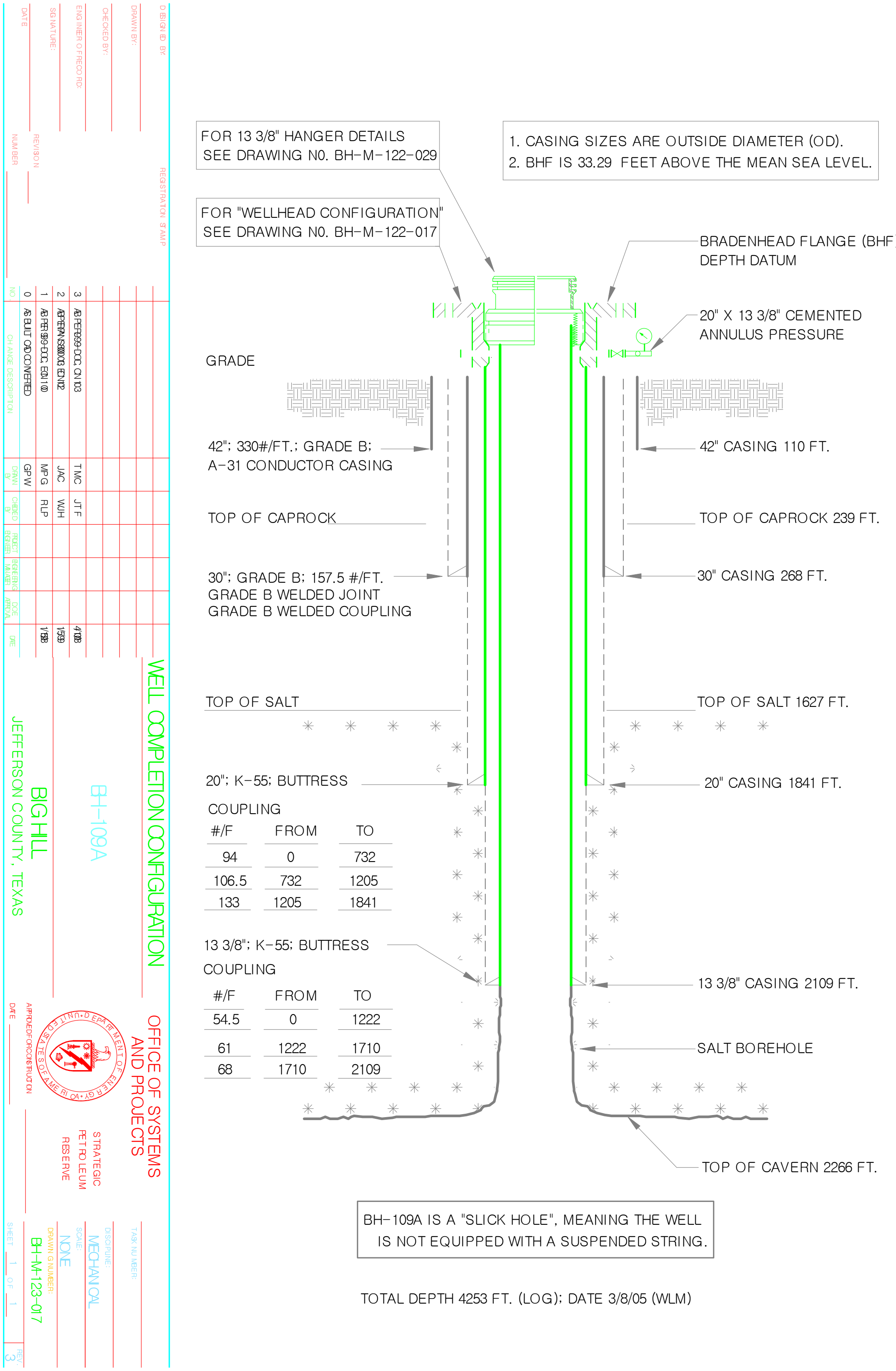

Figure 7: Well Completion Configuration, BH-109A

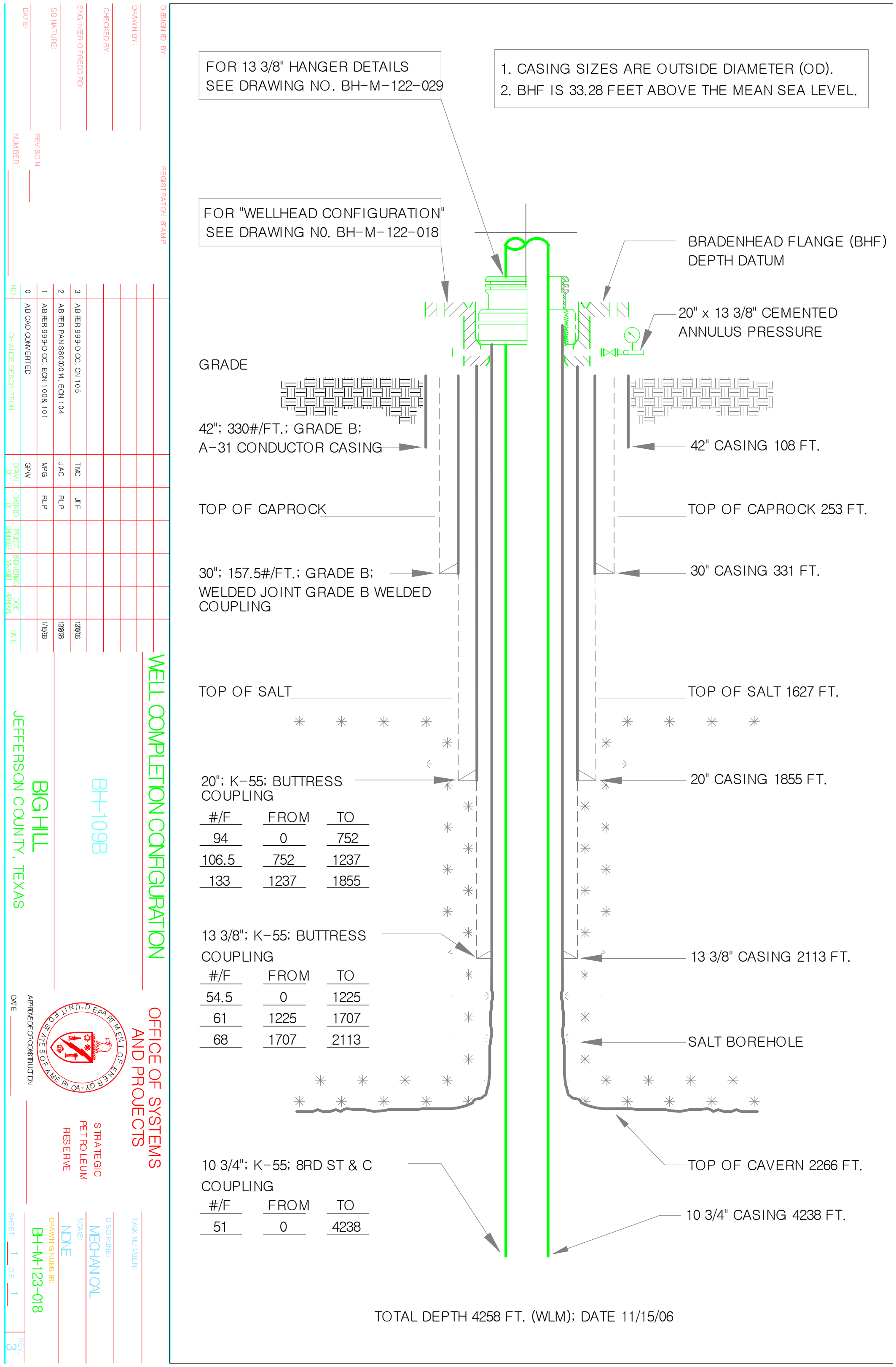

Figure 8: Well Completion Configuration, BH-109B

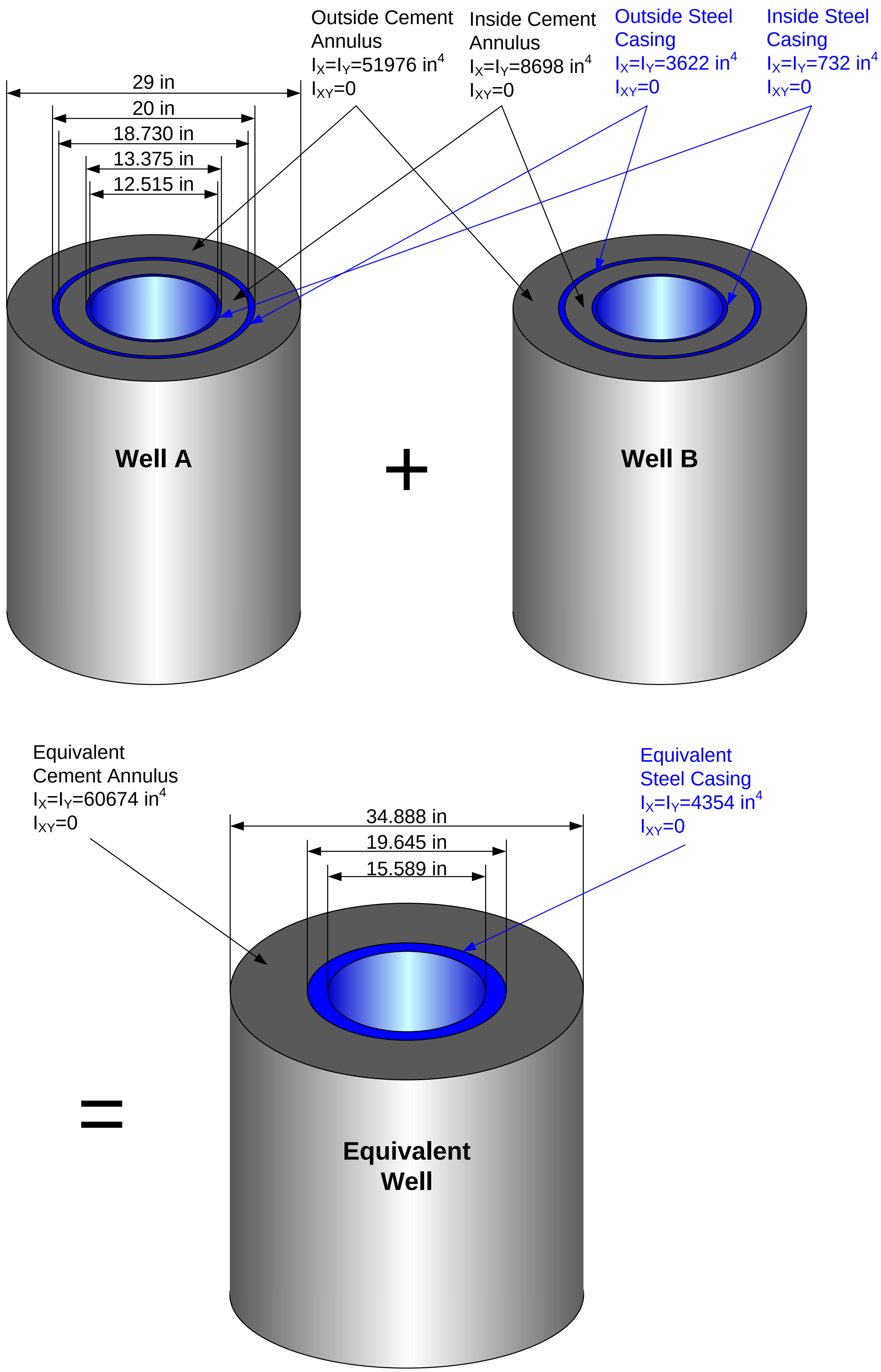

Figure 9: Equivalent wellbore calculation using moment of inertia of an area

2.5. Thermal Conditions

The finite element model includes a depth-dependent temperature gradient which starts at 76.7 °F (24.84 °C) at the surface and increases at the rate of 1.41 °F/100 ft (2.57 °C/100 m). The temperature profile is based on the average temperature data recorded in well logs from BH prior to leaching [Ballard and Ehgartner, 2000]. The temperature distribution is important because the creep response of the salt is temperature dependent. Radial temperature gradients due to cavern cooling effects from the cavern contents are not considered in these calculations. Previous 2D cavern studies have shown the predicted cavern deformation to be insensitive to the developed radial thermal gradients [Hoffman, 1992].

3. MESH

A three dimensional mesh, which allows each cavern to be configured individually, was constructed to investigate wellbore damages at the interbed between the caprock bottom and the salt top. To figure out how the wellbore impedes the movement of the salt dome top, the wellbore blocks are contained in the mesh. Figure 10 shows an overview of the finite element mesh of the stratigraphy and cavern field at BH. The mesh has been separated to show the individual material blocks. The X-axis of the model is in the East direction, Y-axis is along the North direction, and Z-axis is the vertical direction, up being positive. The mesh consists of eleven material blocks. Five material blocks used are Overburden, Caprock 1, Caprock 2, Salt Dome, and Surrounding Rock. Three material blocks are used for the interfaces, and one material block is used for the fault. The two material blocks are used for steel casings and cement annuli.

The Surrounding Rock block encompasses Caprock 1, Caprock 2, and Salt Dome. The interbed under Caprock 1 is split off from it, thus the thickness of Caprock 1 block becomes 886 ft (= 900 ft – 14 ft). The interbed under Caprock 2 block is split off from it, thus the thickness of Caprock 2 block becomes 416 ft. The interface surrounding Caprock 1, Caprock 2, and Salt dome is split off from the inside of the Surrounding Rock block, thus the radii of Caprock1, Caprock 2, and Salt Dome are not changed but the inside radius of Surrounding Rock increases 14 ft.

The thickness of the fault (shear zone) is also assumed to be 14 ft. The strike direction and dip of the fault are N 18º E and 90º, respectively. The strike direction was approximated from Figure 1, and the dip was assumed to be vertical for simplification. The fault runs between Caverns 103 and 104, Caverns 108 and 109, and Caverns 113 and 114. The fault is assumed to extend down to the top of Salt Dome from the surface.

The interior of the model consists of material blocks Salt Dome, Caprock 1, and Caprock 2. It is idealized as an elliptical cylinder with major diameter of 6422 ft, minor diameter of 5064 ft, and height of 5700 ft (4370 ft of which is salt dome). The dome ellipse blocks are rotated clockwise 22.5° to realize the salt dome as shown Figure 11. To more easily see the cross-section of wellbores, each dome and wellbore material block is divided by four element blocks. Three cross-sections correspond to the East-West cross-sections #1, #2, and #3 in Figure 1. Fourteen cavern spaces exist inside the Salt Dome block to represent the cavern volumes. All caverns are idealized as cylinders 1850 ft high with 220 ft diameters. The tops of caverns are 660 ft down from the top of salt (2290 ft below the surface).

Figure 12 shows the assembled mesh and the boundary conditions. The salt dome is modeled as being subject to a regional far-field stresses acting from an infinite distance away. The lengths of the confining boundaries are 12,844 ft (two times the dome’s major diameter) in the N-S direction and 10,128 ft (two times the dome’s minor diameter) in the E-W direction. The mesh consists of 1,050,760 nodes and 1,012,932 elements with 37 element blocks, 5 node sets, and 28 side sets. The mesh was created using CUBIT§§ version 13.1.

---

§§ A mesh generation software copyrighted by Sandia Corporation

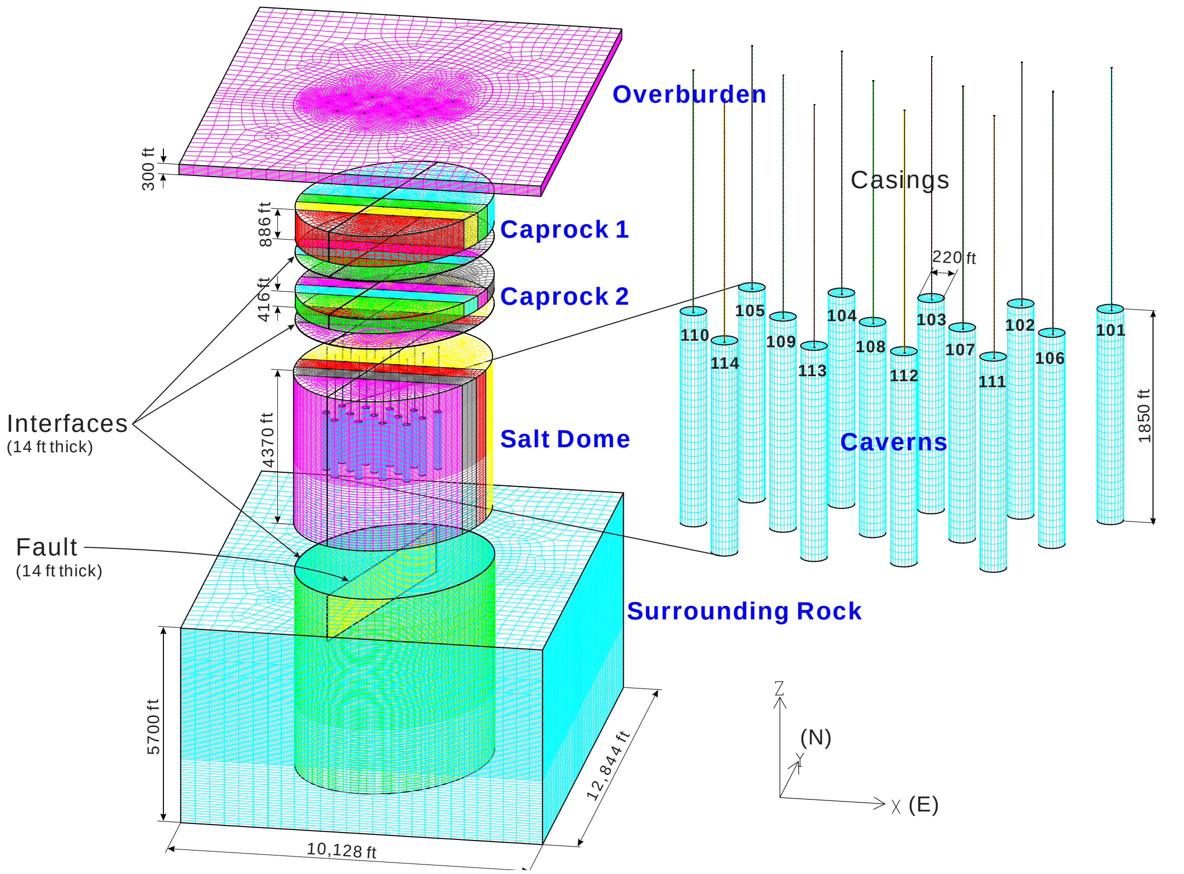

Figure 10: Overview of the components of the finite element mesh of the stratigraphy and cavern field at Big Hill.

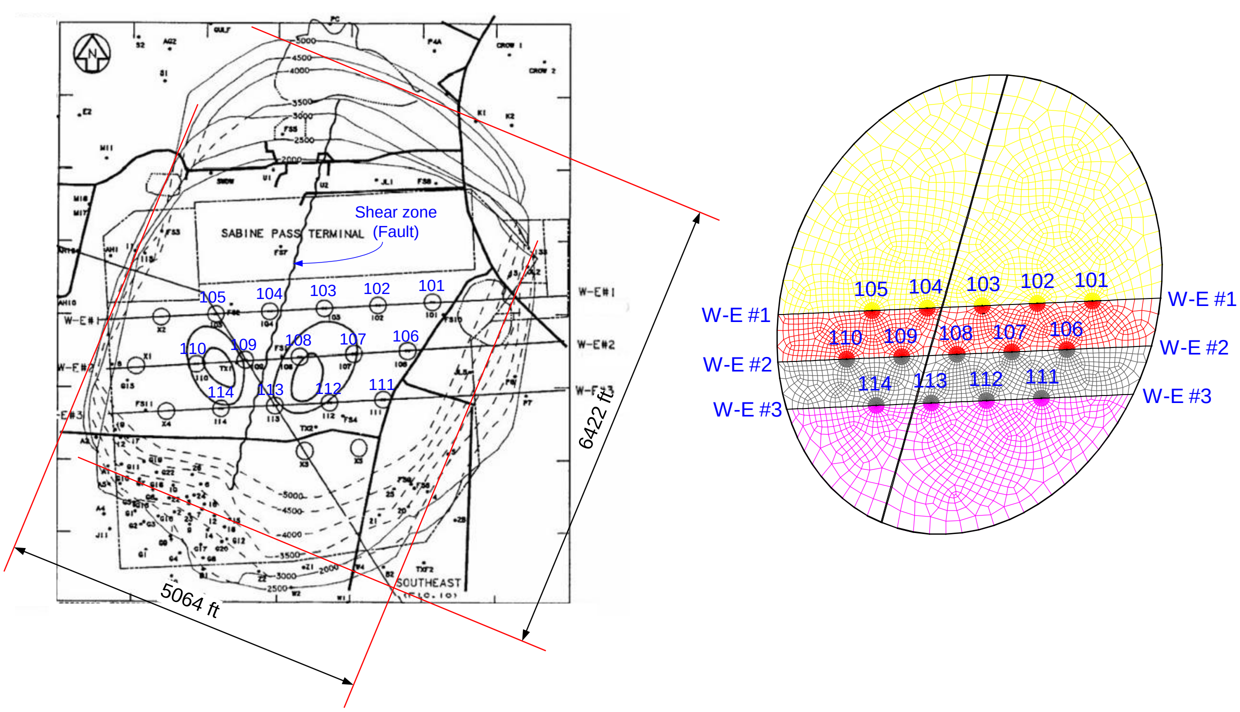

Figure 11: Realization of the dome as the FEM mesh.

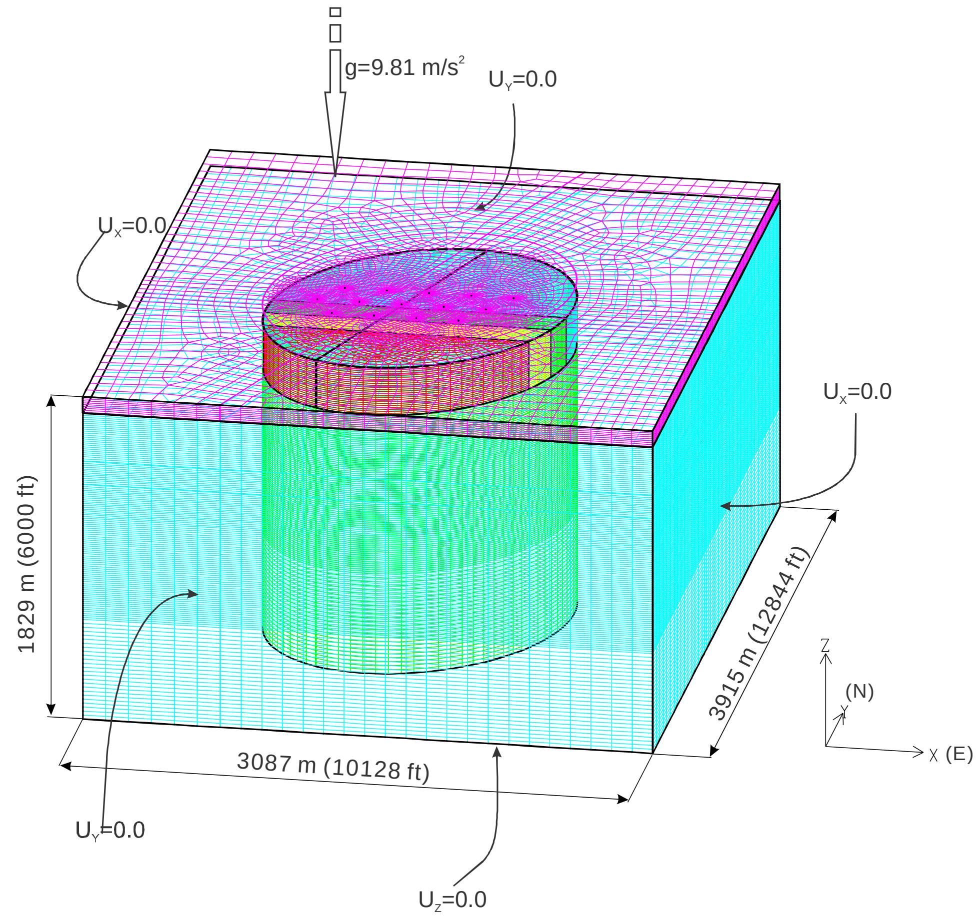

Figure 12: Finite mesh discretization and boundary conditions at Big Hill.

4. MODEL VERIFICAITON

4.1. Volume Closure

Figure 13 through Figure 15 show comparisons the simulated volumetric closure of Cavern 101, 106, and 111, respectively, normalized by the initial cavern volume (i.e. cavern volume strain) with the field data. The slopes of the lines are close to each other, i.e. the modeled volume closure rates match to the field data fairly well. The peaks and the abrupt volume closures in the analysis results are caused by the workover scenarios in each cavern. Discrepancy between the analysis results and the field data occur because the workover history for each cavern in the analysis is idealized with a five year period. The predicted total volumetric closure normalized by total initial volume of fourteen caverns matches to the field data fairly well as shown Figure 16. The peaks and abrupt volume closures of fourteen caverns are merged into one smooth line. The slopes of the trend lines from the analysis and field are almost the same at 0.0026. This model approximation is reasonable to use to investigate the interbed behavior because it is judged to represent the gross volume closure (strain) rather well.

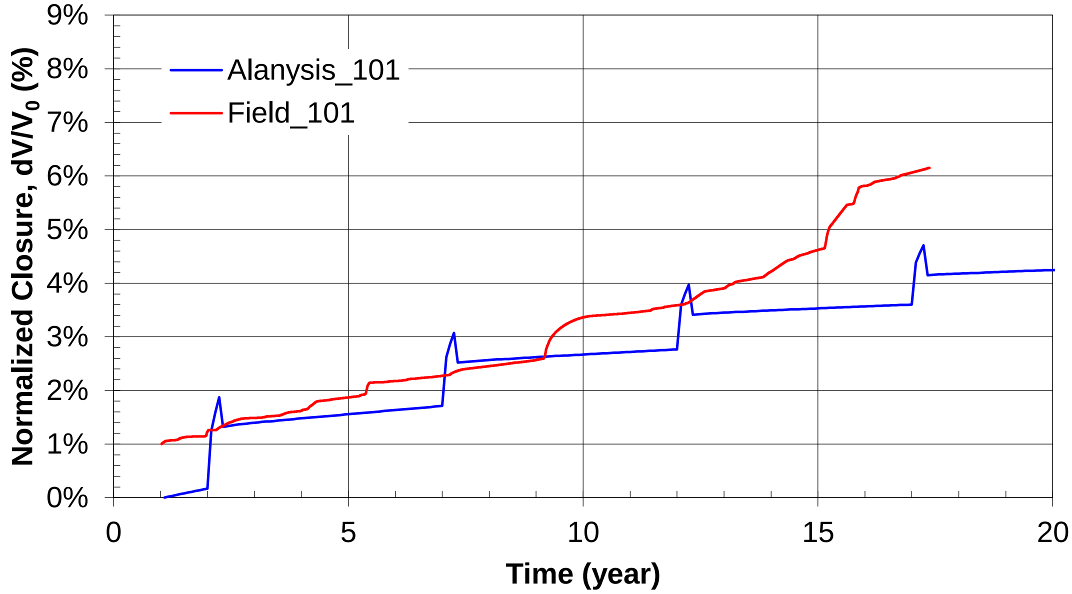

Figure 13: Comparison of predicted volumetric closure normalized by initial cavern volume for Cavern 101 with the field data.

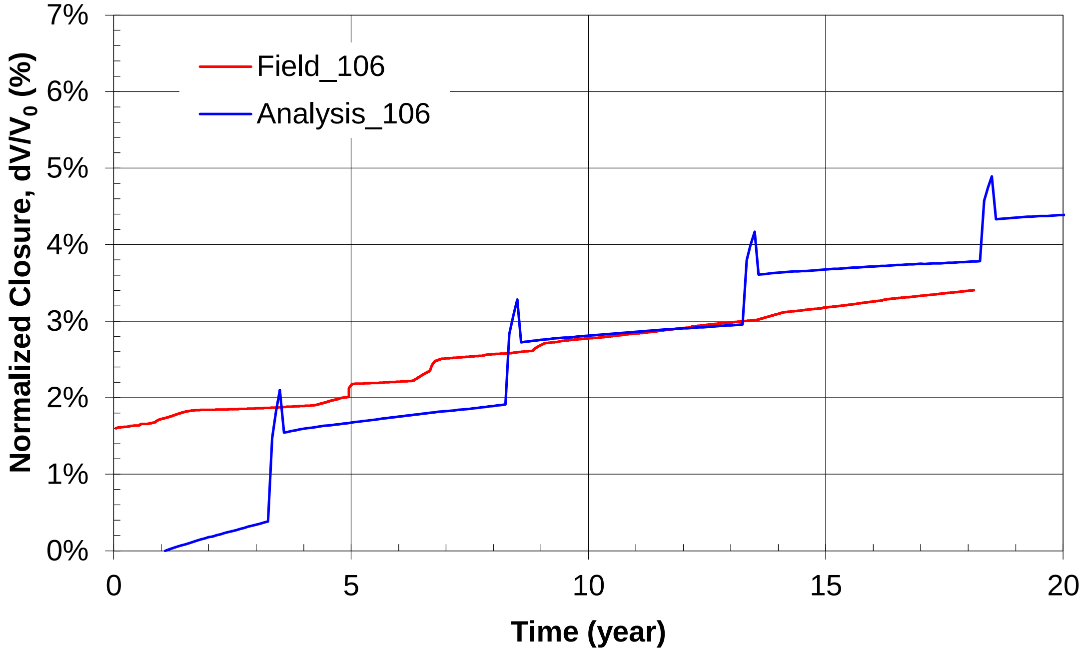

Figure 14: Comparison of predicted volumetric closure normalized by initial cavern volume for Cavern 106 with the field data.

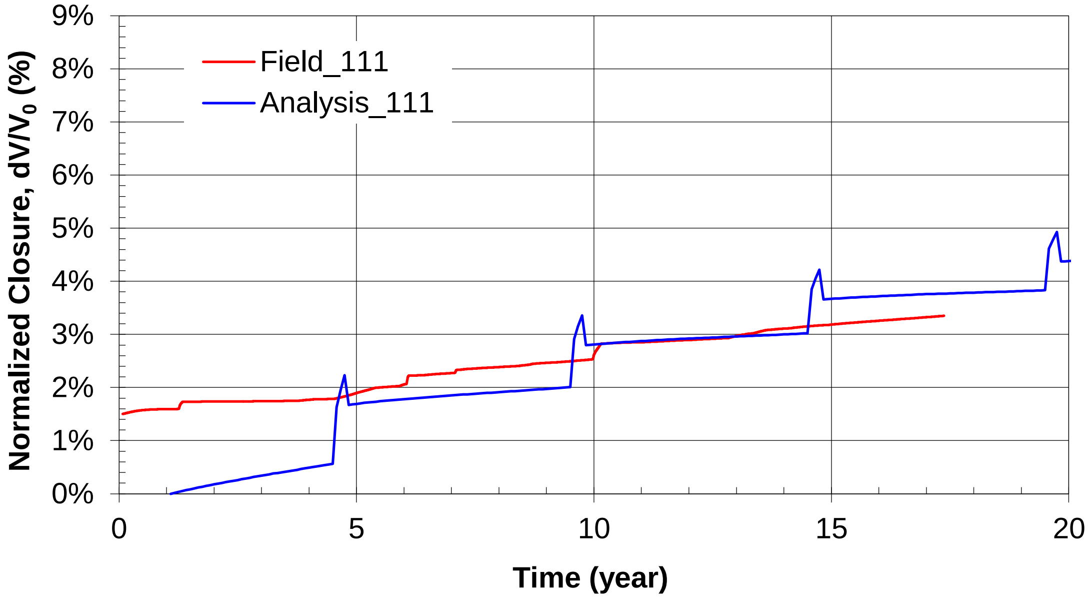

Figure 15: Comparison of predicted volumetric closure normalized by initial cavern volume for Cavern 111 with the field data.

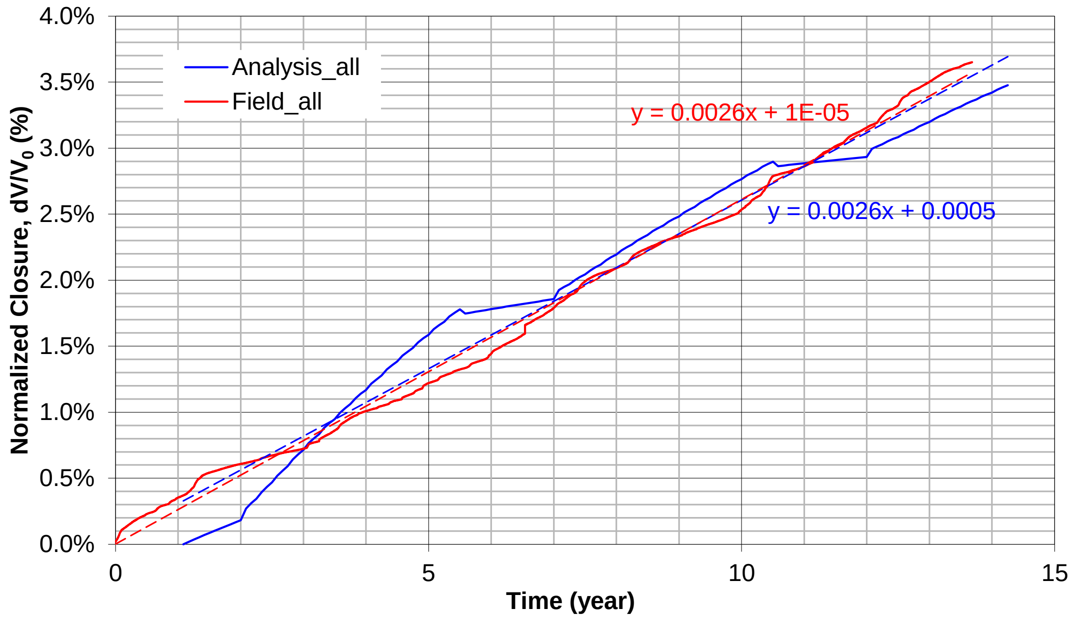

Figure 16: Comparison of predicted total volumetric closure normalized by total initial volume of the fourteen caverns with the field data.

4.2. Subsidence

At Big Hill, and other SPR sites in general, the surface elevation changes are measured because they document surface subsidence resulting from creep closure of caverns. General subsidence on the scale of the site or portions thereof is seen in the elevation data taken. The subsidence monument elevations at the BH Strategic Petroleum Reserve site were surveyed sixteen times between April, 1989 and March 2011. Measurements were taken at specified locations marked by monuments. Monuments are wellheads, other surface structures, or specifically installed elevation monuments. The quantity of data changes from year to year due to monument inaccessibility and/or destruction during site construction. Figure 17 is a plot presenting the elevation measurements from the March 2011 Big Hill site subsidence survey [Lord, 2011a]. The plot also shows the DOE property line, monuments, and cavern well locations.

Figure 18 shows the monument locations, which correspond to the locations noted by crosses in Figure 17, on the FEM mesh. Surface uplift has been occurring since 2002 in the eastern region of the BH cavern field due to injection of liquid waste into the Newpark injection wells [Lord, 2011]. These injection wells are in close proximity to the BH caverns. Five wells are actively being injected with waste, with the largest volumes being injected within the caprock in the southeastern region of the dome. Newpark injects approximately 2.4 MMB of liquid a year into the caprock. This injection impacts subsidence and caprock deformation. This current situation was not considered in this analysis. Therefore, the comparison between the analysis result and the field subsidence observations earlier than 2002 would be meaningful.

Figure 19 shows the elevation change history at well B of each cavern obtained from the field measurement. There are unusual surface heaves in October 1992 and February 2001. The elevations recorded in January 1992 would be in error because the January 1992 data show a sudden drop in elevation, whereas the October data seems to be in line with the rates previously measured. As for the February 2001 data, (A) this time frame correlates to the probable time of injection wells to the south initiating waste disposal within the caprock, (B) the offsite vertical datum has been disturbed several times throughout the history of the site, so the benchmark reference point may have been reset or the survey team chose to use a different offsite benchmark than what was previously used for calibrating surveys [Lord, 2011b].

Because of the reasons above, the predicted subsidence results at 7.67 years after the initial leach was completed are compared to the field subsidence measurement in December 1996 which is 7.67 years since April 1989. The field data are only available at the monument locations as shown in Figure 20, because the subsidence survey was conducted at the wells A and B of each cavern earlier than February 2001. Figure 21 shows the predicted surface subsidence at the lines correspond to the West-Ease cross-sections #1, #2, and #3 in Figure 11 with the field data at the monument locations in Figure 20 as a function of distance from Cavern 108, which is located at the middle of fourteen caverns, in December 1996. The field data are close to the predicted subsidence results. Therefore, this model approximation is reasonable to use to investigate the interbed behavior because this subsidence is caused by the creep closure of underground openings in response to the state of stress in the salt surrounding the caverns.

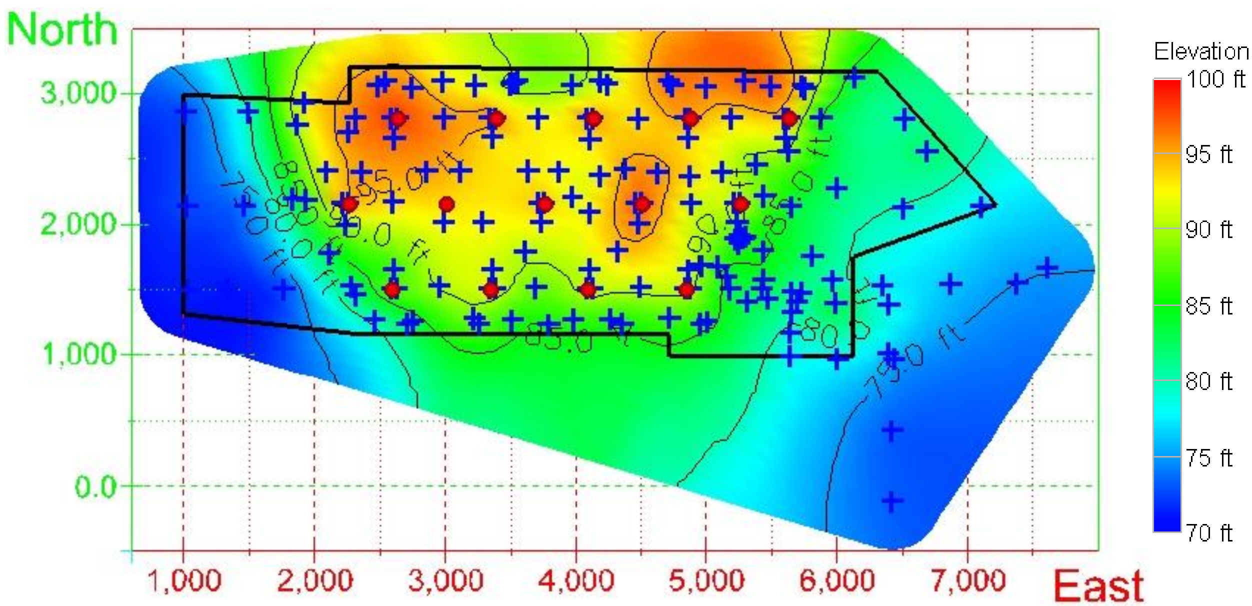

Figure 17: Contour plot of the March 2011 elevation data [Lord, 2011]. Monument locations are noted by crosses. Cavern well locations are depicted as red circles.

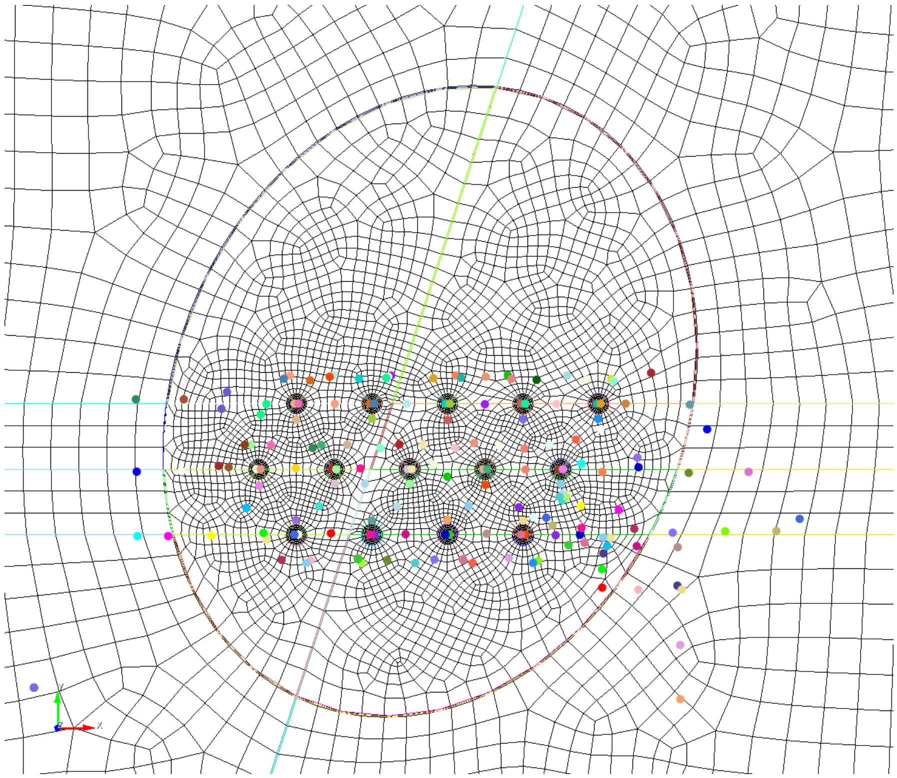

Figure 18: Monument locations (noted by colorful dots) on the mesh at present (March 2011).

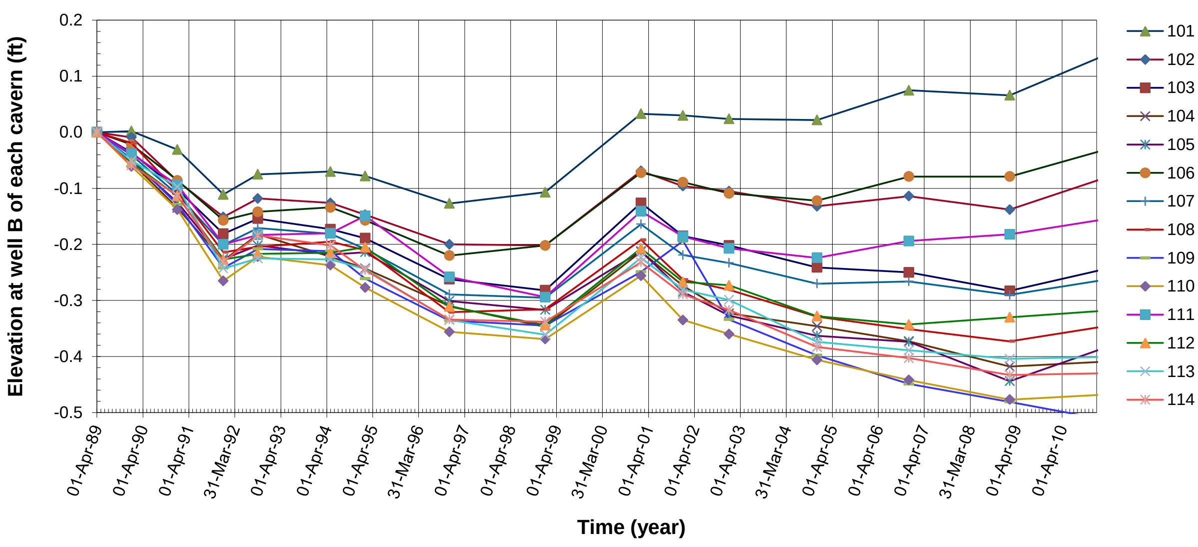

Figure 19 Elevation changes at well B of each cavern.

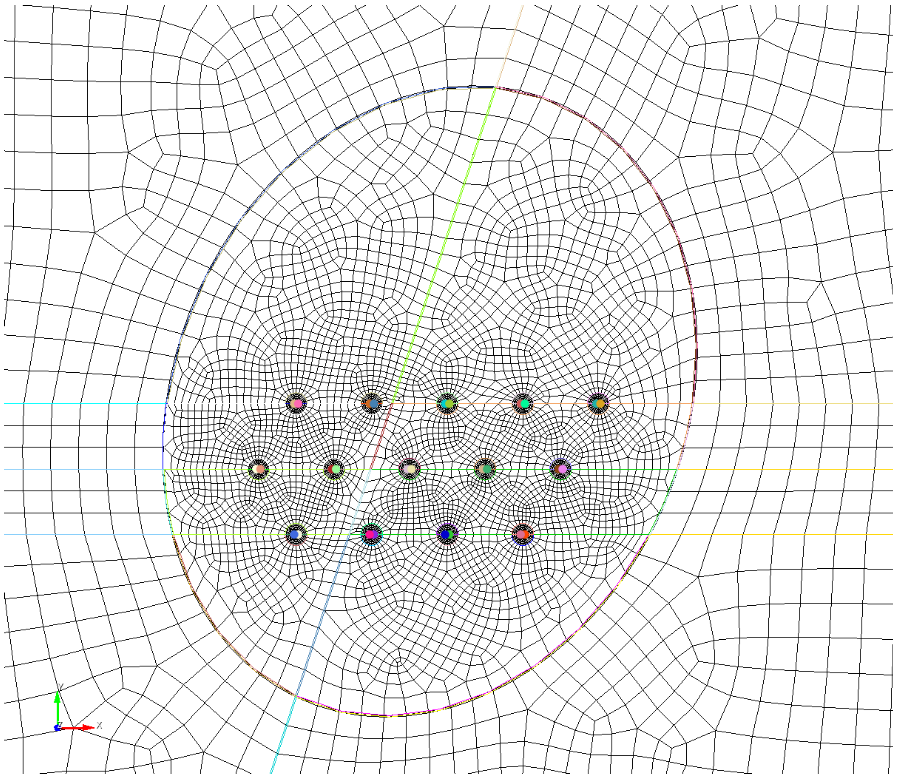

Figure 20: Available monument locations (noted by colored dots) on the mesh before February 2001.

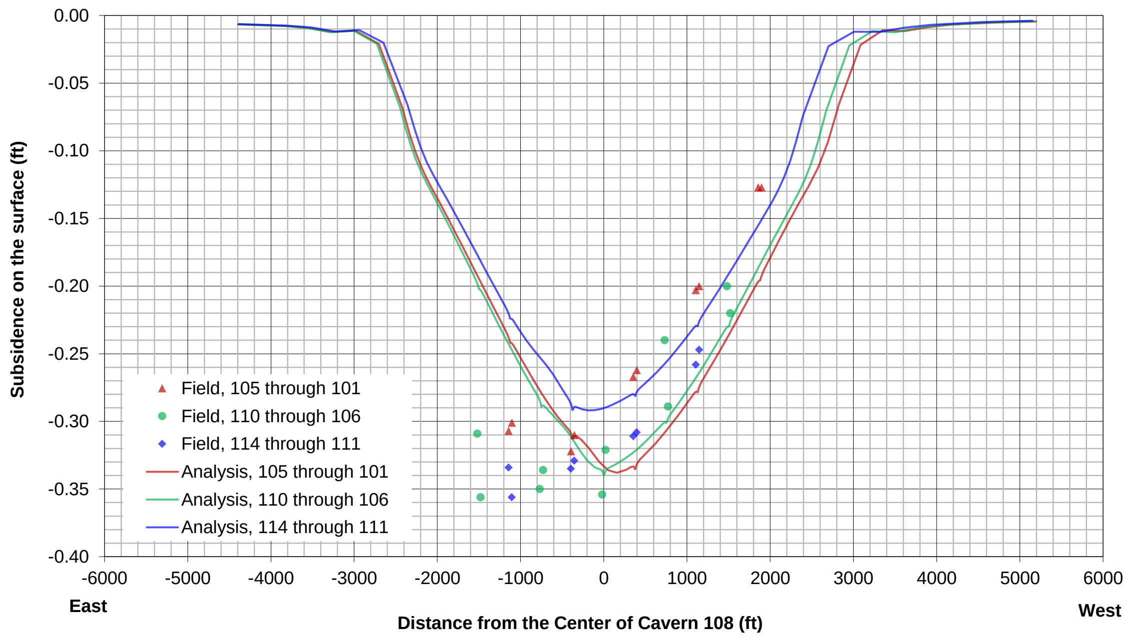

Figure 21: Predicted surface subsidence on the lines correspond to the East-West cross-sections #1, #2, and #3 in Figure 11 with the field data at the monument locations in Figure 20 as a function of distance from Cavern 108 in December 1996.

5. ANALYSIS RESULTS

Results from the simulations using the global model for the equivalent steel casing and cement annulus are presented in this section. The primary quantity of interest is the condition of the casing after slippage of the interbed due to salt creep closure.

5.1. Displacements of Salt Dome Top and Caprock Bottom

The displacements in X-, Y-, and Z-directions are calculated at Nodes N_{CM}, N_{CI}, N_{SI} and N_{SM} in Figure 22 for fourteen wellbores. To figure out the relative movement between the salt dome top and the caprock bottom above the center of each cavern, the displacements at Nodes N_{CI} (caprock bottom) and N_{SI} (salt dome top) are calculated over time. The relative horizontal displacement between N_{CI} and N_{SI} is considered key data for determining the outside diameter (OD) of the steel casing which will be inserted into the existing damaged inner steel casing (ID=12.515", OD=13-3/8") for remediation. The displacement history data at Nodes N_{CM} and N_{SM}, which will correspond to the top and bottom of the wellbore model (Figure 23), respectively, will be applied to the wellbore model as prescribed boundary conditions for each cavern well. The detailed as-built double steel casing and cement annuli behaviors will be calculated through the single-cavern wellbore simulation with these displacement data in the next stage (not in this report).

Figure 24 shows the displacements in X-, Y-, and Z-directions at N_{CI} and N_{SI} as a function of time for Cavern 108 as an example. As for the DZ***s at the caprock bottom (DZ_CI) and salt top (DZ_SI) in Figure 24, the subsidence rate of the salt top is faster than the caprock. The salt top subsides because the volume of caverns below the salt top decrease with time due to salt creep closure. However, the caprock does not subside with the same rate of the salt top because the caprock is thick and stiff. This discrepancy produces a deformation of the well. The deformed wellbore may fail at some time. The oil leaks occur when a wellbore fails. The displacements of N_{SI} relative to N_{CI} are calculated as shown Figure 25. The differences between DX_CI and DX_SI; DY_CI and DY_SI, are smaller than the difference between DZ_CI and DZ_SI in 24. Therefore, the relative displacements of DX and DY in Figure 25 are changed around zero, while DZ increases with time. The horizontal movement of the salt top (N_{SI}) relative to the caprock bottom (N_{CI}) is less than the vertical movement of the salt top. That is, the vertical deformation of wellbore of BH108 is larger than the horizontal deformation. Therefore, wellbore of BH108 is predicted to fail due to the tensile deformation.

Figure 26 shows the displacements in X-, Y-, and Z-directions at N_{CI} and N_{SI} as a function of time for Cavern 101 as an example. As for the DXs and DYs at the caprock bottom and salt top in Figure 26, the salt top (DX_SI) moves in a negative X-direction and the caprock bottom (DX_CI) moves in a positive X-direction, and the movement rates are similar. Both salt top (DY_SI) and caprock bottom (DY_CI) move in negative Y-direction, and the movement rate of the salt top is larger than the caprock bottom. The displacements of N_{SI} relative to N_{CI} are calculated as shown Figure 27. The relative displacements of DX and DY are larger than DZ with time. The horizontal movement of the salt top (N_{SI}) relative to the caprock bottom (N_{CI}) is

*** DX, DY, and DZ are X-, Y-, and Z- directional real displacement values which are differences between displacements at a time step and the 1st time step, respectively, because the initial jump occurs between the 1st step and the 2nd step due to the numerical solutions adjustments to get everything in equilibrium.

larger than the vertical movement. That is, the horizontal deformation of wellbore BH101 is larger than the vertical deformation. Even though both horizontal and vertical deformations contribute to failure of the wellbore, the horizontal deformation is dominant. Therefore the failure mode of BH101 wellbores could be shear deformation.

Figure 28 and Figure 29 show the relative displacements between N_{CM} and N_{SM} as a function of time for Caverns 105 and 109, respectively. The relative horizontal movements of salt top in X- and Y-directions at BH105 are larger than the vertical movement in Z-direction. Therefore, wellbore BH105B failed probably due to shear deformation. The relative horizontal movement of salt top in Y-direction at BH109 oscillates around zero. The horizontal movement of salt top in X-direction and the vertical movement in Z-direction increase with the similar rate. Thus wellbore BH109B failed probably due to the combination of shear and tensile deformations.

Figure 30 shows the predicted vertical displacements at Nodes N_{CI}, N_{SI}, N_{CM}, and N_{SM} in Figure 22 for Well 109 as a function of time. The displacements at nodes (N_{CI}, N_{CM}) in the caprock are almost the same, while the difference between the displacements at nodes (N_{SI}, N_{SM}) in the salt is getting larger with time. This implies the deformation of salt is larger than the caprock, and the caprock is relatively stiff. We recognize the salt deformation is the dominant factor of the wellbore deformation at the interbed from this phenomenon.

The displacements for fourteen cavern wells from the global model simulation are provided in Appendix II.

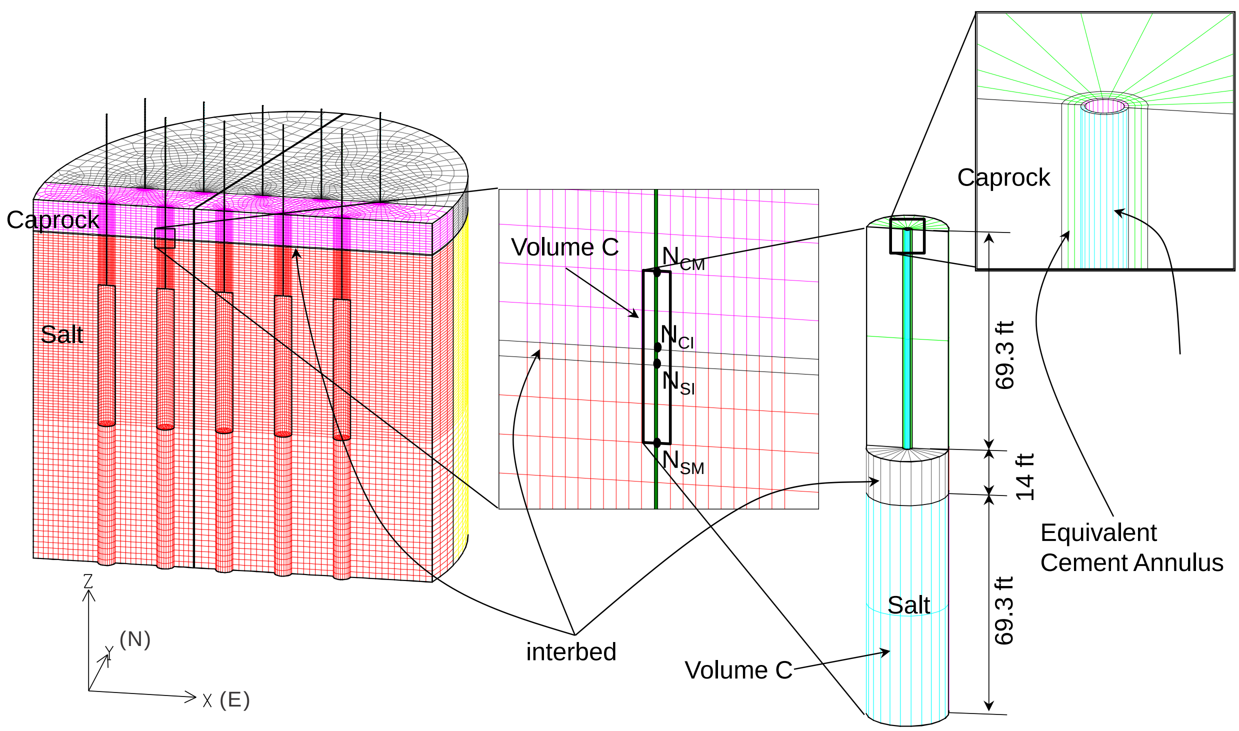

Figure 22: Configuration at the intersection of a wellbore and interbed to show the locations for calculating the predicted displacements

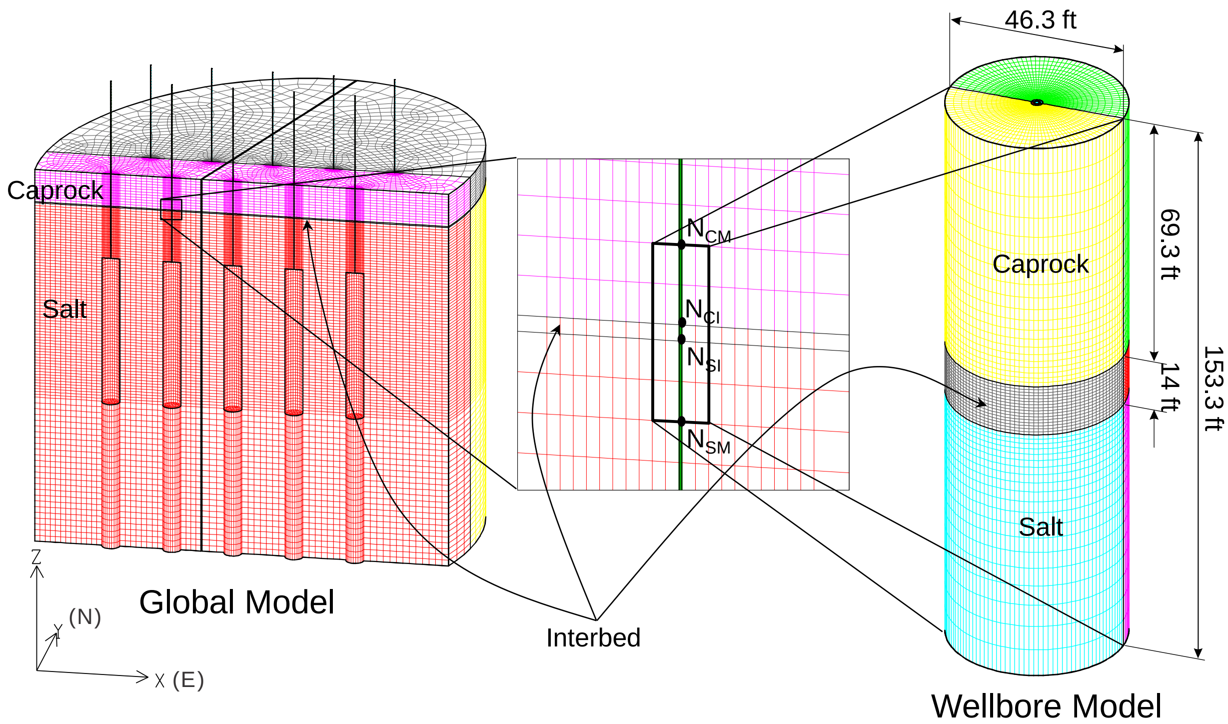

Figure 23: Relationship between global model and wellbore model

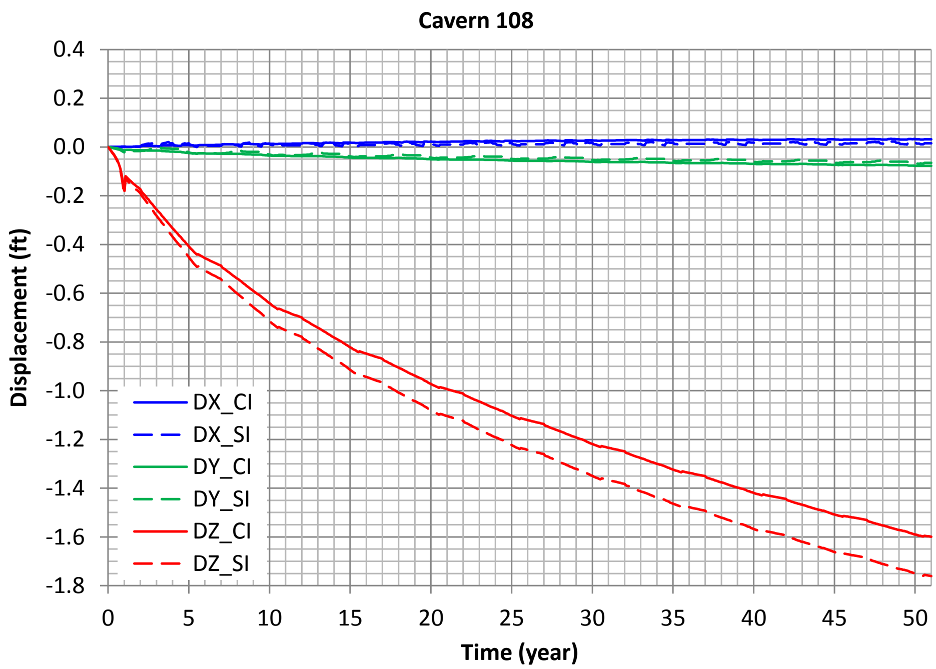

Figure 24: Predicted displacements at N_{CI} and N_{SI} in Figure 22 for Well 108 as a function of time

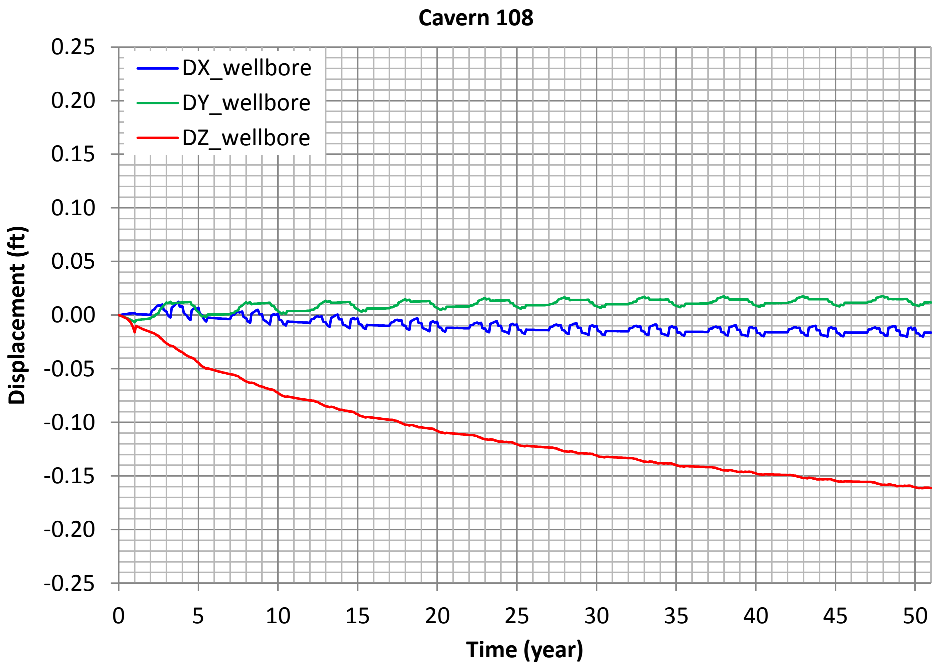

Figure 25: Predicted relative displacement between N_{CI} and N_{SI} in Figure 22 for Well 108 as a function of time

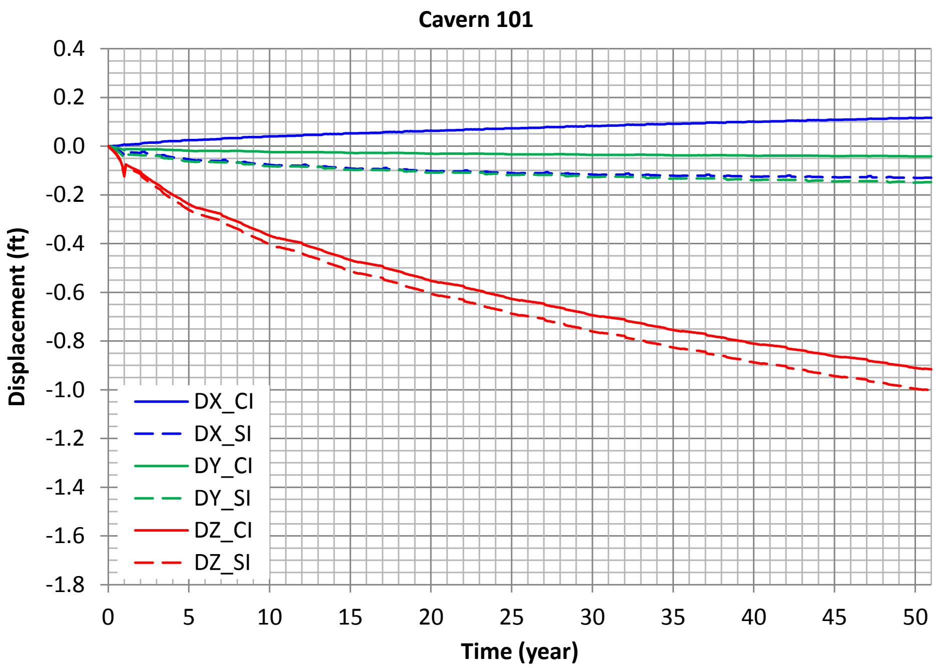

Figure 26: Predicted displacements at N_{CI} and N_{SI} in Figure 22 for Well 101 as a function of time

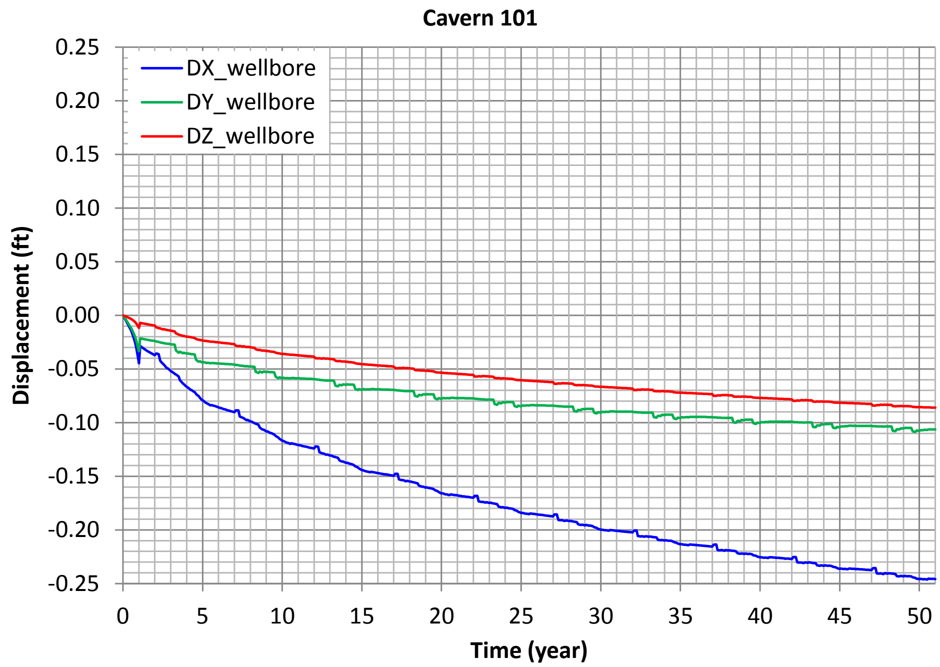

Figure 27: Predicted relative displacement between N_{Cl} and N_{Sl} in Figure 22 for Well 101 as a function of time

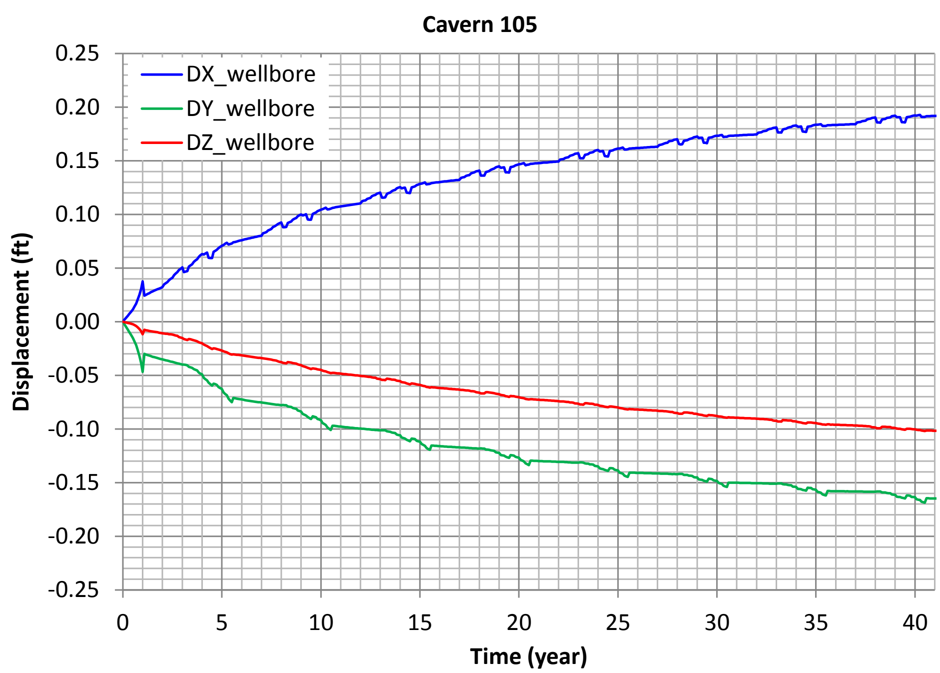

Figure 28: Predicted relative displacement between N_{Cl} and N_{Sl} in Figure 22 for Well 105 as a function of time

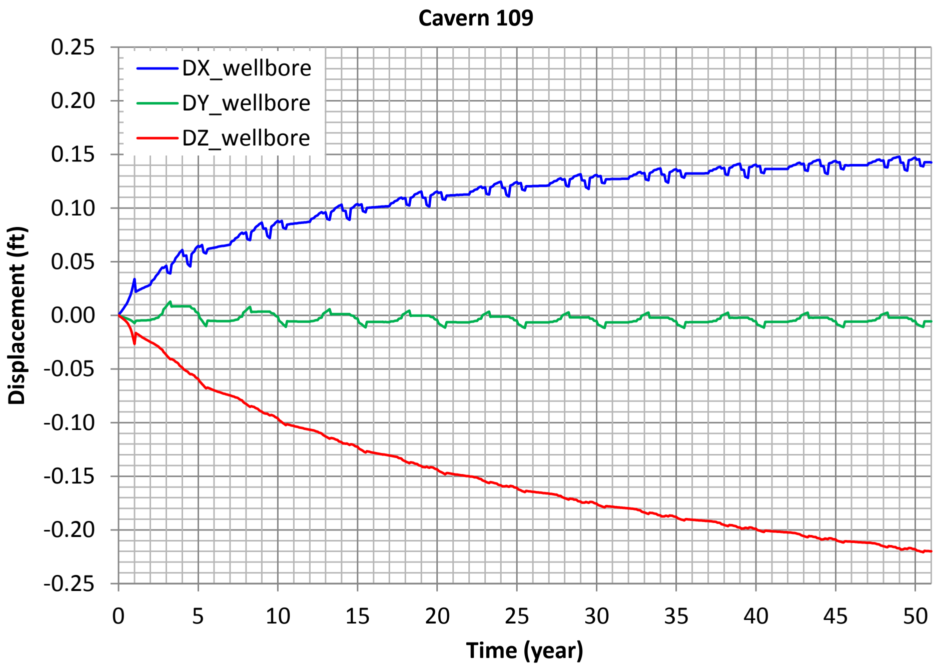

Figure 29: Predicted relative displacement between N_{CM} and N_{SM} in Figure 22 for Well 109 as a function of time

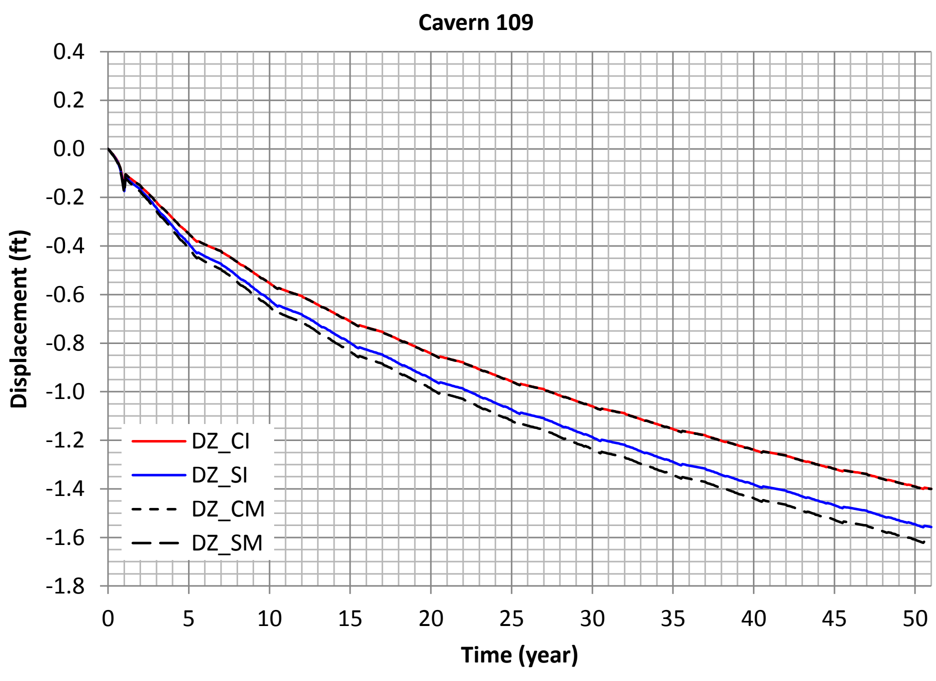

Figure 30: Predicted vertical displacements at Nodes N_{CI}, N_{SI}, N_{CM}, and N_{SM} for Well 109 as a function of time

5.2. Equivalent Plastic Strain

The equivalent plastic strain (EQPS) is calculated at every element of the equivalent steel casing in the cylindrical volume C as shown in Figure 22 at each time step. Volume C encloses the intersection of each wellbore and the interbed between salt dome top and caprock bottom. The element where the maximum EQPS occurs and the magnitude of EQPS are determined at each time step. Figure 31 shows the predicted maximum EQPS in the equivalent steel casing as a function of time for each cavern well. The number at each arrow indicates the cavern ID.

As mentioned in Section 1.1, oil leaks were found in well casings of Caverns 105 and 109 on December 3, 2009 and October 8, 2010, respectively. The oil leaks would occur when both double steel casings and double cement annuli have failed. The leak date of BH109B is regarded as the baseline in this simulation. October 8, 2010 calendar time corresponds to the simulation time of 21.25 years, because this simulation assumes that the initial leach start date for all caverns is July 13, 1990 as described in Section 2.3.2. The EQPS at 21.25 years is calculated to be about 0.79% as shown Figure 31. Then the value of 0.79% can be used as the EQPS failure criterion for the equivalent steel casings (red dashed line in Figure 31). When the EQPS failure criterion (0.79%) is applied to the curve for Well 105, the steel casing of Cavern 105 is predicted to fail at 21.42 years simulation time, i.e. the steel casing of Cavern 105 is predicted to fail on December 7, 2010 calendar time which is about one year different from the field observation (December 3, 2009). Taking into account the actual leach completion date of Cavern 105 is November 11, 1990 (four months later than July 13, 1990 assumed in this simulation), the actual difference is about 8 months. Therefore, the 0.79% EQPS failure criterion for the equivalent steel casing appears reasonable considering uncertainty of the assumptions mentioned in Section 2.1.

Figure 32 shows the predicted maximum EQPS in the equivalent cement annulus as a function of time for each cavern well around the interbed between the caprock bottom and the salt dome top. The number at each arrow indicates the cavern ID. When the 0.79% EQPS failure criterion is applied to the cement annulus, the cement annuli are predicted to fail between 9.58 years (February 9, 1999 calendar day) and 15.17 years (February 8, 2004 calendar day). In general, the cement is more brittle and the cement strength is less than steel. Therefore, the cement annuli should fail earlier than the predicted times using the steel EQPS criterion, i.e. the cement annuli should fail earlier than the steel casings. Steel casing failure should be the dominant factor for oil leaks to occur, i.e. we can conclude that oil leaks occur when the steel casing fails.

The oil leak date of each well can be determined by applying the 0.79% EQPS failure criterion to each curve in Figure 31 as listed in Table 7. To develop a separate well grading system based on the geomechanical simulations, the predicted leak dates obtained from Figure 31 are used for grading. The wellbores predicted to fail by July 2011 were given a score of 5, those predicted to fail by July 2014 a score of 4, those predicted to fail by July 2017 a score of 3, those predicted to fail by July 2020 a score of 2, those predicted to fail after July 2022 a score of 1. Table 7 lists the predicted leak date and the grade score for each cavern.

Color maps showing grading result for the DM casing inspection workbook [Wynn, 2012] is shown in Figure 33. In Table 7, differences between the DM and the grading from this simulation are identified in the column labeled “Similarity”. This simulation did not distinguish two wells for one cavern because one equivalent well, which integrates two wells together into, as described in Section 2.4. Two well are located at the center of each cavern and the distance between them is small compared to the cavern diameter. Thus the one predicted grade for two wells of each cavern would be reasonable. The grades for four cavern wells among fourteen caverns (BH102, BH103, BH108, and BH112) are different than the field observations. Taking into account uncertainty due to the assumptions in Section 2.1, the simulations results would be reasonable from a global perspective. We can recognize the dominant factor of the wellbore failure would be the subsidence of salt top due to cavern volume closure with time compared to the deformation of the thick and stiff caprock, from this simulation.

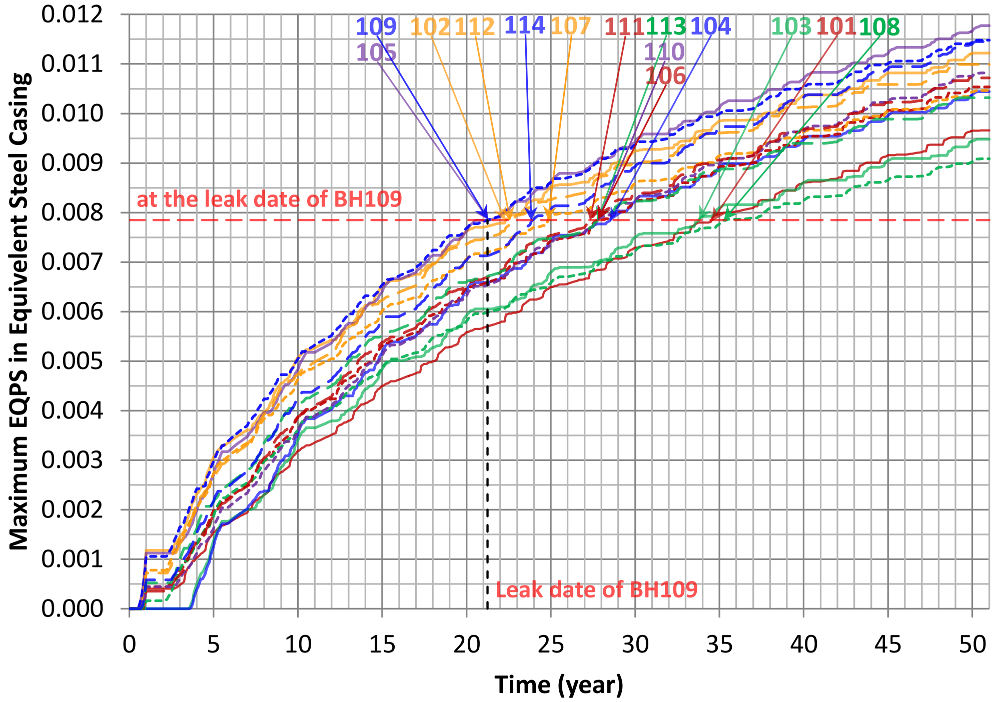

Figure 31: Predicted maximum EQPS in the equivalent steel casing as a function of time.

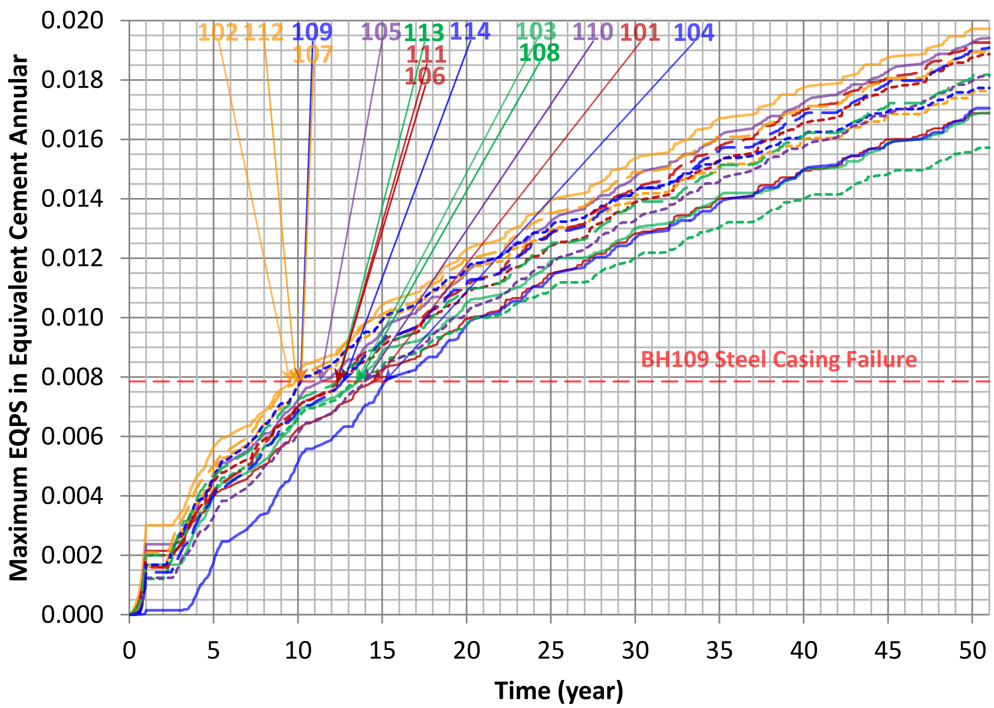

Figure 32: Predicted maximum EQPS in the equivalent cement annulus as a function of time.

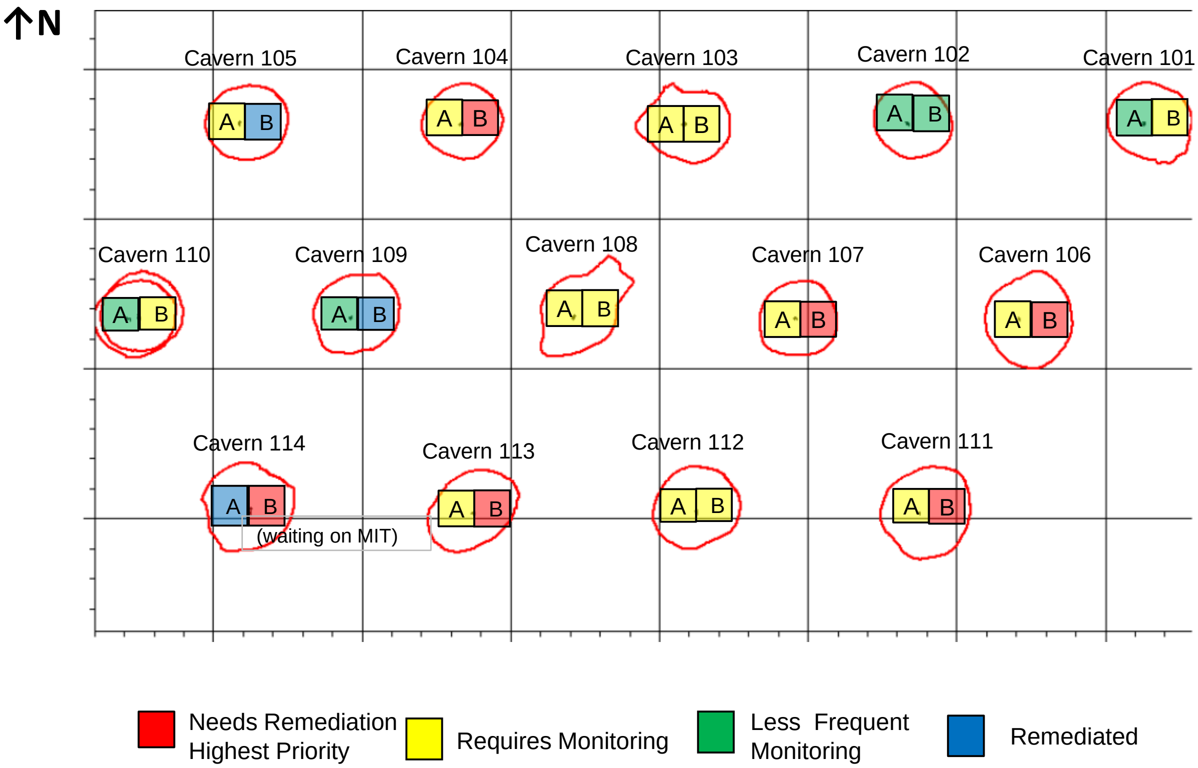

Figure 33: Big Hill caverns aerial view with Multi-Arm Caliper survey classification [Wynn, 2012].

Table 7: Predicted leak date and grading for the remediation with Multi-Arm Caliper survey result.

Cavern ID	Predicted Leak Date Simulation Time (year)	Predicted Leak Date Calendar Time	Grade (1~5)	Multi-Arm Caliper Survey	Similarity
101	34.58	Feb-2024	1	Well A - Less Frequent monitoring Well B - Requires monitoring	
102	22.33	Nov-2011	4	Well A - Less Frequent monitoring Well B - Less Frequent monitoring	Different
103	33.83	May-2023	1	Well A - Requires Monitoring Well B - Requires Monitoring	Different
104	28.58	Feb-2018	2	Well A - Requires Monitoring Well B - Needs remediation	
105	21.42	Dec-2010	5	Well A - Requires Monitoring Well B - Failed, Remediated	
106	27.75	Apr-2017	3	Well A - Requires Monitoring Well B - Needs remediation	
107	24.83	May-2014	4	Well A - Requires Monitoring Well B - Needs remediation	
108	35.50	Jan-2025	1	Well A - Requires Monitoring Well B - Requires Monitoring	Different
109	21.25	Oct-2010	5	Well A - Less Frequent monitoring Well B - Failed, Remediated	
110	27.83	May-2017	3	Well A - Less Frequent monitoring Well B - Requires monitoring	
111	27.33	Nov-2016	3	Well A - Requires Monitoring Well B - Needs remediation	
112	22.67	Mar-2012	4	Well A - Requires Monitoring Well B - Requires Monitoring	Different
113	27.83	May-2017	3	Well A - Requires Monitoring Well B - Needs remediation	
114	24.00	Jul-2013	4	Well A - Remediated Well B - Needs remediation	

5.3. Wellbore Deformations

Figure 34 shows the predicted deformations of the equivalent steel casing at the leak date of BH109B (October 8, 2010) around the intersection of each well and the interbed between the caprock bottom and salt top. Figure 37 through Figure 39 show the EQPS contours on the equivalent steel casing at the leak date of BH109B. The deformations are magnified by a factor of 20. Figure 35 and Figure 36 show the predicted relative horizontal displacements and vertical distances between the caprock bottom (N_{CI} in Figure 22) and salt top (N_{SI} in Figure 22) at each well as a function of time, respectively.

Each casing bottom placed in the salt moves toward Well 108 over time (Figure 34). The horizontal displacement of the bottom of Well 108 is predicted to be the least (Figure 35) while the vertical distance between the caprock bottom and salt top at Well 107 is predicted to be the most (Figure 36) because Caverns 107 and 108 are located in the middle of fourteen caverns. The horizontal displacement of the bottom of Wells 114, 105, 104, 102, 111, 101, and 110 are predicted to be relatively large (Figure 35), because Caverns 114, 105, 111, 101, and 110 make up a majority of the outermost caverns and Cavern 104 is closest to the fault.

The maximum EQPS (7.851 millistrain) is predicted to occur on Well 109 at the leak date of BH109 (Figure 31 and Figure 38). The leak is predicted to occur on east side of the well and is indicated by ✳. The minimum EQPS (5.698 millistrain) at the leak date of BH109 is predicted to occur on Well 101 (Figure 31 and Figure 37).

Figure 40 through Figure 42 show the EQPS contours on the equivalent steel casing at the leak date of each well. Comparing the calculated EQPS in the steel casing elements of each cavern well to the 7.851 millistrain EQPS failure criterion, the failure date, the deformed shapes, and the interbed elevations at that time can be predicted. The deformed shapes when the equivalent steel casing fails can also be generated and are shown in the figures. The red area (EQPS > 7.851 millistrain) indicates the steel casing failure. The steel casing of BH109 is predicted to be the first to fail at 21.25 simulation year (October 8, 2010) and then BH105 is predicted to fail two months later. The oil leaks at BH109 and BH105 are predicted to occur earlier than other wells, similar to field observations.

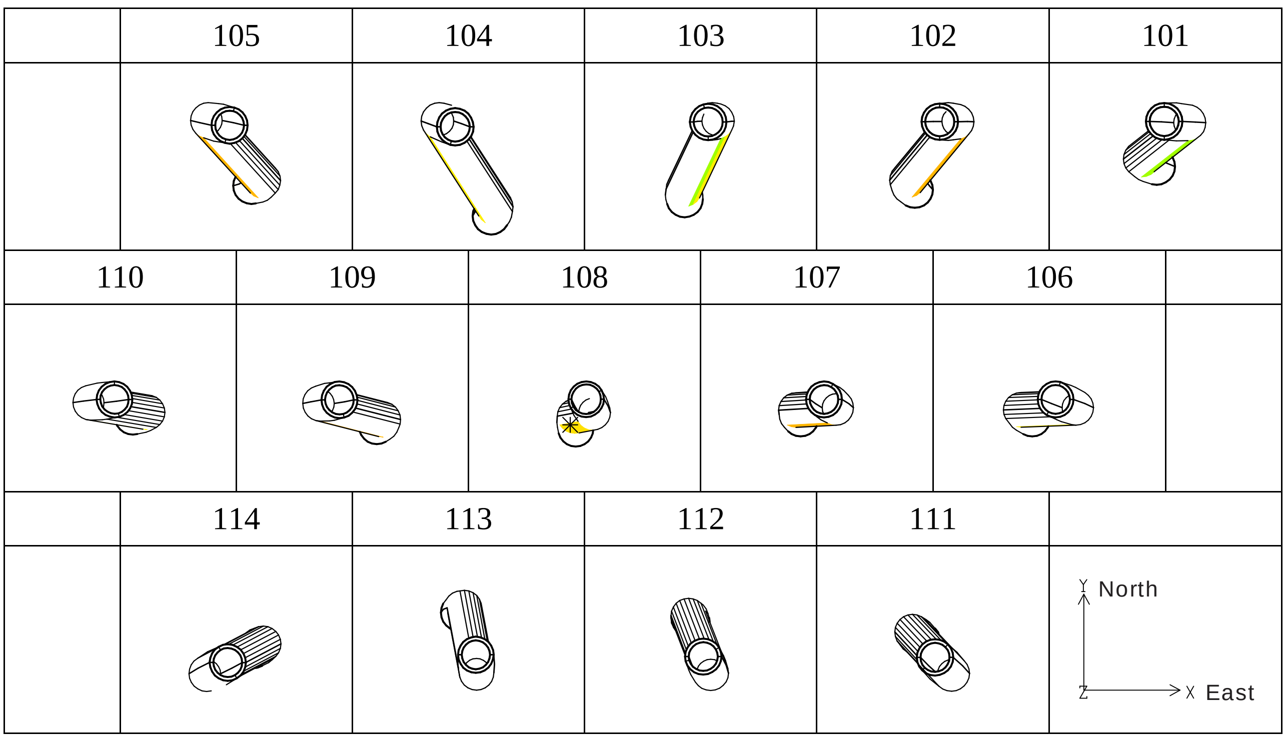

Figure 34: Predicted deformations of fourteen equivalent steel casings at the leak date of BH109B (October 8, 2010). Views are from the top of the well. Deformations are magnified by a factor of 20.

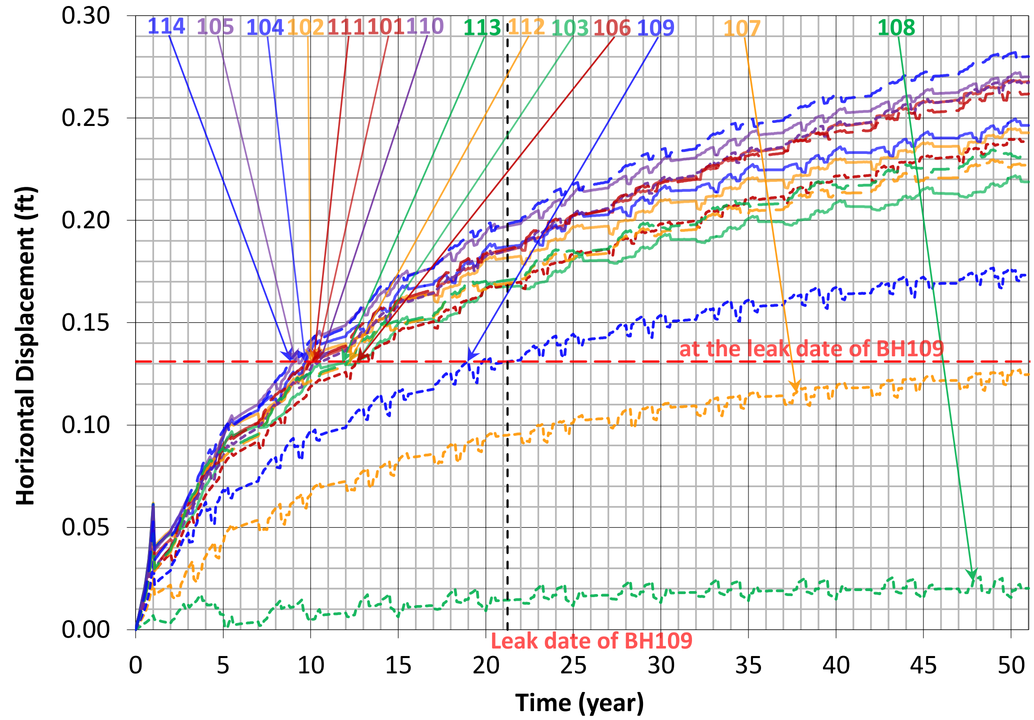

Figure 35: Predicted relative horizontal displacement between N_{CI} and N_{SI} in Figure 22 at each wellbore.

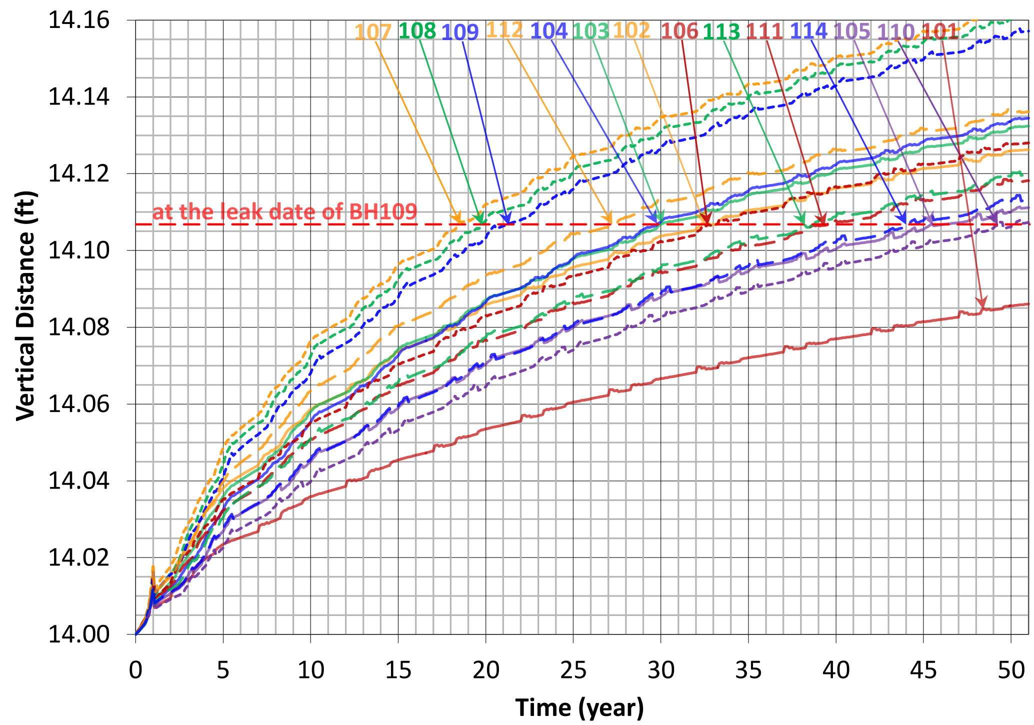

Figure 36: Predicted relative vertical distance between N_{CI} and N_{SI} in Figure 22 at each wellbore.

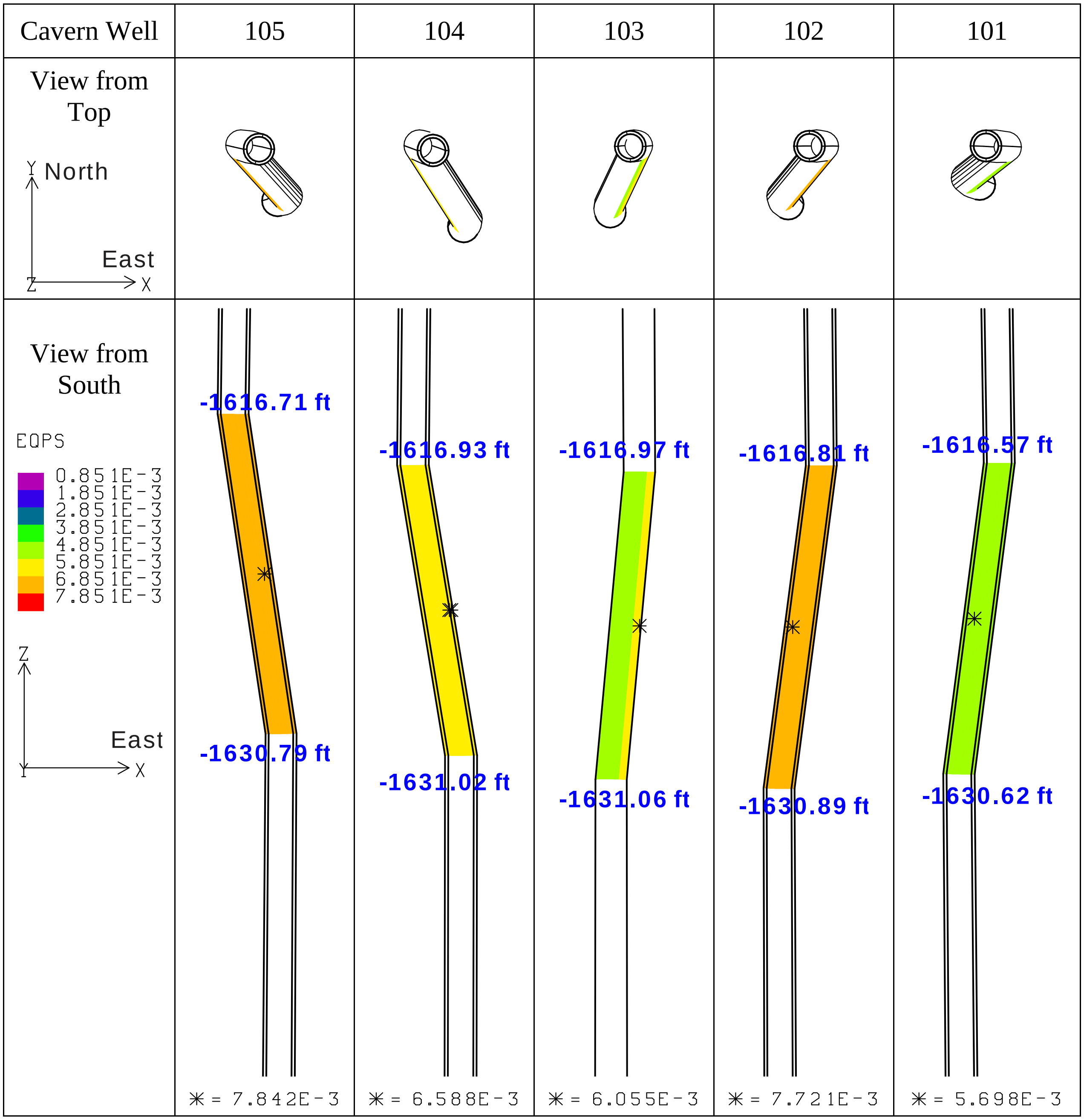

Figure 37: EQPS contours on the equivalent steel casings of BH101 through BH105 at the leak date of BH109B (10/8/2010). Views are from the top (upper row) and south (lower row). Deformations are magnified by a factor of 20. ✳ indicates the location where the maximum value of EQPS is predicted. The numbers in blue indicate the predicted depths of the top and bottom of the interbed.

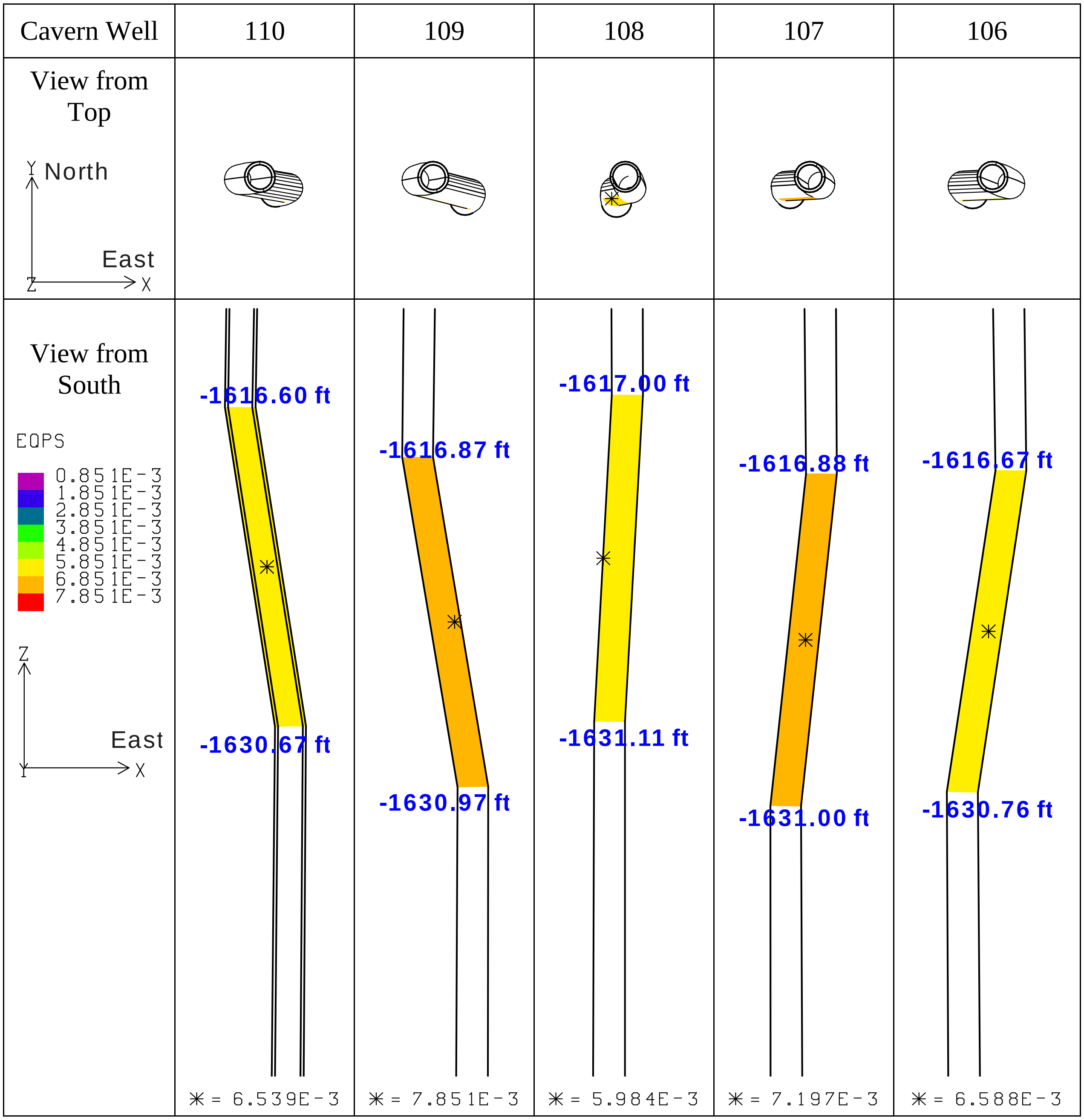

Figure 38: EQPS contours on the equivalent steel casings of BH106 through BH110 at the leak date of BH109B (10/8/2010). Views are from the top (upper row) and south (lower row). Deformations are magnified by a factor of 20. ✳ indicates the location where the maximum value of EQPS is predicted. The numbers in blue indicate the predicted depths of the top and bottom of the interbed.

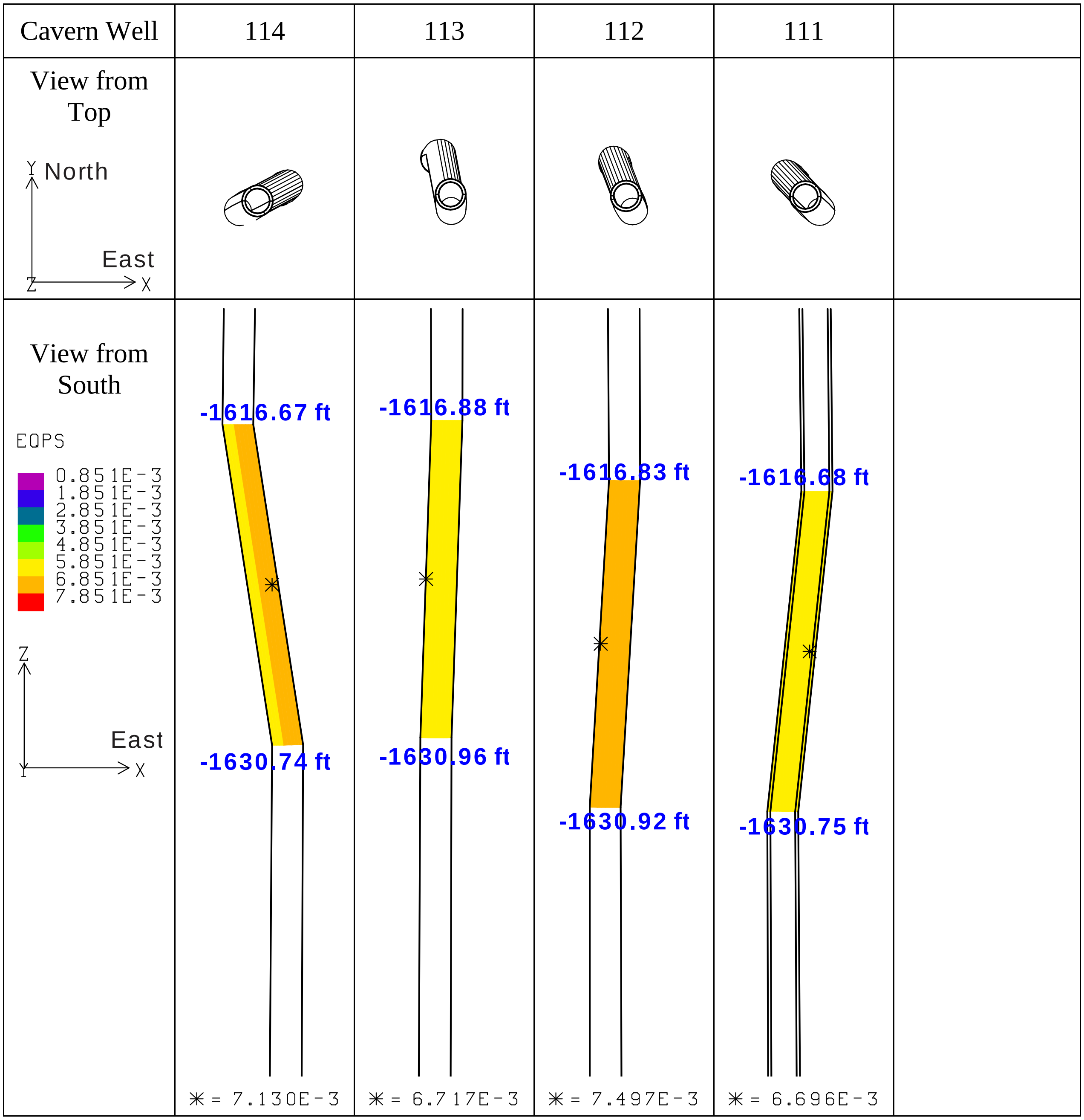

Figure 39: EQPS contours on the equivalent steel casings of BH111 through BH114 at the leak date of BH109B (10/8/2010). Views are from the top (upper row) and south (lower row). Deformations are magnified by a factor of 20. ✳ indicates the location where the maximum value of EQPS is predicted. The numbers in blue indicate the predicted depths of the top and bottom of the interbed.

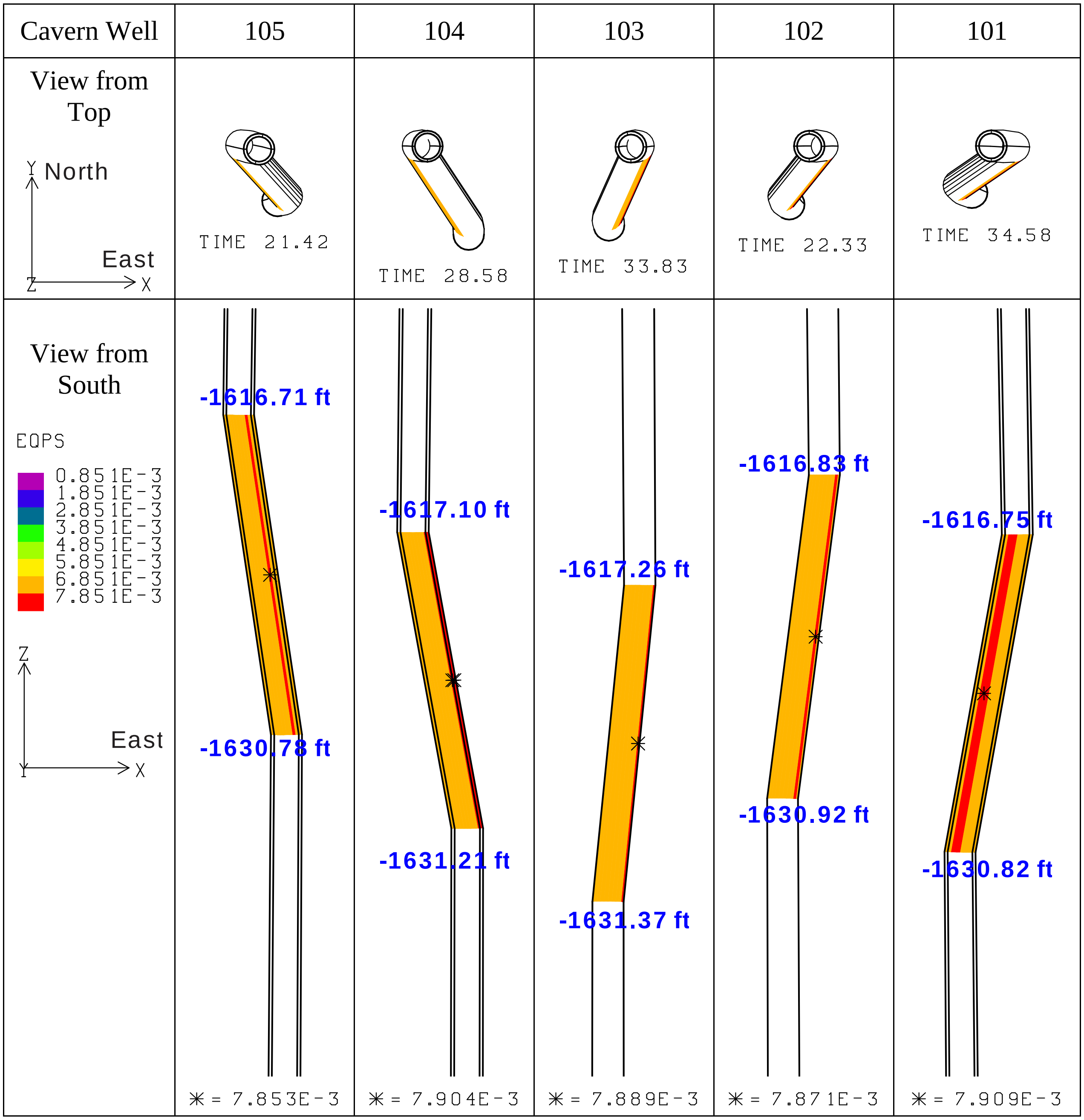

Figure 40: EQPS contours on the equivalent steel casings of BH101 through BH105 at the leak date of each cavern. Deformations are magnified by a factor of 20. Views are from the top (upper row) and south (lower row). ✳ indicates the location where the maximum value of EQPS is predicted. The numbers in blue indicate the predicted depths of the top and bottom of the interbed. Time unit is year.

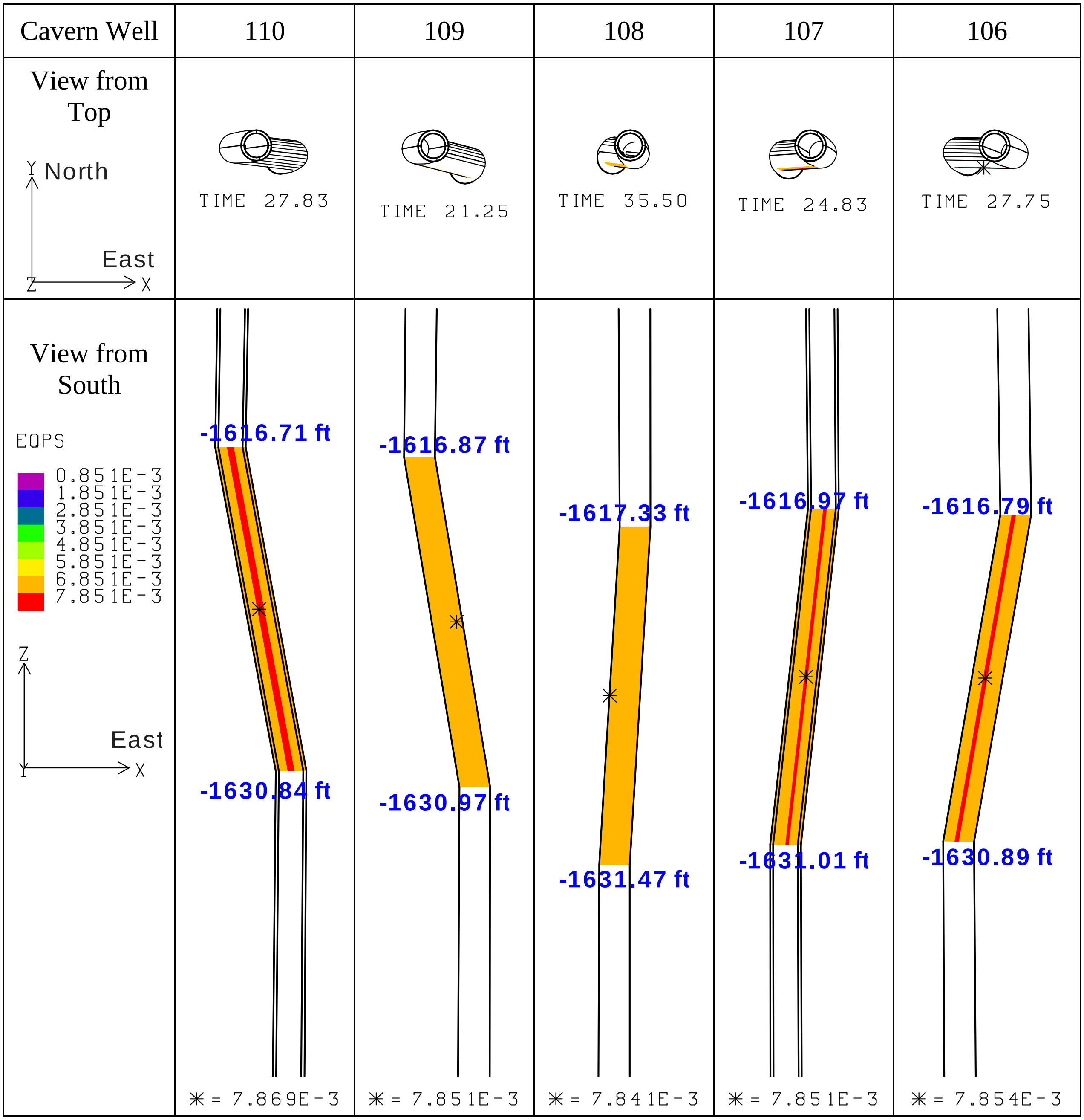

Figure 41: EQPS contours on the equivalent steel casings of BH106 through BH110 at the leak date of each cavern. Deformations are magnified by a factor of 20. Views are from the top (upper row) and south (lower row). ✳ indicates the location where the maximum value of EQPS is predicted. The numbers in blue indicate the predicted depths of the top and bottom of the interbed. Time unit is year.

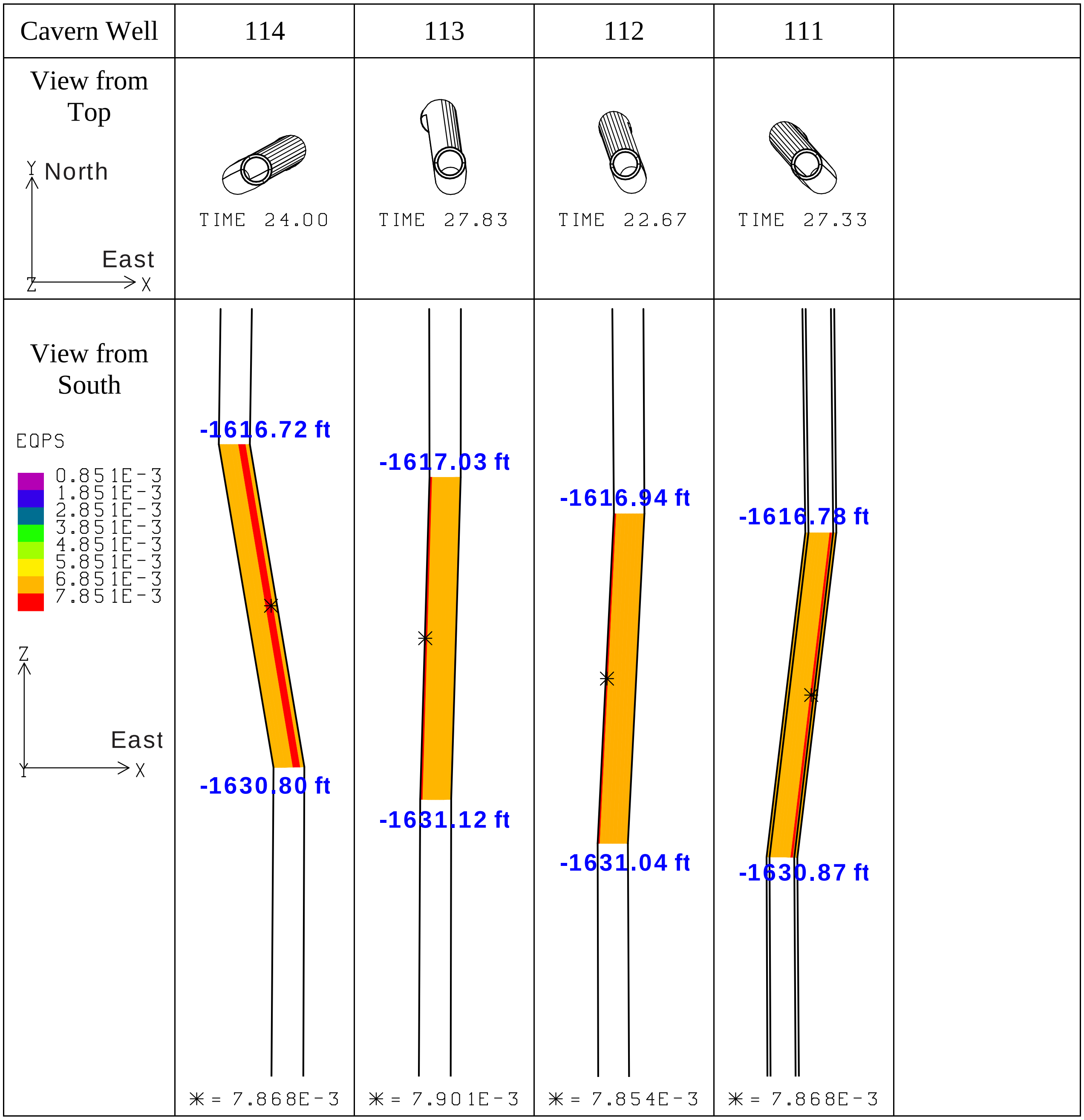

Figure 42: EQPS contours on the equivalent steel casings of BH111 through BH114 at the leak date of each cavern. Deformations are magnified by a factor of 20. Views are from the top (upper row) and south (lower row). ✳ indicates the location where the maximum value of EQPS is predicted. The numbers in blue indicate the predicted depths of the top and bottom of the interbed. Time unit is year.

5.4. Proposed Steel Casing Size for Remediation

Remediation of the well casings needs to be performed before the occurrence of an oil leak to prevent environmental contamination. Wellbores BH105B, BH109B, BH114A and BH114B were repaired on 06/22/2011, 04/28/2011, 01/22/2013, and 04/15/2013, respectively [DM, 2011a; DM, 2011b; DM, 2013a; DM, 2013b]. For remediation, a smaller size of steel casing was inserted into the damaged steel casing all the way down to the depth of about 2065 ft from the surface (Figure 43).

The horizontal deformation of the damaged steel casing at the interbed may limit the outside diameter of the inserted steel casing. Figure 44 shows the predicted horizontal deformation history of each well at the interbed, i.e. the horizontal distance change between N_{CI} and N_{SI} in Figure 22 over time. The dots indicate the predicted horizontal displacement when each well is predicted to fail (see Figure 31 and Table 7). The maximum horizontal displacement of a well does not occur always when the well is predicted to fail according to the EQPS criterion. For instance, the steel casing of BH114 is predicted to fail at 24.00 simulation years. The maximum horizontal displacement is calculated to be 0.2145 ft (2.574 in) at 24.00 simulation years. The maximum horizontal displacement of a well occurs when the well is predicted to fail in this case. Another example is the steel casing of BH109. It is predicted to fail at 21.25 simulation years with the horizontal displacement of 0.1311 ft (1.573 in), however the maximum horizontal displacement is calculated to be 0.1326 ft (1.591 inches) at 20.0 simulation years (see Figure 44). Therefore, for BH109 the relative displacement between N_{SI} and N_{CI} of 1.591 inches, at 20.0 simulation year is regarded as the maximum horizontal displacement the steel casing will undergo. Note that the horizontal displacement at 20.0 simulation years is calculated to be larger than at 21.25 simulation year, even though the predicted EQPS at 21.25 simulation years is larger than at 20.0 simulation years (see Figure 31). This is because the EQPS is calculated by the combination of the horizontal and vertical displacements.

The largest value of the maximum horizontal displacements for the fourteen wells occurs in Well 101 as shown in Figure 44. The maximum horizontal displacement of Well 101 is calculated to be 2.785 inches at 34.58 simulation years. Figure 45 shows a schematic diagram to show how the inside diameter of Well 101 steel casing decreases due to the horizontal deformation at 34.58 simulation years. The original ID of the 13-3/8” inner steel casing is 12.515 inches. The ID decreases to 9.730 inches due to 2.785 inches horizontal deformation. Therefore, the OD of the remediation steel casing would have to be less than 9.730 inches. A 10-3/4” steel casing (11.750 inches OD) would be hard to insert into the damaged wellbore and then the inserted steel casing will be pre-strained. The life of pre-strained steel casing will be shorter than the normal steel casing. A 9-5/8” steel casing could be used because the OD (9.625 inches) is less than 9.730 inches. In addition, a flush-joint connection (Figure 46) is required because the OD of the coupling is the same as the OD of the casing body. Other types of couplings can have ODs as large as 10-5/8” (Appendix I).

The predicted maximum horizontal displacement before each steel casing is predicted to fail is calculated as listed in Table 8. Considering inside diameter of inner steel casing of each wellbore, the casing size required for remediation is listed in Table 8. These proposed values are recommended to use as a reference. Field observation data and field engineer’s judgment should be more important for the field work.

Table 8: Proposed outside diameter of inserted steel casing for remediation.

Cavern	ID of Inner Steel Casing (inch)	Predicted Max. Hori. Displacement (inch)	Tolerance (inch)	Proposed Casing Size OD	Predicted Time at Max. Hori. Disp. (year)	Predicted Calendar Time at Max. Hori. Disp.
101	12.515	2.785	9.730	**9-5/8**	34.58	Feb-2024
102	12.515	2.190	10.325	**9-5/8**	22.00	Jul-2011
103	12.515	2.356	10.159	**9-5/8**	33.83	May-2023
104	12.515	2.059	10.456	**9-5/8**	28.58	Feb-2018
105	12.515	2.378	10.137	**9-5/8**	20.50	Jan-2010
106	12.515	2.293	10.222	**9-5/8**	27.75	Apr-2017
107	12.515	1.225	11.290	**10-3/4**	24.50	Jan-2014
108	12.515	0.296	12.219	**11-3/4**	33.25	Oct-2022
109	12.515	1.591	10.924	**10-3/4**	20.00	Jul-2009
110	12.515	2.546	9.969	**9-5/8**	27.83	May-2017
111	12.515	2.507	10.008	**9-5/8**	27.33	Nov-2016
112	12.515	2.125	10.390	**9-5/8**	22.67	Mar-2012
113	12.515	2.321	10.194	**9-5/8**	27.83	May-2017
114	12.515	2.574	9.941	**9-5/8**	24.00	Jul-2013

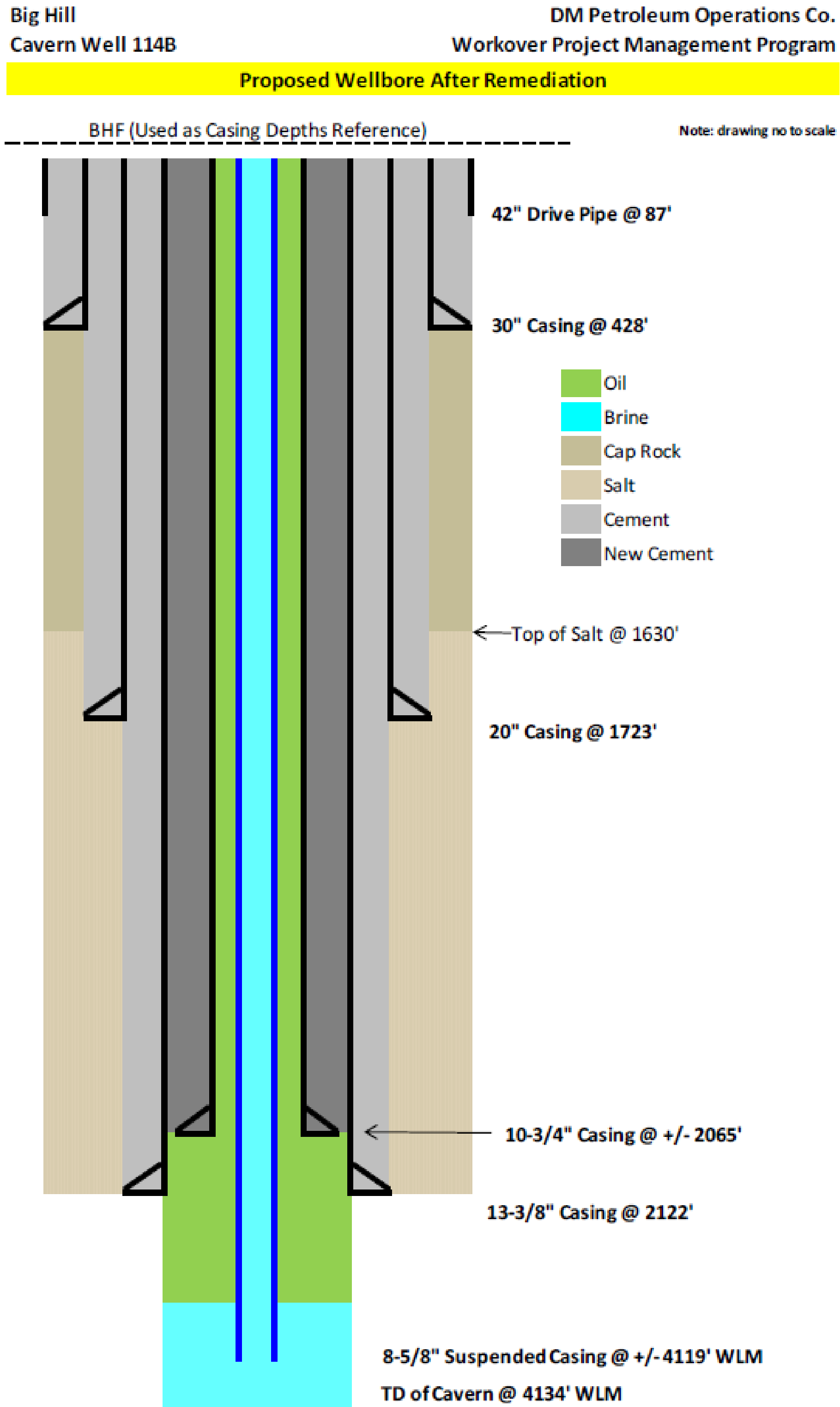

Figure 43: Proposed schematic of wellbore BH114B after remediation

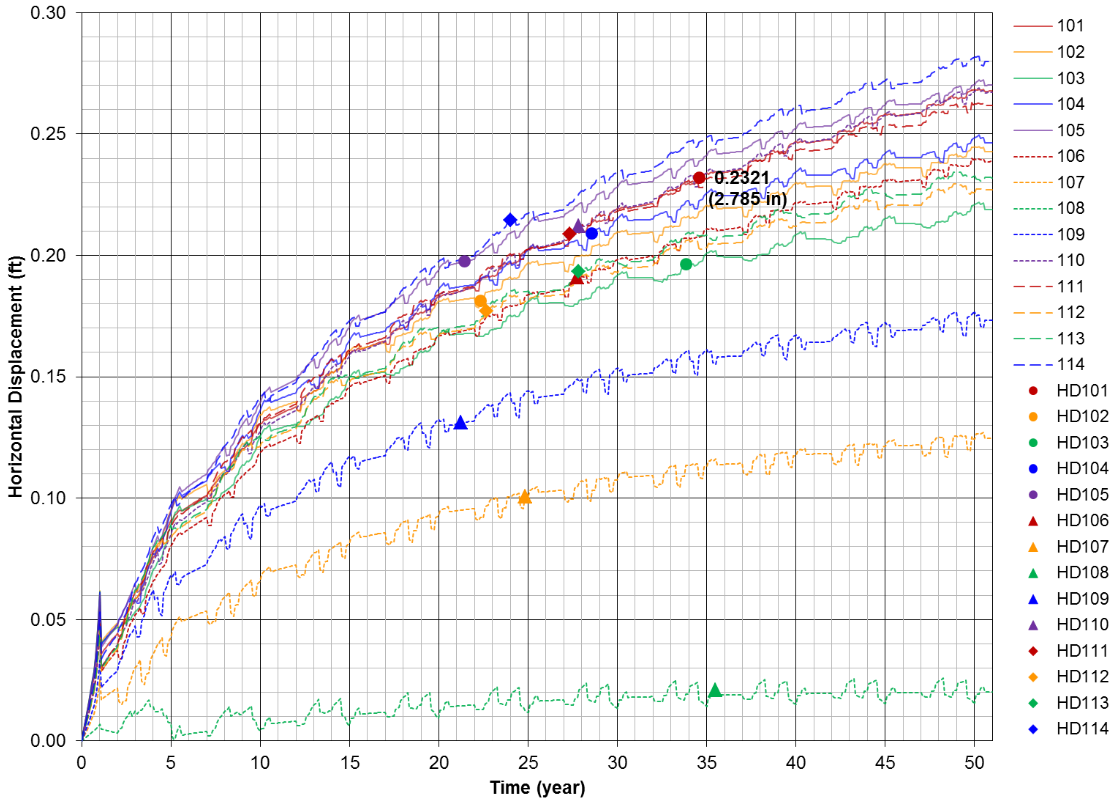

Figure 44: Predicted horizontal well deformations at the interbed as a function of time. The dots indicate the predicted horizontal displacement when each well is predicted to fail.

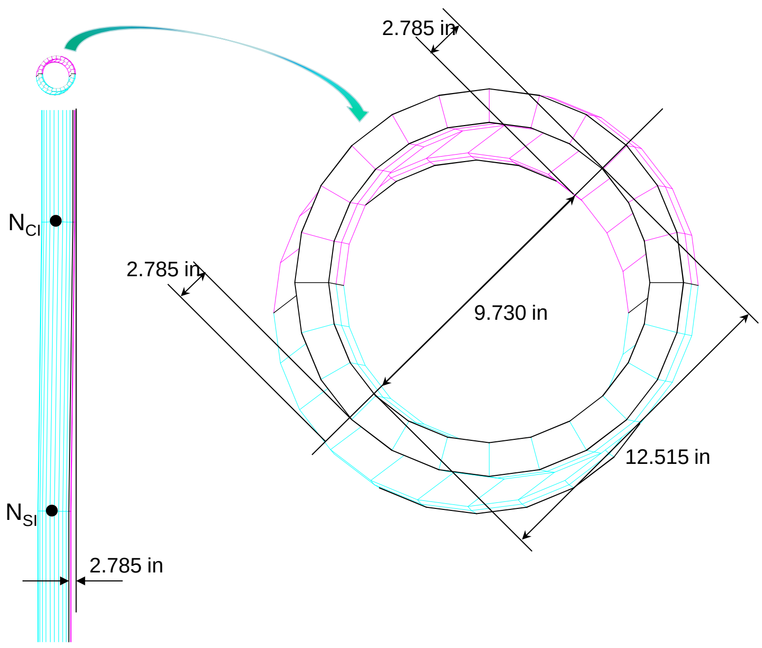

Figure 45: Schematic diagram showing the inside diameter of steel casing decrease due to the horizontal deformation at 34.58 simulation years for Well 101.

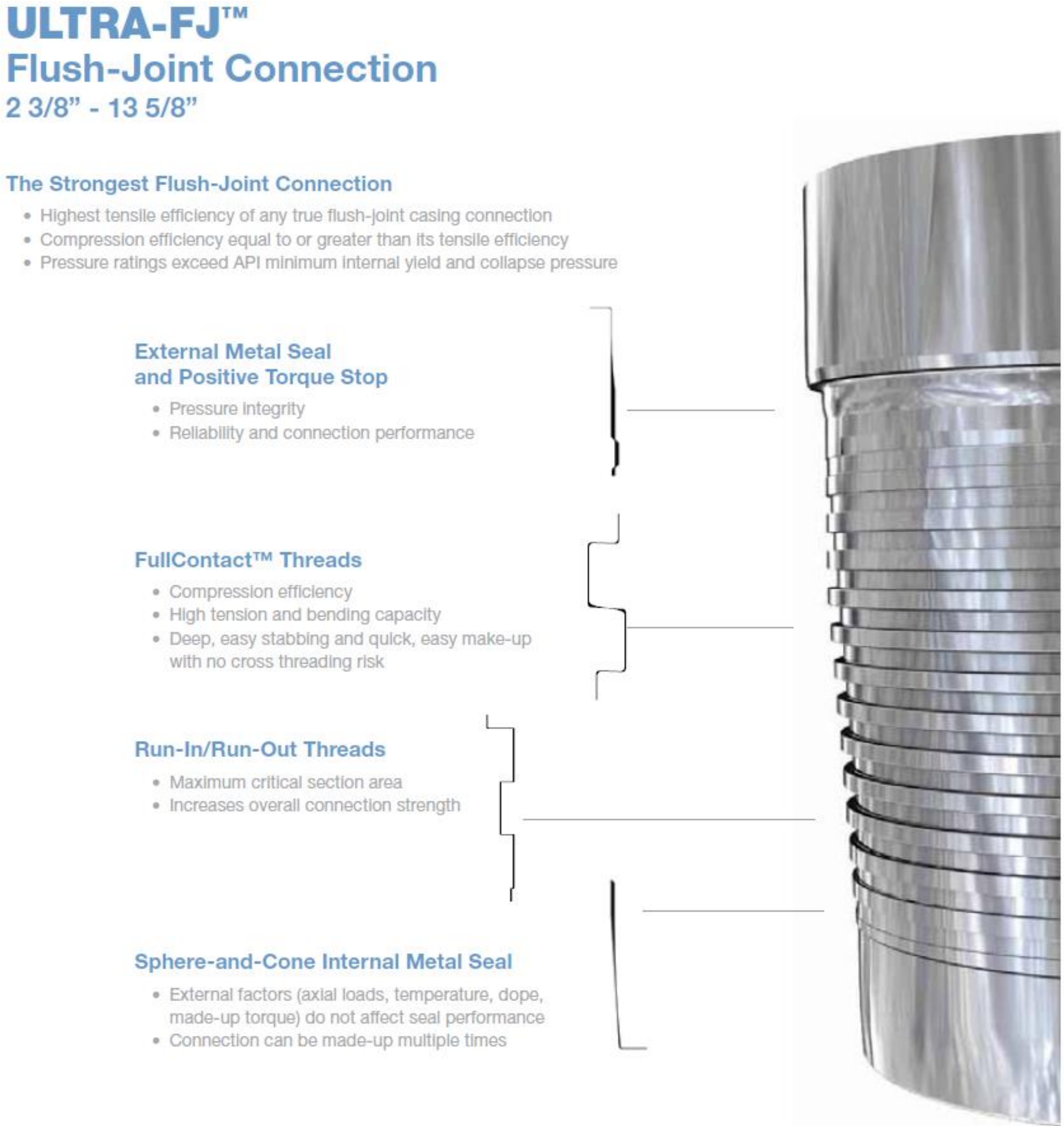

Figure 46: Flush-Joint Connection [TMK-Ipsco, 2013]

5.5. Comparison to the Field Observations

Weatherford's multi-sensor caliper (MSC) tool (Figure 47) provides an accurate internal casing profile from an array of independent measuring, precision calibrated, carbide-tipped feeler arms. Real-time monitoring of tool response enables the operator to perform multiple passes over anomalous features observed in the casing profile. The tool is available in 40- and 60-arm variants that can be used depending upon casing size to be logged. TVision analysis software classifies each casing joint with respect to the worst case defect found, providing a convenient joint-by-joint well summary. The analysis package can also graphically portray the casing as a 2D cross-section or 3D image to highlight anomalies. The wellbore measurement and onboard inclinometers supply data for a rigorous eccentricity correction algorithm, as well as the analysis of casing deformation [Weatherford, 2010].

Figures 48 through 53 show the comparisons of predicted equivalent steel casing deformation images to the MSC survey images for BH105A, BH105B, BH108A, BH109A, BH111A, and BH114A. The computational images are displayed as deformed equivalent steel casing with EQPS contours. Both computational and survey images are magnified by five.

The computational images match the survey images fairly well. In conclusion, the FEM model used in this study is considered to be reliable.

Figure 47: Weatherford's multi-sensor caliper [Weatherford, 2010]

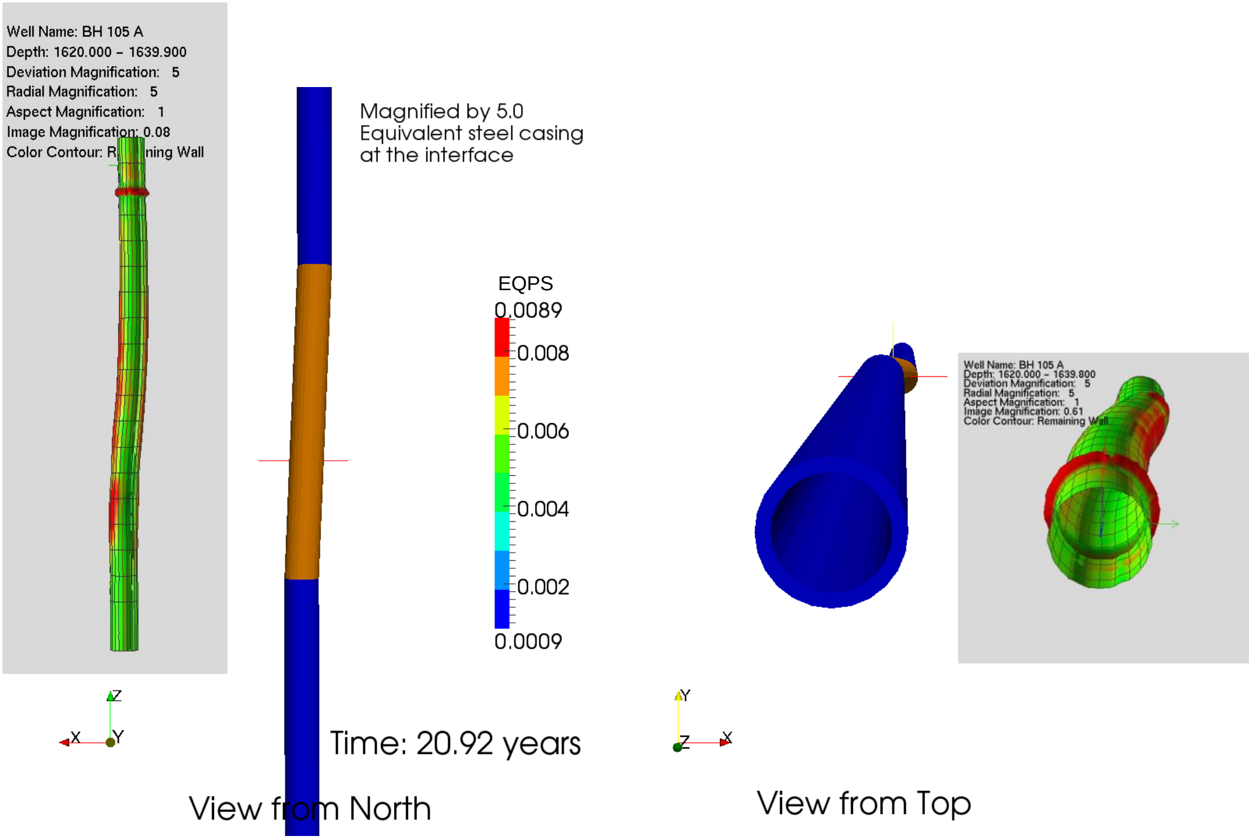

Figure 48: Comparison of predicted equivalent steel casing deformation of BH105A to the multi-arm caliper survey images on 5/25/2010 (about 20.92 simulation years).

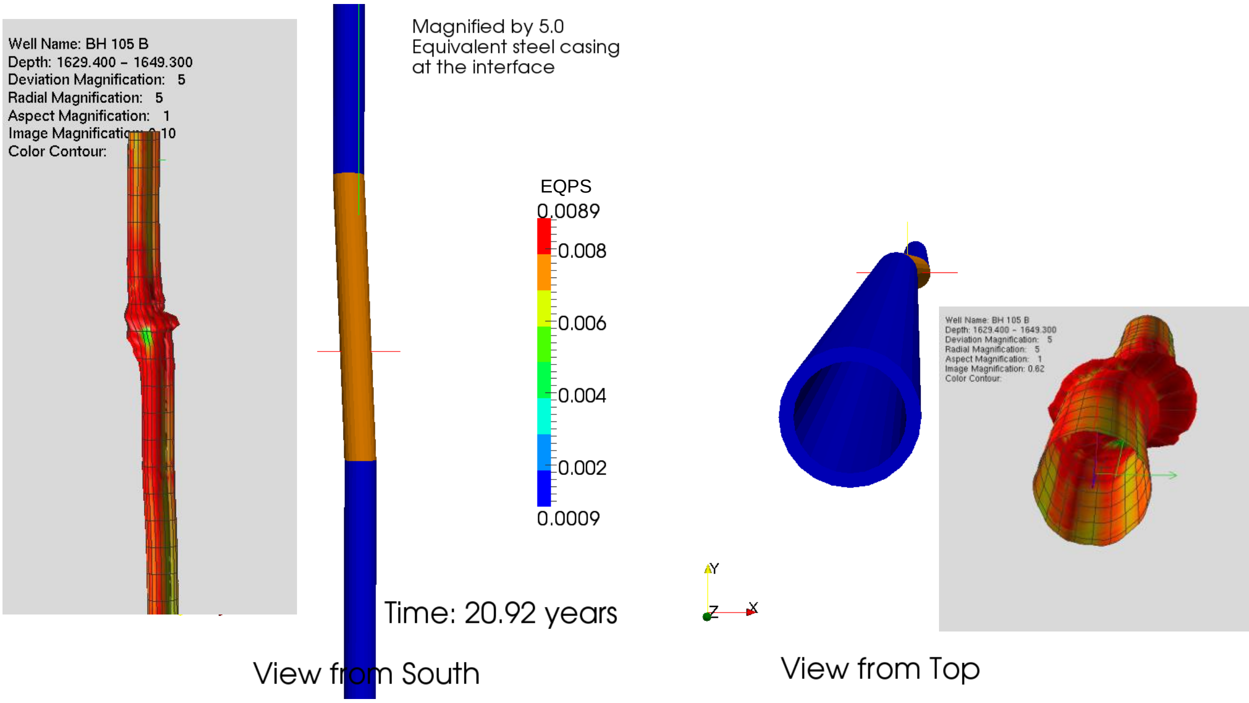

Figure 49: Comparison of predicted equivalent steel casing deformation of BH105B to the multi-arm caliper survey images on 6/6/2010 (about 20.92 simulation years).

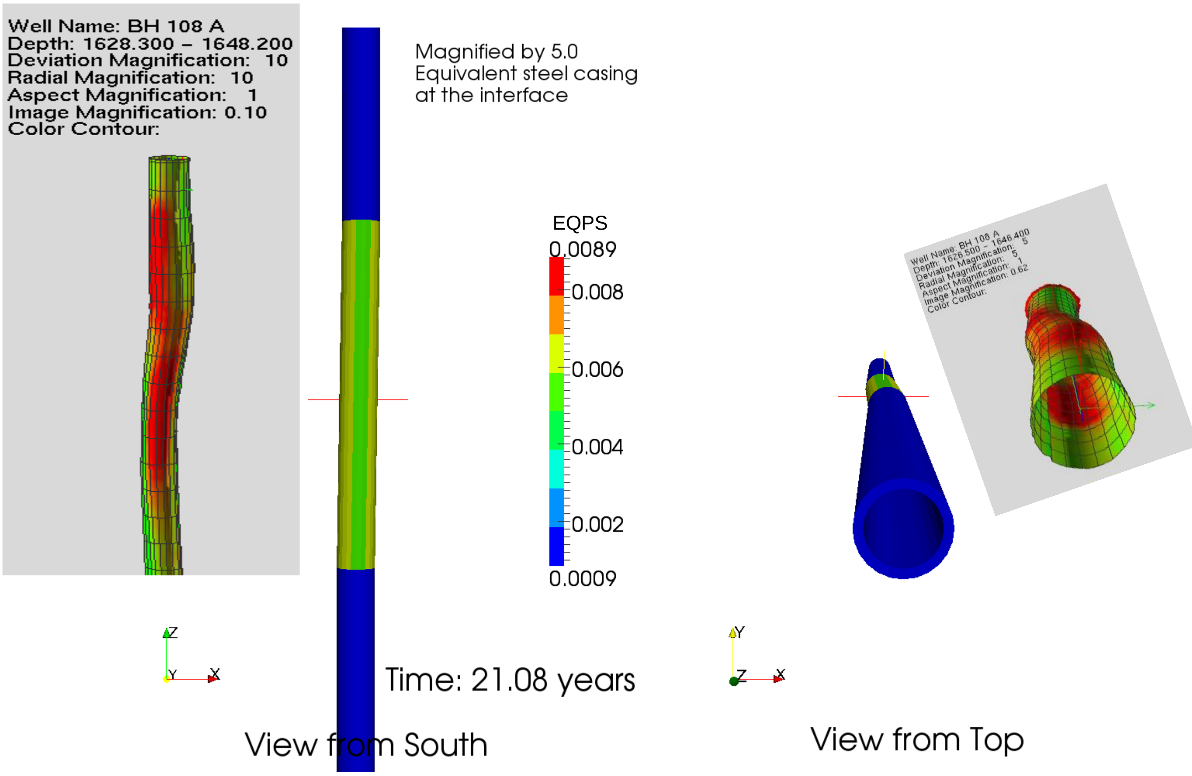

Figure 50: Comparison of predicted equivalent steel casing deformation of BH108A to the multi-arm caliper survey images on 7/13/2010 (about 21.08 simulation years).

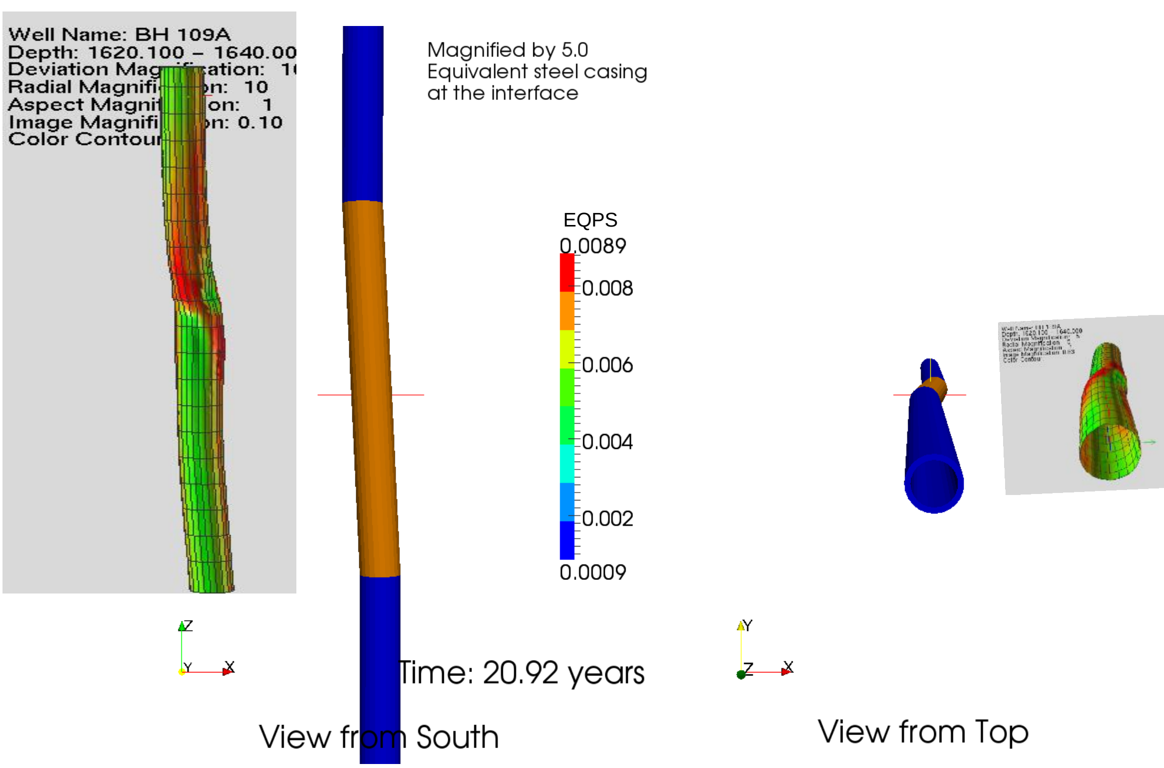

Figure 51: Comparison of predicted equivalent steel casing deformation of BH109A to the multi-arm caliper survey images on 6/29/2010 (about 20.92 simulation years).

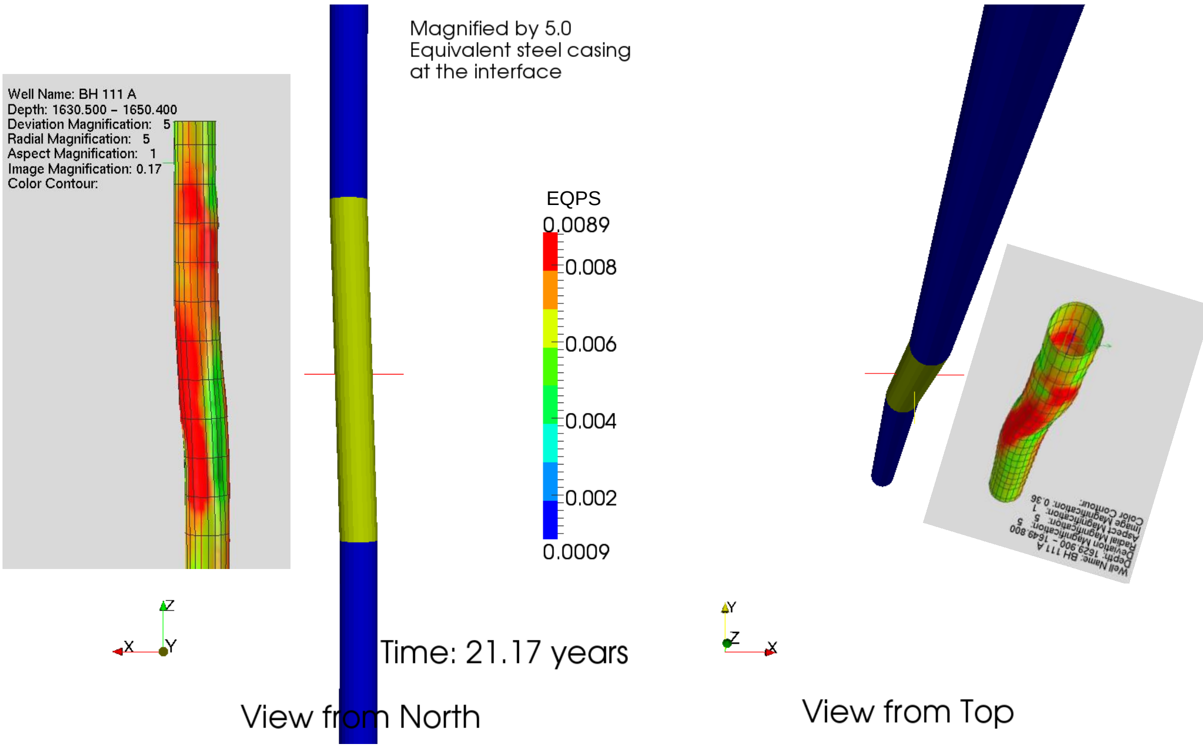

Figure 52: Comparison of predicted equivalent steel casing deformation of BH111A to the multi-arm caliper survey images on 9/8/2010 (about 21.17 simulation years).

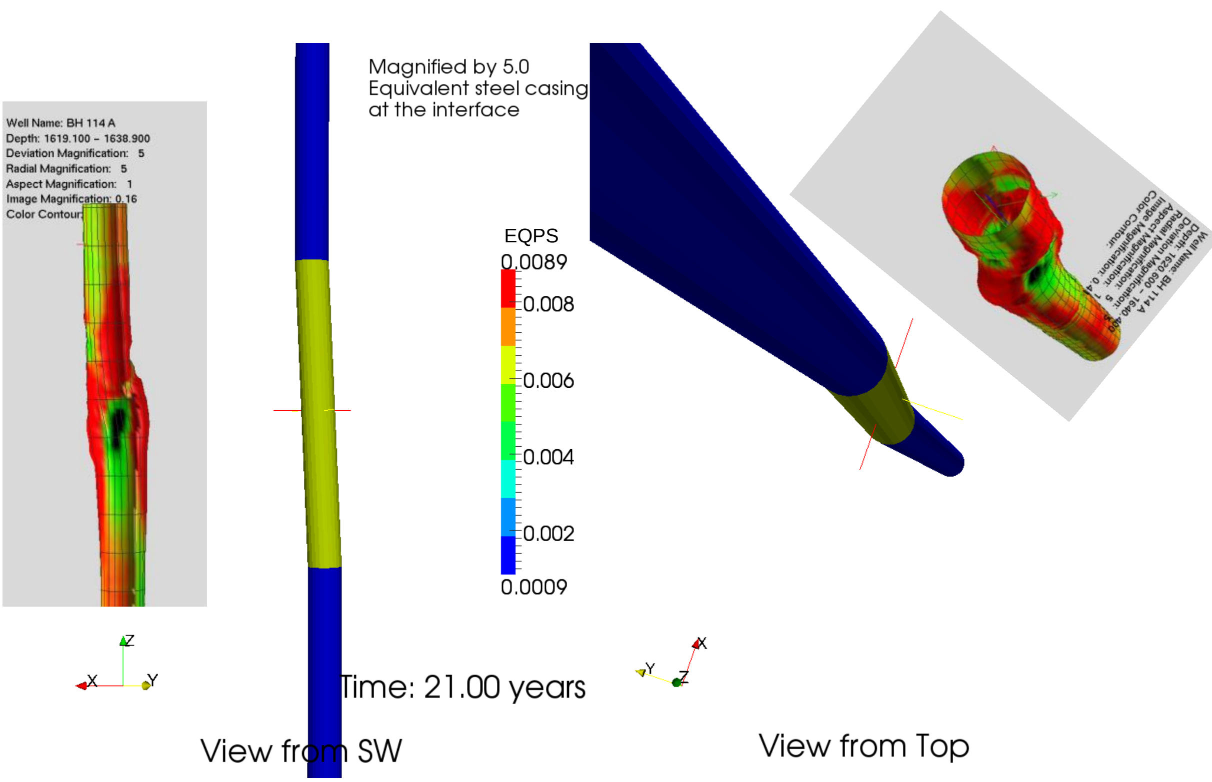

Figure 53: Comparison of predicted equivalent steel casing deformation of BH114A to the multi-arm caliper survey images on 7/14/2010 (about 21.00 simulation years).

5.6. Modeling Impact of Wellbore Block

To figure out how the wellbore impedes the movement of the salt dome top, a comparison of the analyses results from meshes with and without the wellbore blocks is needed. Figure 54 shows the overview of the finite element mesh of the stratigraphy and cavern field at BH without the wellbore block. The mesh consists of 920,589 elements, while the mesh containing the wellbore blocks consists of 1,012,932 elements (Figure 10).

Figure 55 shows the comparison of predicted total volumetric closure normalized by total initial volume of the fourteen caverns from the meshes with and without wellbore blocks. Two results are almost the same. This implies that the wellbore blocks do not affect the cavern volume closures.

Figure 56 through Figure 65 show the predicted relative displacements between N_{CM} and N_{SM}; N_{CI} and N_{SI} in 22 for BH104, BH105, BH108, BH109, and BH114 as a function of time. The solid and dashed lines indicate the results from the model with and without wellbore blocks, respectively. The predicted relative displacements at inside nodes N_{CM} and N_{SM} (69.3 ft apart from the top and bottom of interbed, respectively) are almost the same, while those at nodes N_{CI} and N_{SI} (on the top and bottom of interbed, respectively) are a little different. We recognize the stiff wellbore blocks impede obviously the movement of the salt top, however the amount of the impediment is too small. Therefore, the model omitting the wellbore blocks could be used for a simplified simulation. The model without wellbores would reduce the effort needed to construct it and save on computer run time, but the result would be not much different from the result from the model containing wellbore blocks.

The displacements at the top and bottom of interbed above the center of each cavern are calculated in this report. The predicted displacement data will be applied to the as-built wellbore model for each cavern well. The as-built casing behavior will be calculated in the next stage (not in this report). The predicted relative displacements between N_{CM} and N_{SM}; N_{CI} and N_{SI} in Figure 22 for fourteen cavern wells are provided in Appendix III.

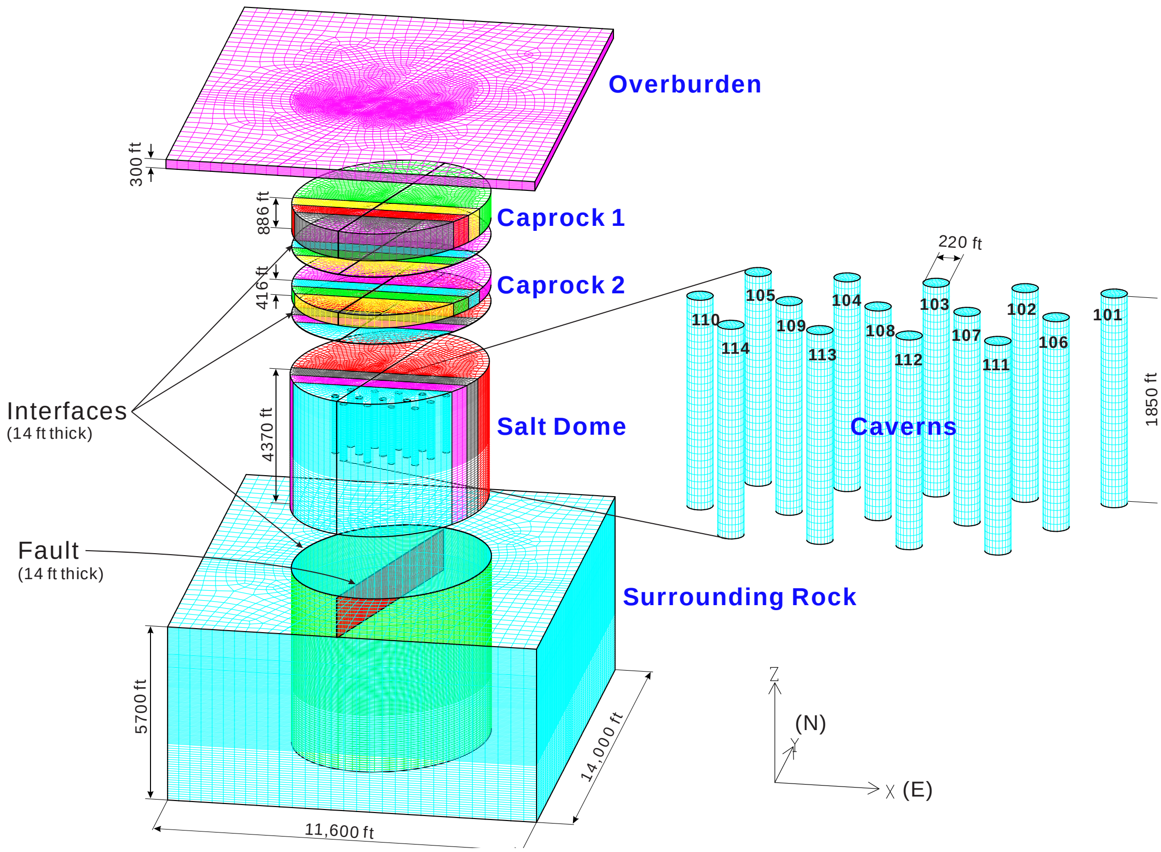

Figure 54: Overview of the finite element mesh of the stratigraphy and cavern field without wellbores at Big Hill.

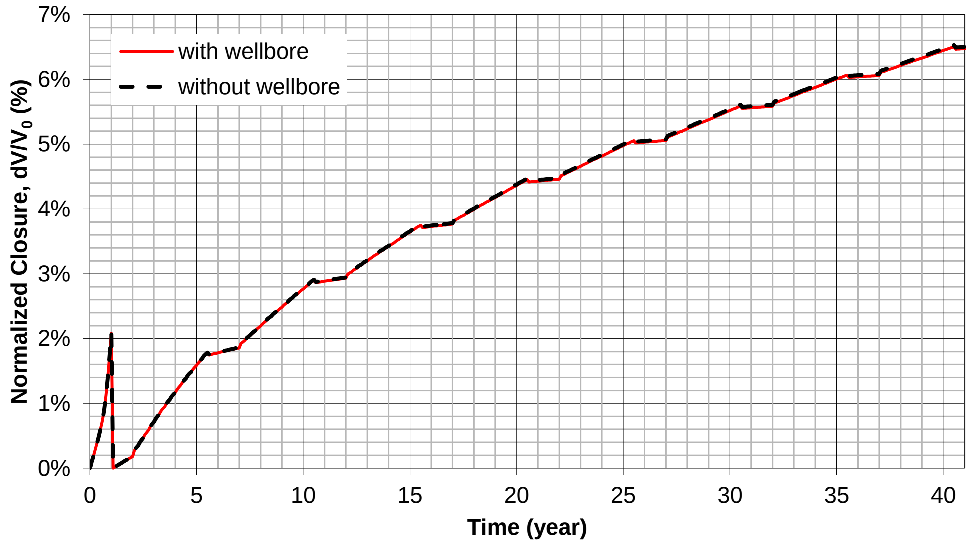

Figure 55: Comparison of predicted total volumetric closure normalized by total initial volume of the fourteen caverns calculated from the model with and without wellbore blocks.

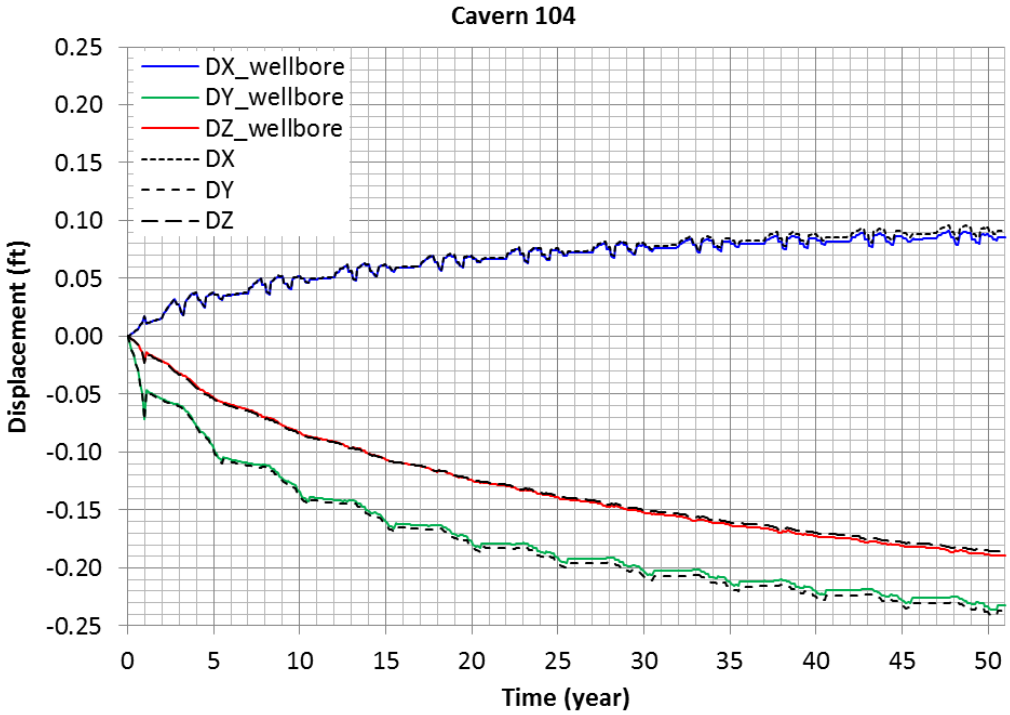

Figure 56: Predicted relative displacement between N_{CM} and N_{SM} in Figure 22 for BH104 as a function of time

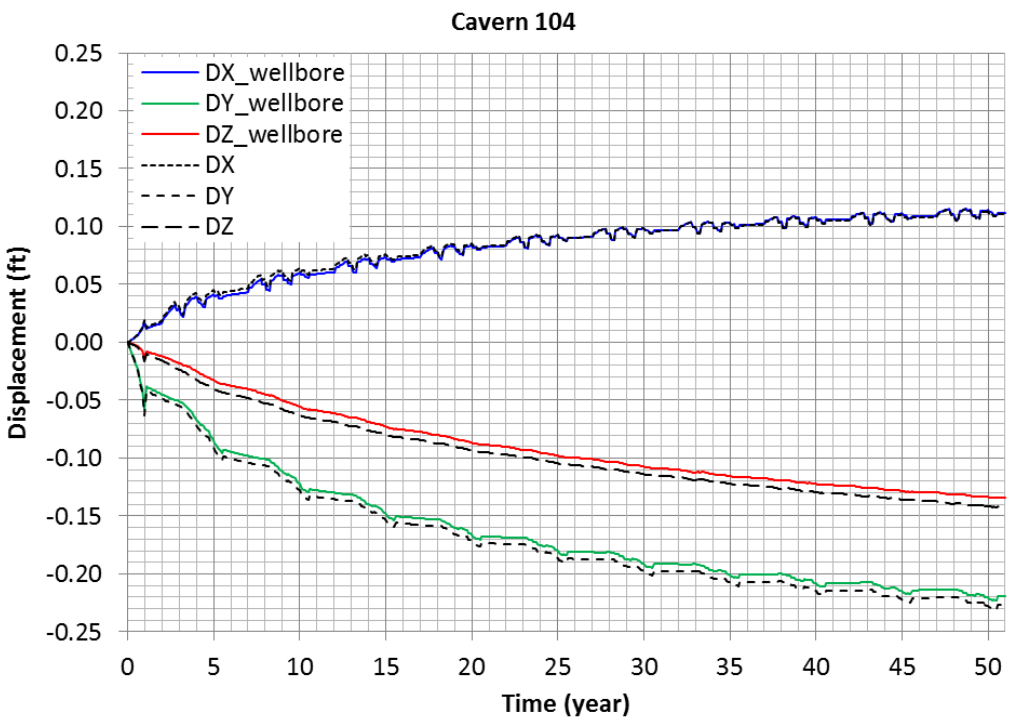

Figure 57: Predicted relative displacement between N_{CI} and N_{SI} in Figure 22 for BH104 as a function of time

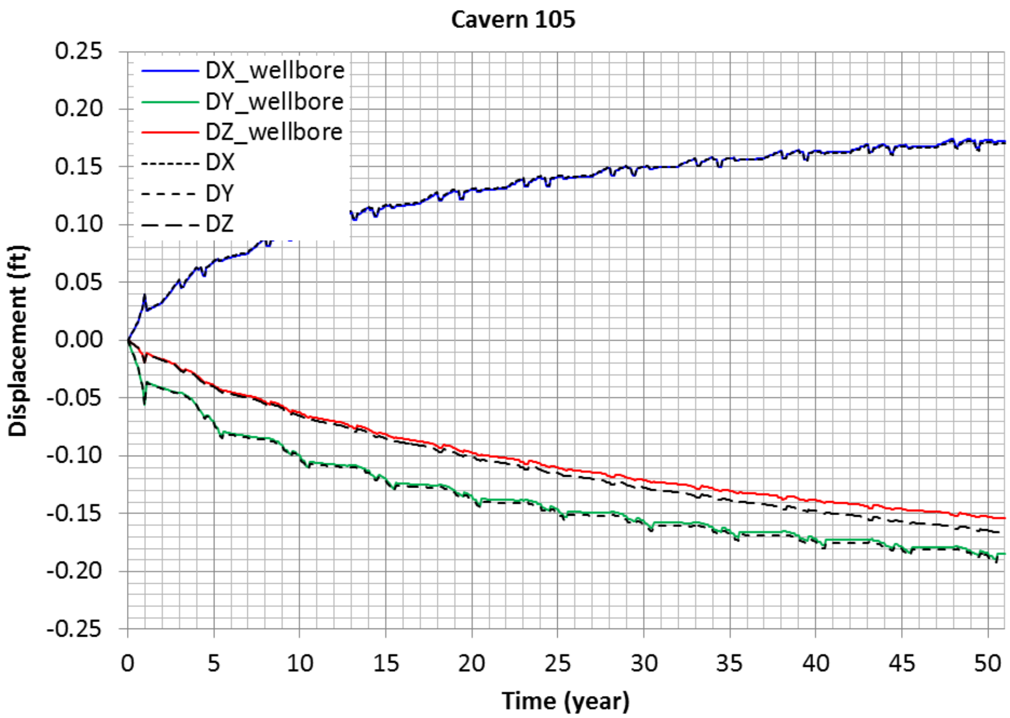

Figure 58: Predicted relative displacement between N_{CM} and N_{SM} in Figure 22 for BH105 as a function of time

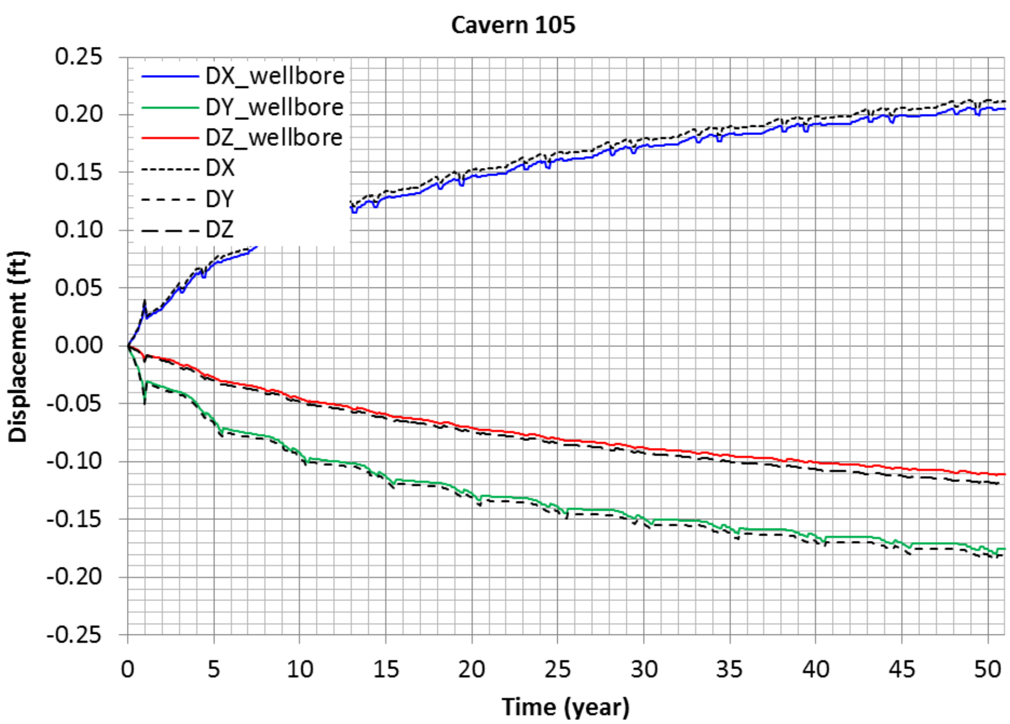

Figure 59: Predicted relative displacement between N_{CI} and N_{SI} in Figure 22 for BH105 as a function of time

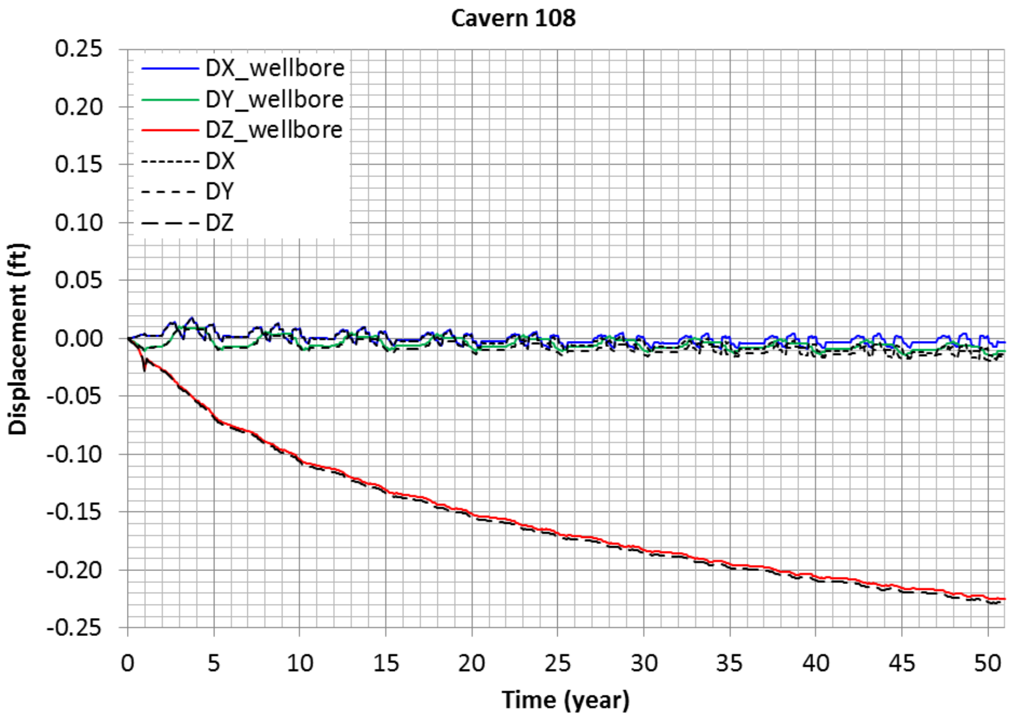

Figure 60: Predicted relative displacement between N_{CM} and N_{SM} in Figure 22 for BH108 as a function of time

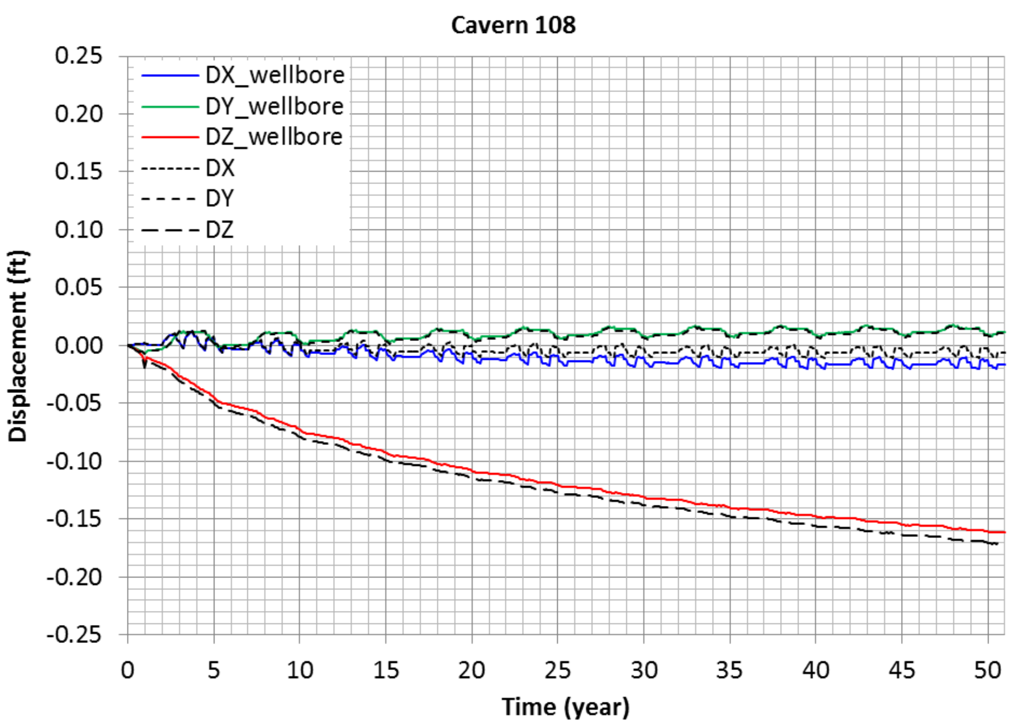

Figure 61: Predicted relative displacement between N_{CI} and N_{SI} in Figure 22 for BH108 as a function of time

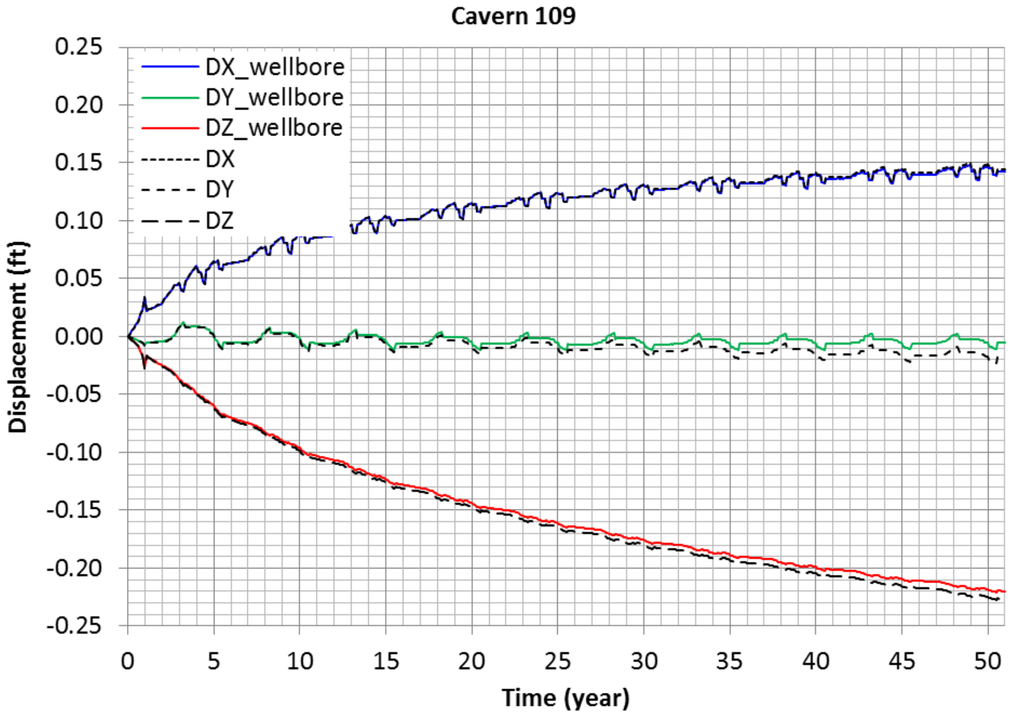

Figure 62: Predicted relative displacement between N_{CM} and N_{SM} in Figure 22 for BH109 as a function of time

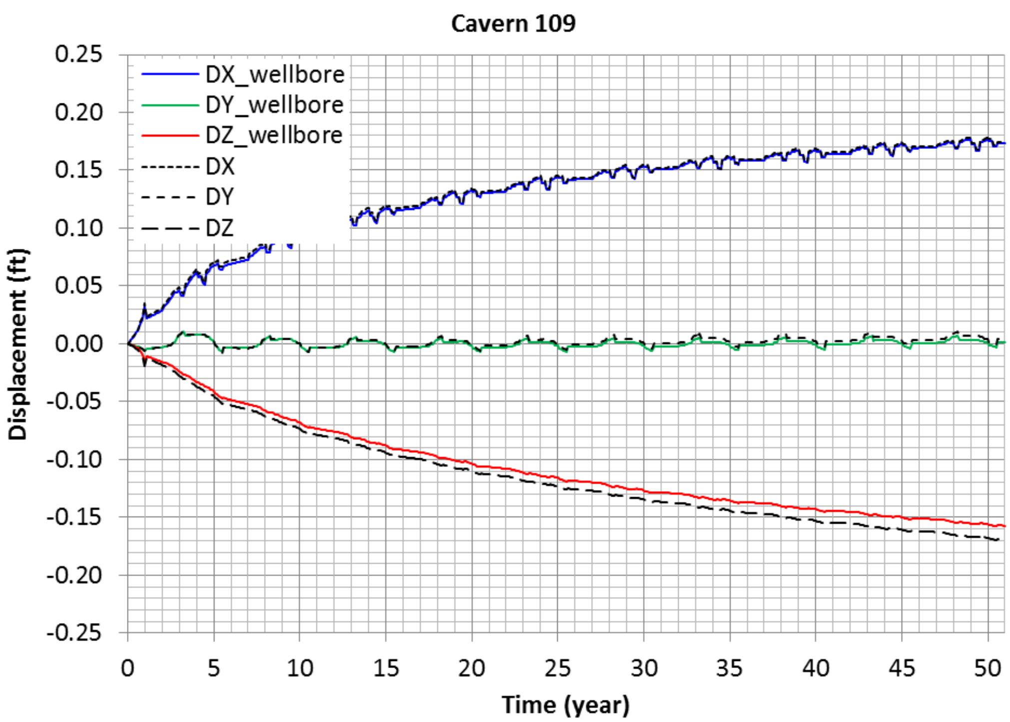

Figure 63: Predicted relative displacement between N_{CI} and N_{SI} in Figure 22 for BH109 as a function of time

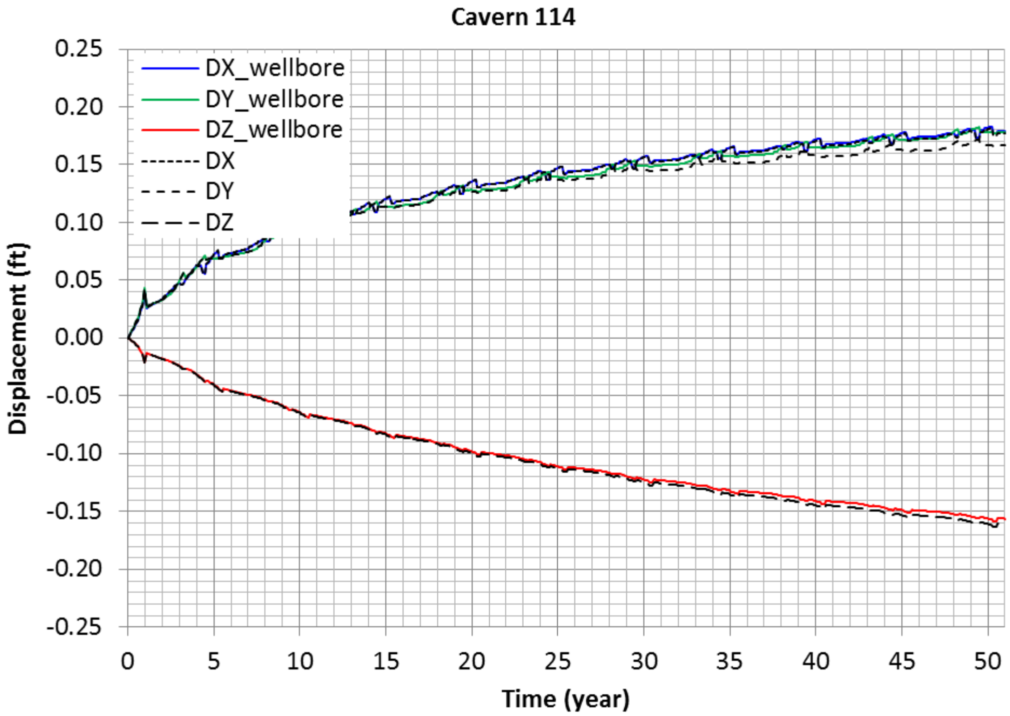

Figure 64: Predicted relative displacement between N_{CM} and N_{SM} in Figure 22 for BH114 as a function of time

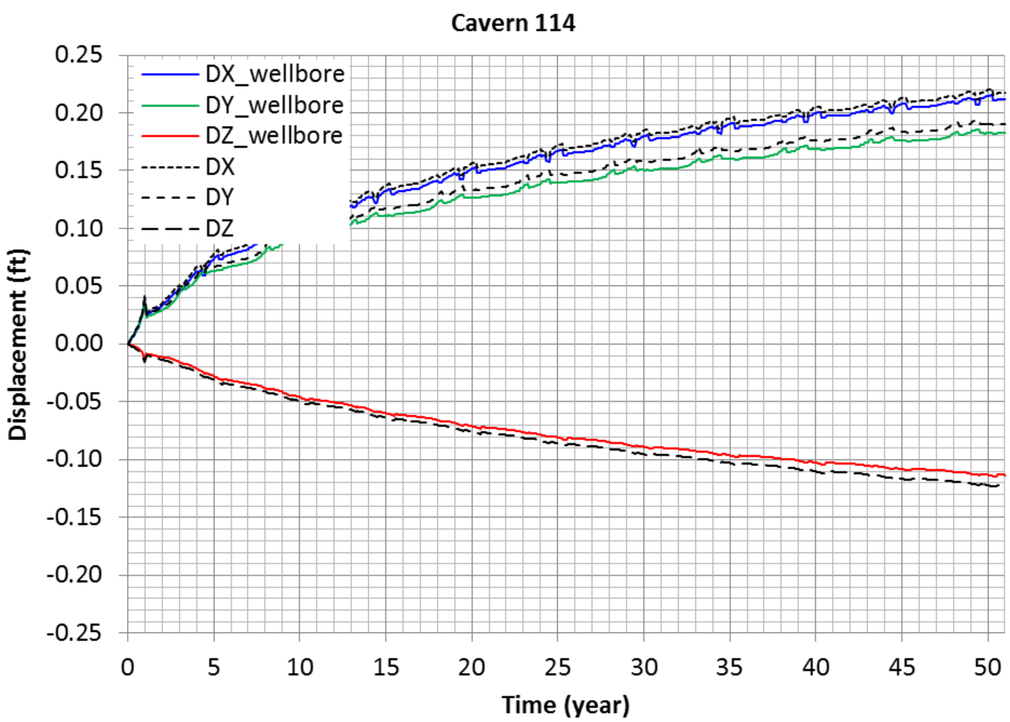

Figure 65: Predicted relative displacement between N_{CI} and N_{SI} in Figure 22 for BH114 as a function of time

6. SUMMARY AND CONCLUSIONS

Oil leaks were found at the well casings of Caverns 105 and 109 in BH SPR salt dome. According to the field observation, damage to the casings occurred at the depths of the interbed between the caprock and salt dome. A three-dimensional finite element model, which allows each cavern to be configured individually, was developed in the previous study [Park and Ehgartner, 2012]. Interface blocks, special purpose analysis tools, were implemented in the model for the caprock-salt interbed to investigate causes of wellbore damage. However, the wellbore casings were not included. This omission led to questions about the effect of those casings on the interaction between the salt and caprock. A global model, which contains the wellbore blocks, was constructed to investigate out how the wellbore affects the movement of the salt dome top.

The as-built wellbore consists of double steel casings and double cement annuli. The thicknesses of steel and cement are too small relative to the global model size. This size difference necessarily produces poor mesh quality. To improve the mesh quality, the blocks would have to be divided into smaller sizes of elements. Then, the number of elements in the mesh could be more than tens of millions. A mesh with such a large number of elements would consume an extraordinary amount of computer run time. To avoid this inefficiency, an equivalent wellbore, which consists of single steel casing and single cement annulus, was developed using the combined moment of inertia of the areas of casings and annuli from the two wellbores per a cavern. The equivalent single steel casing and single cement annulus become thicker than a single as-built well. This result in a mesh with fewer elements and acceptable quality conserves CPU time consumption with the same structural behavior as the combination of the two as-built wellbores.

The EQPS is calculated at every element of the equivalent steel casing in the cylindrical volume which encloses the intersection of each wellbore and the interbed between salt dome top and caprock bottom. The element where the maximum EQPS occurs among them and the value of EQPS are determined at each time step. Maximum EQPS in the equivalent steel casing is calculated as a function of time for each cavern well. BH109B is regarded as the baseline in this simulation. The EQPS at the leak date of BH109B is calculated to be about 0.79% which is used as the EQPS failure criterion. When this EQPS failure criterion is applied to BH105, the steel casing of Cavern 105 is predicted to fail at December 7, 2010 calendar time which is about one year different from the field observation (December 3, 2009). Considering the uncertainty due to geological assumptions and numerical simplifications, the EQPS failure criterion for the equivalent steel casing is considered to be reasonable.

The oil leak date for each well is determined by applying the 0.79% EQPS failure criterion to the predicted maximum EQPS history curve of each cavern wellbore. A well grading system for the remediation plan is developed using the predicted leak dates of each wellbore. The grades for only four cavern wells among fourteen caverns (BH102, BH103, BH108, and BH112) are different to the field observations. Taking into account uncertainty due to the assumptions in Section 2.1, the simulations results appear reasonable from a global perspective.

In conclusion, the causes of the damaged casing segments are a result of vertical and horizontal movements of the interbed between the caprock and salt dome. The salt top subsides because the volume of caverns below the salt top decrease with time due to salt creep closure, while the caprock subsides at a slower rate because the caprock is thick and stiff. This discrepancy yields deformation in a well. The deformed wellbore would fail at some time. An oil leak occurs when the wellbore fails.

For well remediation, a smaller size of steel casing could be inserted into the damaged steel casing all the way down to the depth of about 2065 ft from the surface. The horizontal deformation of the steel casing at the interbed will limit the OD of the inserted steel casing. From this study, a steel casing of OD less than 9-5/8” with flush-joint connection is recommended to use for remediation. A field engineer may use this recommendation as a reference.

To estimate out how the well impedes the movement of the salt dome top, a comparison of analyses results from models with and without the wellbore blocks is performed. The predicted total cavern volumetric closures from the two models are almost the same, i.e. the wellbore blocks do not affect the cavern volume closures. From comparisons of predicted relative displacements between the top and bottom of the interbed at the center of each cavern, the results show the stiff wellbore blocks do impede the movement of the salt top, however the amount of the impediment is very small. Therefore, a model omitting the wellbore blocks could be used for a more simplified simulation. The model without wellbores should reduce the effort needed to construct the mesh and save on computer run time. The result would be not much different from the model containing the wellbore blocks.

7. REFERENCES

Arguello J.G., J.E. Bean, C.M. Stone, and B.L. Ehgartner, 2009. *Geomechanical Analyses to Investigate Wellbore/Mine Interactions in the Potash Enclave of Southeastern New Mexico*, SAND2009-4795, Sandia National Laboratories, Albuquerque, NM.

Ballard, S. and B.L. Ehgartner, 2000, *CAVEMAN Version 3.0: System for SPR Cavern Pressure Analysis,* SAND2000-1751, Sandia National Laboratories, Albuquerque, NM 87185-0750.

Brannon, R.M., A.F. Fossum, and O.E. Strack, 2009. *KAYENTA Theory and User's Guide*, SAND2009-2282, Sandia National Laboratories, NM.

Butcher, B.M. 1997. *A Summary of the Sources of Input Parameter Values for the WIPP Final Porosity Surface Calculations*, SAND97-0796, Albuquerque, NM: Sandia National Laboratories.

DM, 2011a. *Well History Workover Report, Big Hill SPR Well 105-B, 04/29/2011through 04/22/2011*, New Orleans, LA 70123.

DM, 2011b. *Well History Workover Report, Big Hill SPR Well 109-B, 01/03/2011 through 04/28/2011*, New Orleans, LA 70123.

DM, 2013a. *Well History Workover Report, Big Hill SPR Well 114-A, 11/27/2012 through 01/22/2013*, New Orleans, LA 70123.

DM, 2013b. *Well History Workover Report, Big Hill SPR Cavern Well 114-B, 1/24/2013 through 4/15/2013*, New Orleans, LA 70123.

Ehgartner, B.L. and S. Bauer, 2004, *Large Scale Salt Deformation: Comments on Subsidence Using Thermal, Creep and Dissolution Modeling to Assess Volumetric Strain*, SAND2004-0095C, Sandia National Laboratories, Albuquerque, NM 87185.

Ehgartner, B.L., 2010, *Big Hill 105 Leak Analyses*, Memorandum from B. Ehgartner to R.E. Myers, DOE SPR PMO dated September 16, 2010. Sandia National Laboratories, Albuquerque, New Mexico.

Ehgartner, B.L., 2011, *Big Hill 109B Leak Estimate*, Memorandum from B. Ehgartner to R.E. Myers, DOE SPR PMO dated February 18, 2011. Sandia National Laboratories, Albuquerque, New Mexico.

Fossum, A. F. and Brannon, R. M., 2004. *The Sandia Geomodel Theory and User's Guide*, SAND2004-3226, Sandia National Laboratories, Albuquerque, NM.

Hoffman, E.L., 1992, *Investigation of Analysis Assumptions for SPR Calculations*, memo to J. K. Linn dated February 7, 1992, Sandia National Laboratories, Albuquerque, New Mexico.

Hull, J., 1988. *Thickness-displacement relationships for deformation zones*, J. Struct. Geol., 10, 431-435.

Krieg, R. D., 1984, *Reference Stratigraphy and Rock Properties for the Waste Isolation Pilot Plant (WIPP) Project*, SAND83-1908, Sandia National Laboratories, Albuquerque, NM 87185.

Krieg, R. D. and Krieg, D. B., 1977. Accuracies of Numerical Solution Methods for the Elastic-Perfectly Plastic Model, *ASME Journal of Pressure Vessel Technology*, vol. 99, pp. 510-515.

Magorian, T.R, and J.T. Neal, 1988. *Strategic Petroleum Reserve (SPR) Addition Geological Site Characterization Studies Big Hill Salt Dome, Texas*, SAND88-2267**,** Albuquerque, NM: Sandia National Laboratories.

Mohr, P.J., B.N. Taylor, and D.B. Newell, 2011, *The 2010 CODATA Recommended Values of the Fundamental Physical Constants (Web Version 6.0)*, Available at http://physics.nist.gov/constants, National Institute of Standards and Technology, Gaithersburg, MD 20899.

Munson, D.E., 1998. *Analysis of Multistage and Other Creep Data for Domal Salts*, SAND98-2276, Sandia National Laboratories, Albuquerque, NM.

Lord, A.S., 2011a. *March 2011 Big Hill Subsidence Analysis*, Memorandum to Gerard Berndsen dated July 13, 2011. Sandia National Laboratories, Albuquerque, NM.

Lord, A.S, 2011b. *RE: Additional BH sub data*, E-mail to Byoung Yoon Park dated June 17 2011, Sandia National Laboratories, Albuquerque, NM.

Park, B.Y., B.L. Ehgartner, M.Y. Lee, and S.R. Sobolik, 2005. *Three Dimensional Simulation for Big Hill Strategic Petroleum Reserve (SPR)*, SAND2005-3216, Sandia National Laboratories, Albuquerque, NM.

Park, B.Y. and B.L. Ehgartner, 2012, *Interface Modeling to Predict Well Casing Damage for Big Hill Strategic Petroleum Reserve*, SAND2012-1206, Sandia National Laboratories, Albuquerque, NM.

Rautman, C.A. and A.S. Lord, 2007. *Sonar Atlas of Caverns Comprising the U.S. Strategic Petroleum Reserve Volume 2: Big Hill Site, Texas*, SAND2007-6023, Sandia National Laboratories, Albuquerque, NM.

Sattler, A. R. and B. L. Ehgartner, 2011. *Big Hill Logging Results withe the Weatherford Multi-Arm Caliper*. Milestone Report FY11-1.1.4 & 1.1.6, Sandia National Laboratories, Albuquerque, NM USA.

Sattler, A. and B. Ehgartner, 2011. *Big Hill Logging Results with the Weatherford Multi Arm Caliper Tasks 1.1.4 Activity a1 and Task 1.1.6 activity a1*, Letter report to Robert E. Myer, DOE Project Manager, dated June 7, 2011.

Schreyer, H. L., Kulak, R. F., and Kramer, J. M., 1979. Accurate Numerical Solutions for Elastic-Plastic Models, *ASME Journal of Pressure Vessel Technology*, vol. 101, pp. 226-234, 1979.

Shipton, Z.K., A.M. Soden, J.D. Kirkpatrick, A.M. Bright, and R.J. Lunn, 2006. *How thick is a fault? Fault displacement-thickness scaling revisited. In Abercrombie*, R. (Eds) Earthquakes: Radiated Energy and the Physics of Faulting, pages pp. 193-198, AGU.

Taylor, L. M. and Flanagan, D. P., 1989. *PRONTO 3D A Three-Dimensional Transient Solid Dynamics Program*, SAND87-1912, Sandia National Laboratories, Albuquerque, NM, March 1989.

TMK-Ipsco, 2013. Ultra-FJ Brochure, Houston Sales Office, 10120 Houston Oaks Dr., Houston, TX 77064, www.tmk-ipsco.com.

Wawersik, W.R. and D.H Zeuch, 1984. *Creep and Creep Modeling of Three Domal Salts – A Comprehensive Update*, SAND84-0568, Sandia National Laboratories, Albuquerque, NM.

Weatherford, 2010. Multi-Sensor Caliper (MSC) Tool, Weatherford Brochure at http://www.weatherford.com/dn/WFT144393.

Wynn, K., 2012. *00-0000-2011-01-01-UPDATED MULTI ARM CALIPER SURVEYS.xlsx*. MS Excel 2010 file. Compilation of SPR Caliper Survey Data. DM Petroleum Operations. U.S. Strategic Petroleum Reserve. New Orleans, LA.

APPENDIX I: API CASING CHART (HALLIBURTON)

Security DBS Drill Bits

API Casing Chart

Roller Cone and Fixed Cutter Bits

API Casing Dimensions

CASING SIZE OD	CASING COUPLING OD	NOMINAL WEIGHT	INSIDE DIAMETER ID	API DRIFT ID	ROLLER CONE BIT SIZE OD		FIXED CUTTER BIT SIZE OD	
IN.	IN.	LBS/FT	IN.	IN.	IN.	DEC	IN.	DEC
4-1/2	5.000	9.50	4.090	3.965	3-7/8	3.875	3-7/8	3.875
4.500	5.000	10.50	4.052	3.927	3-7/8	3.875	3-7/8	3.875
	5.000	11.60	4.000	3.875	3-7/8	3.875	3-7/8	3.875
	5.000	13.50	3.920	3.795	3-3/4	3.750	3-3/4	3.750
5	5.563	11.50	4.560	4.435	3-7/8	3.875	3-7/8	3.875
5.000	5.563	13.00	4.494	4.369	3-7/8	3.875	3-7/8	3.875
	5.563	15.00	4.408	4.283	3-7/8	3.875	3-7/8	3.875
	5.563	18.00	4.276	4.151	3-7/8	3.875	3-7/8	3.875
5-1/2	6.050	14.00	5.012	4.887	4-3/4	4.750	4-3/4	4.750
5.500	6.050	15.50	4.950	4.825	4-3/4	4.750	4-3/4	4.750
	6.050	17.00	4.892	4.767	4-3/4	4.750	4-3/4	4.750
	6.050	20.00	4.778	4.653	3-7/8	3.875	4-1/2	4.500
	6.050	23.00	4.670	4.545	3-7/8	3.875	4-1/2	4.500
6-5/8	7.390	20.00	6.049	5.924	5-7/8	5.875	5-7/8	5.875
6.625	7.390	24.00	5.921	5.796	4-3/4	4.750	4-3/4	4.750
	7.390	28.00	5.791	5.666	4-3/4	4.750	4-3/4	4.750
	7.390	32.00	5.675	5.550	4-3/4	4.750	4-3/4	4.750
7	7.656	17.00	6.538	6.413	6-1/4	6.250	6-1/4	6.250
7.000	7.656	20.00	6.456	6.331	6-1/4	6.250	6-1/4	6.250
	7.656	23.00	6.366	6.241	6-1/8	6.125	6-1/8	6.125
	7.656	26.00	6.276	6.151	6-1/8	6.125	6-1/8	6.125
	7.656	29.00	6.184	6.059	6	6.000	6	6.000
	7.656	32.00	6.094	5.969	5-7/8	5.875	5-7/8	5.875
	7.656	35.00	6.004	5.879	5-7/8	5.875	5-7/8	5.875
	7.656	38.00	5.920	5.795	4-3/4	4.750	4-3/4	4.750
7-5/8	8.500	20.00	7.125	7.000	6-3/4	6.750	6-3/4	6.750
7.625	8.500	24.00	7.025	6.900	6-3/4	6.750	6-3/4	6.750
	8.500	26.40	6.969	6.844	6-3/4	6.750	6-3/4	6.750
	8.500	29.70	6.875	6.750	6-3/4	6.750	6-3/4	6.750
	8.500	33.70	6.765	6.640	6-1/2	6.500	6-1/2	6.500
	8.500	39.00	6.625	6.500	6-1/2	6.500	6-1/2	6.500
8-5/8	9.625	24.00	8.097	7.972	7-7/8	7.875	7-7/8	7.875
8.625	9.625	28.00	8.017	7.892	7-7/8	7.875	7-7/8	7.875
	9.625	32.00	7.921	7.796	6-3/4	6.750	6-3/4	6.750
	9.625	36.00	7.825	7.700	6-3/4	6.750	6-3/4	6.750
	9.625	40.00	7.725	7.600	6-3/4	6.750	6-3/4	6.750
	9.625	44.00	7.625	7.500	6-3/4	6.750	6-3/4	6.750
	9.625	49.00	7.511	7.386	6-3/4	6.750	6-3/4	6.750

NOTE: Above information for API casing data, refer to Toolpusher's Manual or specific manufacturer's specifications.
For metric equivalents (millimeters), multiply the inches by 25.4.

HALLIBURTON

API Casing Dimensions (continued)

CASING SIZE OD IN.	CASING COUPLING OD IN.	NOMINAL WEIGHT LBS/FT	INSIDE DIAMETER ID IN.	API DRIFT ID IN.	ROLLER CONE BIT SIZE OD IN.	ROLLER CONE BIT SIZE OD DEC	FIXED CUTTER BIT SIZE OD IN.	FIXED CUTTER BIT SIZE OD DEC
9-5/8	10.625	29.30	9.063	8.907	8-3/4	8.750	8-3/44	8.750
9.625	10.625	32.30	9.001	8.845	8-3/4	8.750	8-3/4	8.750
	10.625	36.00	8.921	8.765	8-3/4	8.750	8-3/4	8.750
	10.625	40.00	8.835	8.679	8-1/2	8.500	8-1/2	8.500
	10.625	43.50	8.755	8.599	8-1/2	8.500	8-1/2	8.500
	10.625	47.00	8.681	8.525	8-1/2	8.500	8-1/2	8.500
	10.625	53.50	8.535	8.379	8-3/8	8.375	8-3/8	8.375
10-3/4	11.750	32.75	10.192	10.036	9-7/8	9.875	9-7/8	9.875
10.750	11.750	40.50	10.050	9.984	9-7/8	9.875	9-7/8	9.875
	11.750	45.50	9.950	9.794	9-1/2	9.500	9-1/2	9.500
	11.750	51.00	9.850	9.694	9-1/2	9.500	9-1/2	9.500
	11.750	55.50	9.760	9.604	9-1/2	9.500	9-1/2	9.500
	11.750	60.70	9.660	9.504	9-1/2	9.500	9-1/2	9.500
	11.750	65.70	9.560	9.404	8-3/4	8.750	8-3/4	8.750
11-3/4	12.750	42.00	11.084	10.928	10-5/8	10.625	10-5/8	10.625
11.750	12.750	47.00	11.000	10.844	10-5/8	10.625	10-5/8	10.625
	12.750	54.00	10.880	10.724	10-5/8	10.625	10-5/8	10.625
	12.750	60.00	10.772	10.616	9-7/8	9.875	9-7/8	9.875
13-3/8	14.375	48.00	12.715	12.559	12-1/4	12.250	12-1/4	12.250
13.375	14.375	54.50	12.615	12.459	12-1/4	12.250	12 1/4	12.250
	14.375	61.00	12.515	12.359	12-1/4	12.250	12-1/4	12.250
	14.375	68.00	12.415	12.259	12-1/4	12.250	12-1/4	12.250
	14.375	72.00	12.347	12.191	11	11.000	10-5/8	10.625
16	17.000	65.00	15.250	15.062	14-3/4	14.750	14-3/4	14.750
16.000	17.000	75.00	15.124	14.936	14-3/4	14.750	14-3/4	14.750
	17.000	84.00	15.010	14.822	14-3/4	14.750	14-3/4	14.750
18-5/8	20.000	87.50	17.755	17.567	17-1/2	17.500	17-1/2	17.500
18.625	-	-	-	-	-	-	-	-
20	21.000	94.00	19.124	18.936	17-1/2	17.500	17-1/2	17.500
20.000	21.000	106.50	19.000	18.812	17-1/2	17.500	17-1/2	17.500
	21.000	133.00	18.730	18.542	17-1/2	17.500	17-1/2	17.500
	21.000	169.00	18.376	18.188	17-1/2	17.500	17-1/2	17.500

NOTE: Above information for API casing data, refer to Toolpusher's Manual or specific manufacturer's specifications.
For metric equivalents (millimeters), multiply the inches by 25.4.

www.halliburton.com

H03038 09/05

Sales of Halliburton products and services will be in accord solely with the terms and conditions contained in the contract between Halliburton and the customer that is applicable to the sale.

HALLIBURTON

Drilling and Formation Evaluation

APPENDIX II: PREDICTED DISPLACEMENTS

Appendix II-1: Displacements at N_{CI} and N_{SI}

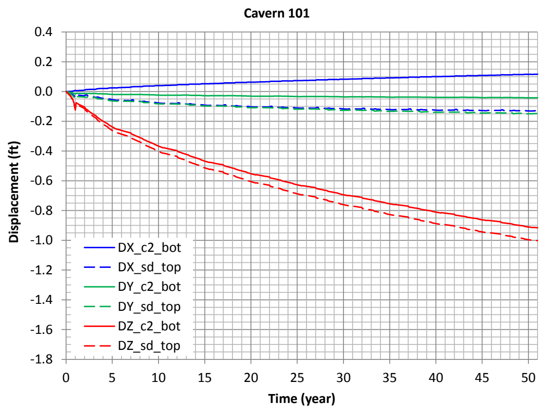

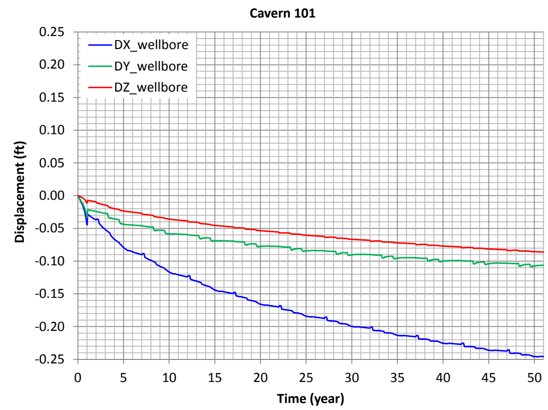

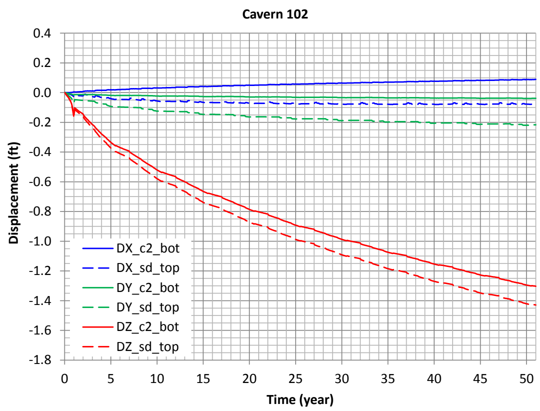

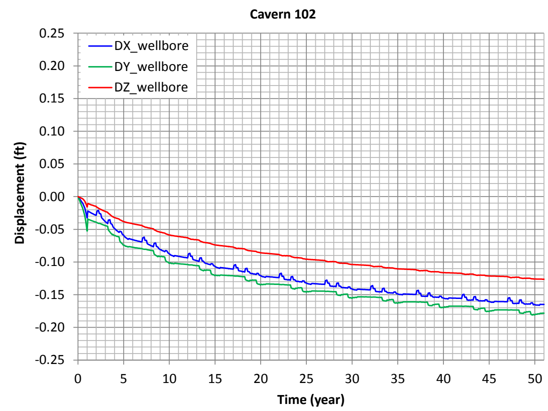

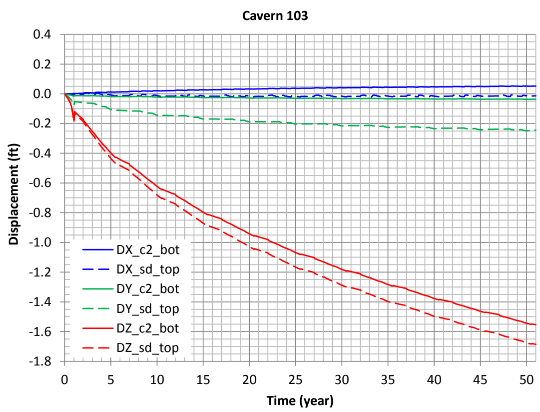

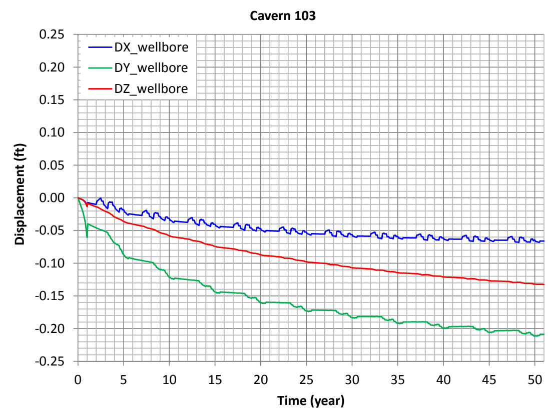

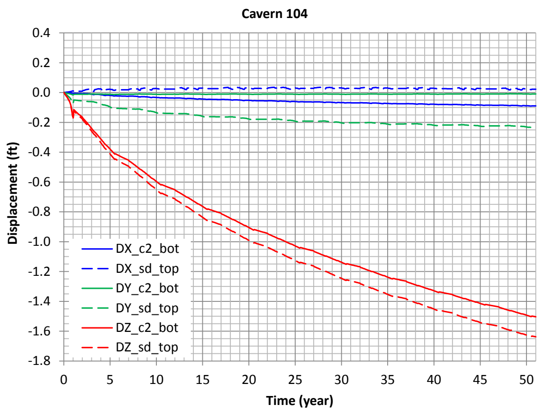
Cavern 104
Displacement (ft)
Time (year)
DX_c2_bot
DX_sd_top
DY_c2_bot
DY_sd_top
DZ_c2_bot
DZ_sd_top

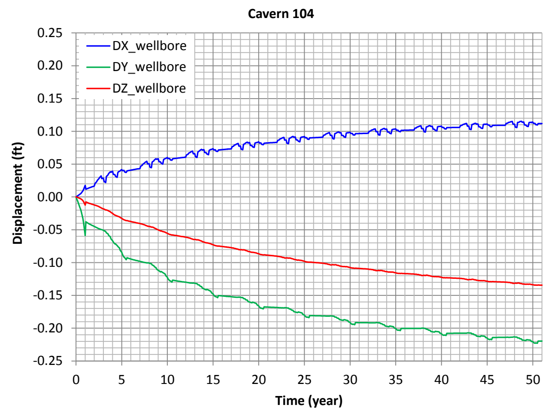
Cavern 104
Displacement (ft)
Time (year)
DX_wellbore
DY_wellbore
DZ_wellbore

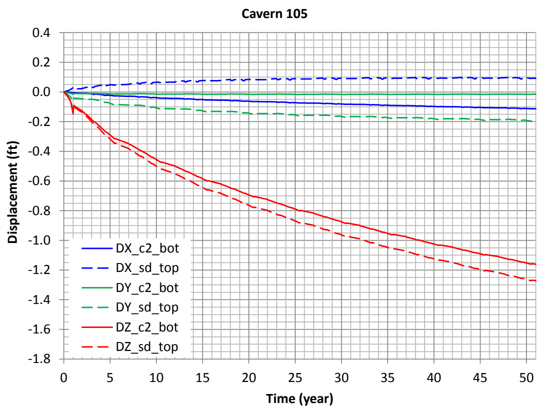
Cavern 105
Displacement (ft)
Time (year)
DX_c2_bot
DX_sd_top
DY_c2_bot
DY_sd_top
DZ_c2_bot
DZ_sd_top

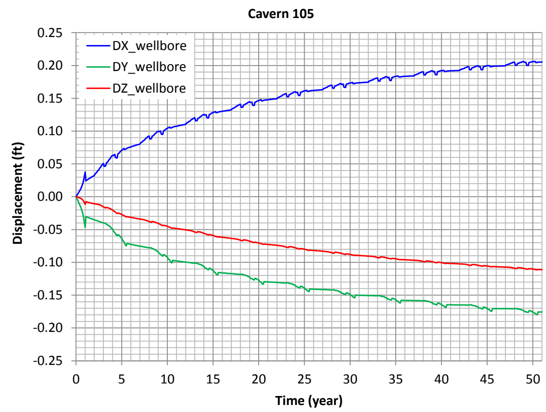
Cavern 105
Displacement (ft)
Time (year)
DX_wellbore
DY_wellbore
DZ_wellbore

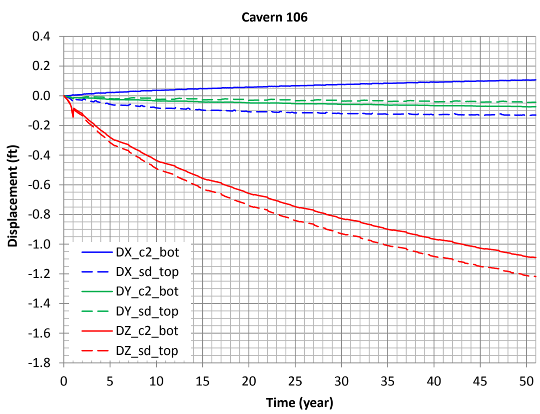
Cavern 106
Displacement (ft)
Time (year)
DX_c2_bot
DX_sd_top
DY_c2_bot
DY_sd_top
DZ_c2_bot
DZ_sd_top

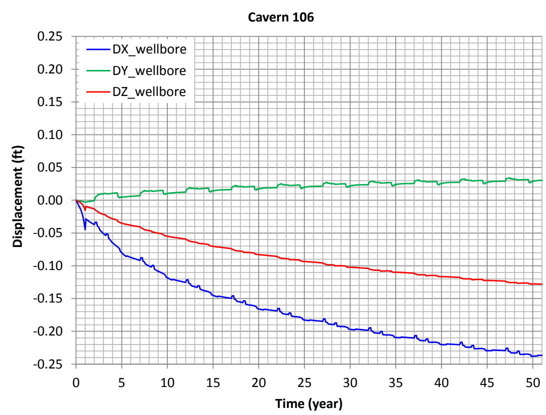
Cavern 106
Displacement (ft)
Time (year)
DX_wellbore
DY_wellbore
DZ_wellbore

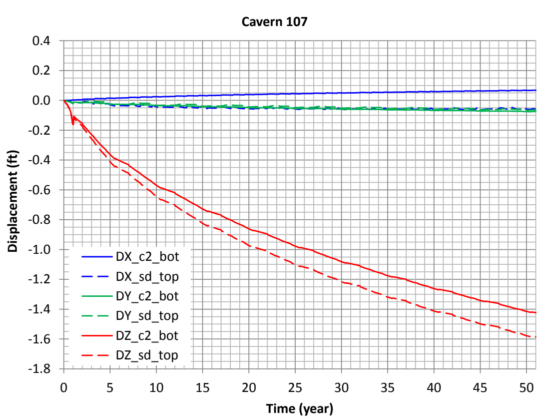
Cavern 107
Displacement (ft)
Time (year)
DX_c2_bot
DX_sd_top
DY_c2_bot
DY_sd_top
DZ_c2_bot
DZ_sd_top

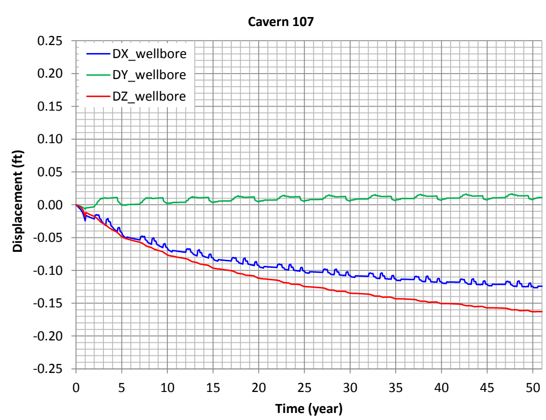
Cavern 107
Displacement (ft)
Time (year)
DX_wellbore
DY_wellbore
DZ_wellbore

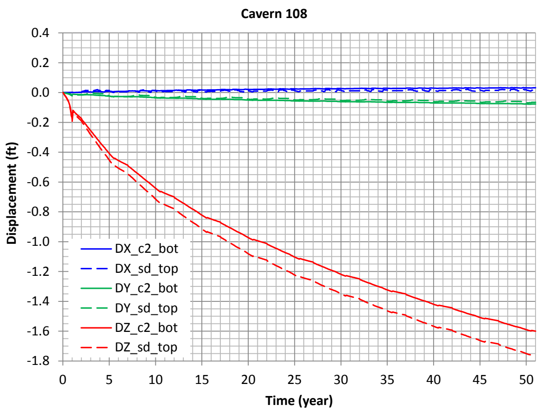
Cavern 108
Displacement (ft)
Time (year)
DX_c2_bot
DX_sd_top
DY_c2_bot
DY_sd_top
DZ_c2_bot
DZ_sd_top

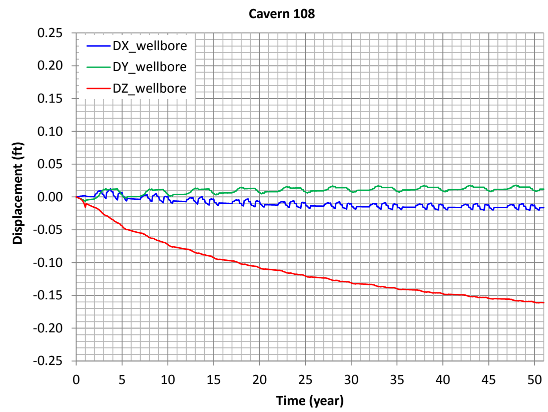
Cavern 108
Displacement (ft)
Time (year)
DX_wellbore
DY_wellbore
DZ_wellbore

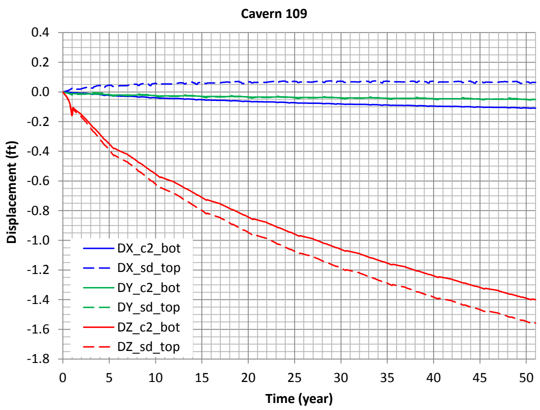
Cavern 109
Displacement (ft)
Time (year)
DX_c2_bot
DX_sd_top
DY_c2_bot
DY_sd_top
DZ_c2_bot
DZ_sd_top

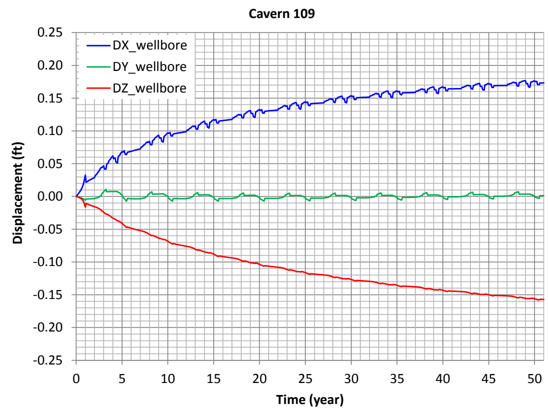
Cavern 109
Displacement (ft)
Time (year)
DX_wellbore
DY_wellbore
DZ_wellbore

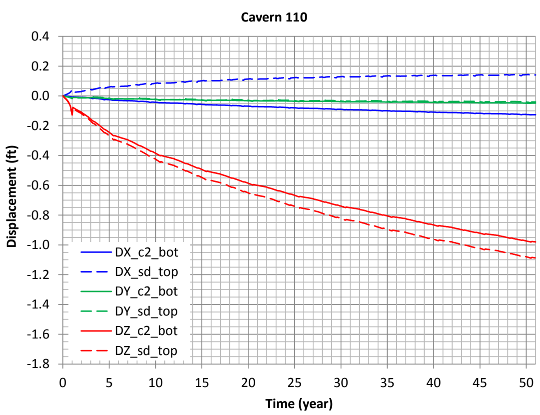
Cavern 110
Displacement (ft)
Time (year)
DX_c2_bot
DX_sd_top
DY_c2_bot
DY_sd_top
DZ_c2_bot
DZ_sd_top

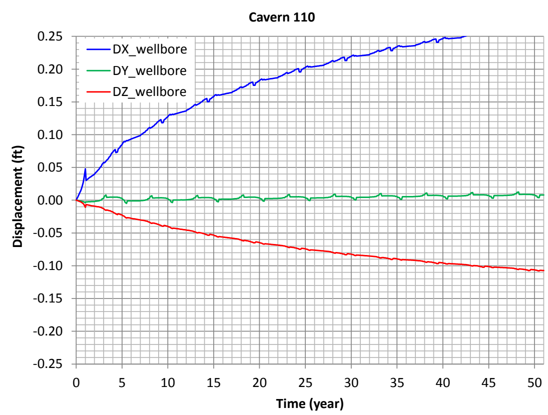
Cavern 110
Displacement (ft)
Time (year)
DX_wellbore
DY_wellbore
DZ_wellbore

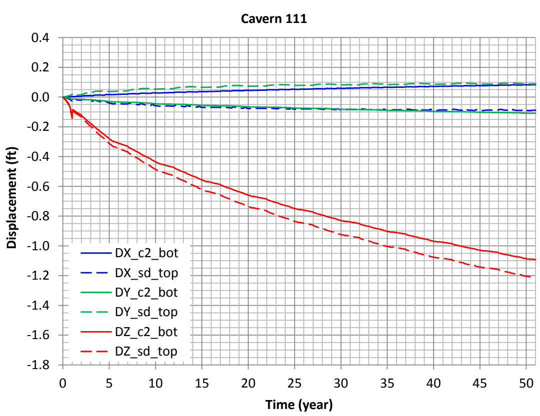
Cavern 111
Displacement (ft)
Time (year)
DX_c2_bot
DX_sd_top
DY_c2_bot
DY_sd_top
DZ_c2_bot
DZ_sd_top

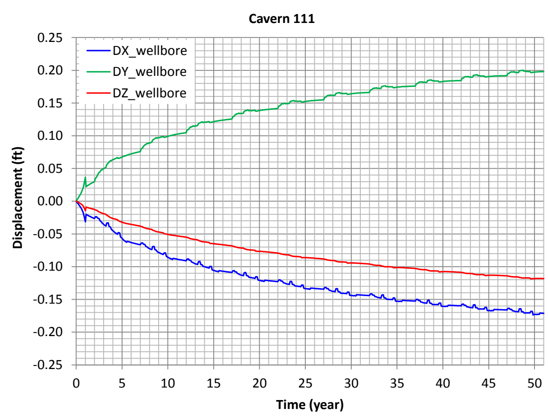
Cavern 111
Displacement (ft)
Time (year)
DX_wellbore
DY_wellbore
DZ_wellbore

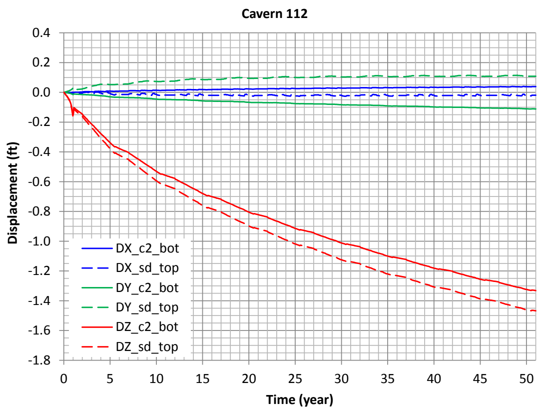
Cavern 112
Displacement (ft)
Time (year)
0.4
0.2
0.0
-0.2
-0.4
-0.6
-0.8
-1.0
-1.2
-1.4
-1.6
-1.8
0
5
10
15
20
25
30
35
40
45
50
DX_c2_bot
DX_sd_top
DY_c2_bot
DY_sd_top
DZ_c2_bot
DZ_sd_top

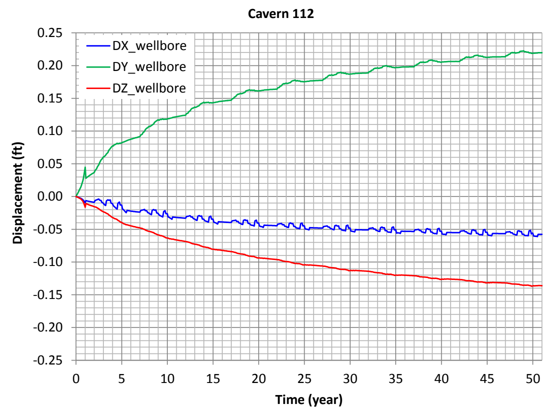
Cavern 112
Displacement (ft)
Time (year)
0.25
0.20
0.15
0.10
0.05
0.00
-0.05
-0.10
-0.15
-0.20
-0.25
0
5
10
15
20
25
30
35
40
45
50
DX_wellbore
DY_wellbore
DZ_wellbore

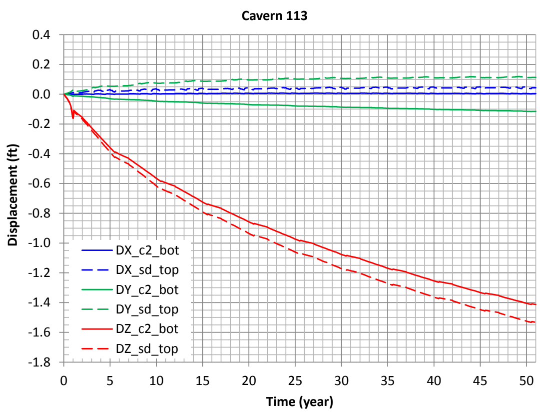
Cavern 113
Displacement (ft)
Time (year)
0.4
0.2
0.0
-0.2
-0.4
-0.6
-0.8
-1.0
-1.2
-1.4
-1.6
-1.8
0
5
10
15
20
25
30
35
40
45
50
DX_c2_bot
DX_sd_top
DY_c2_bot
DY_sd_top
DZ_c2_bot
DZ_sd_top

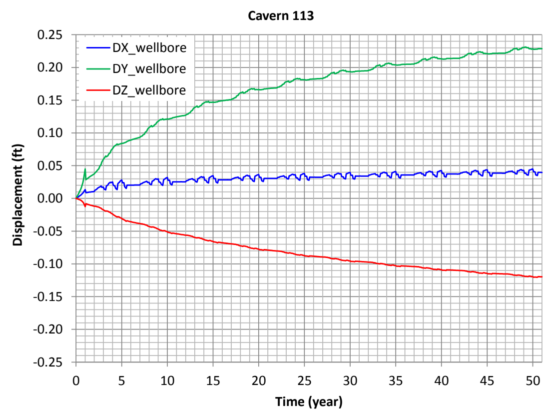
Cavern 113
Displacement (ft)
Time (year)
0.25
0.20
0.15
0.10
0.05
0.00
-0.05
-0.10
-0.15
-0.20
-0.25
0
5
10
15
20
25
30
35
40
45
50
DX_wellbore
DY_wellbore
DZ_wellbore

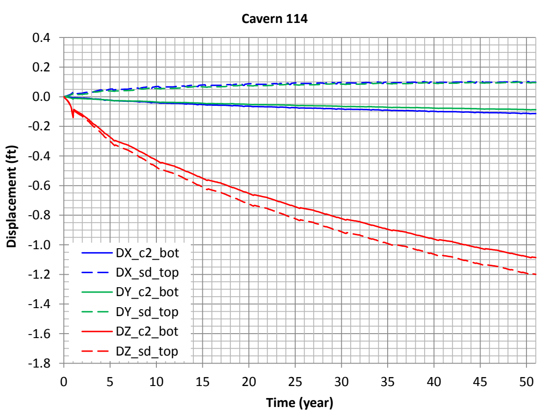
Cavern 114
Displacement (ft)
Time (year)
0.4
0.2
0.0
-0.2
-0.4
-0.6
-0.8
-1.0
-1.2
-1.4
-1.6
-1.8
0
5
10
15
20
25
30
35
40
45
50
DX_c2_bot
DX_sd_top
DY_c2_bot
DY_sd_top
DZ_c2_bot
DZ_sd_top

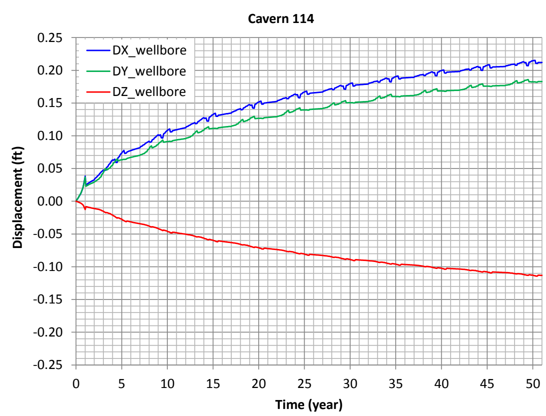
Cavern 114
Displacement (ft)
Time (year)
0.25
0.20
0.15
0.10
0.05
0.00
-0.05
-0.10
-0.15
-0.20
-0.25
0
5
10
15
20
25
30
35
40
45
50
DX_wellbore
DY_wellbore
DZ_wellbore

Appendix II-2: Displacements at N_{CM} and N_{SM}

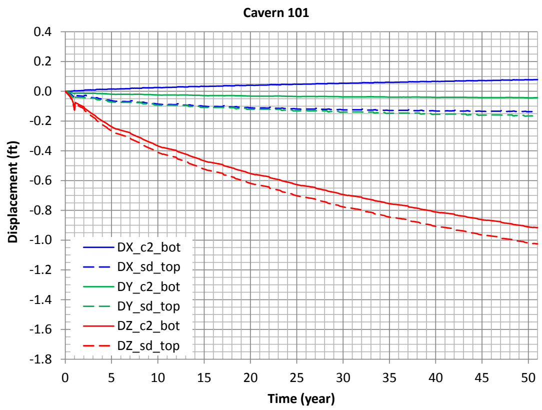

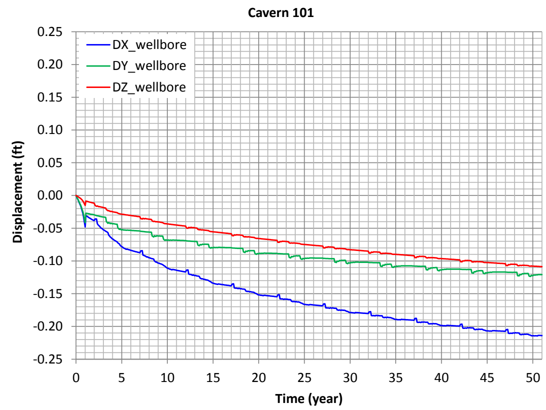

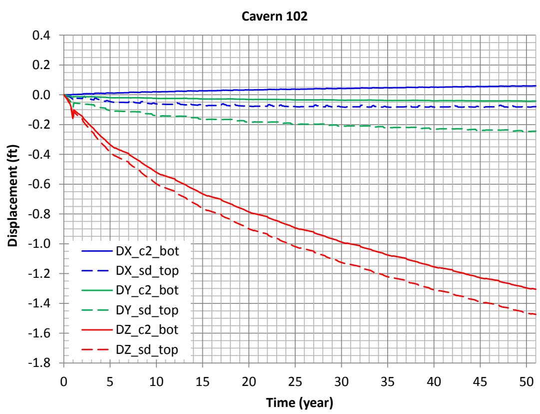

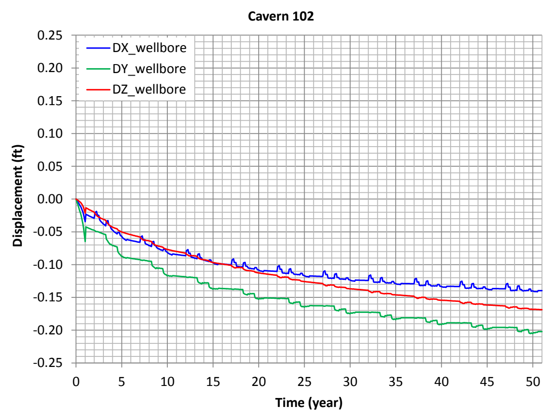

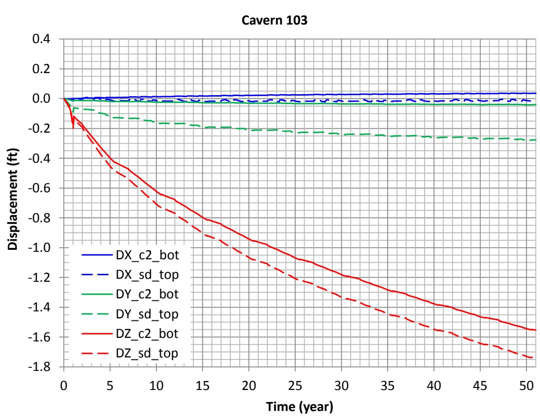

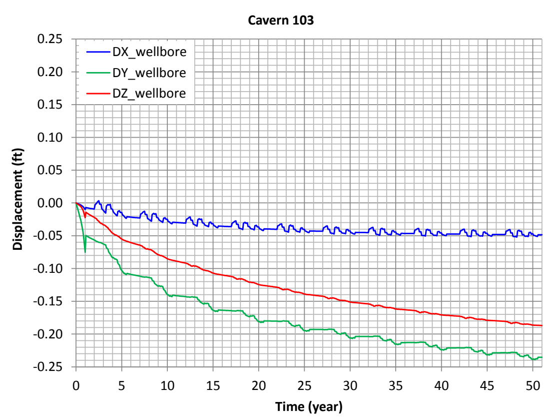

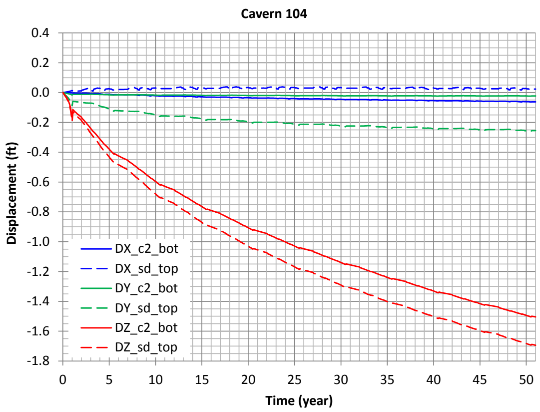
Cavern 104
Displacement (ft)
Time (year)
DX_c2_bot
DX_sd_top
DY_c2_bot
DY_sd_top
DZ_c2_bot
DZ_sd_top

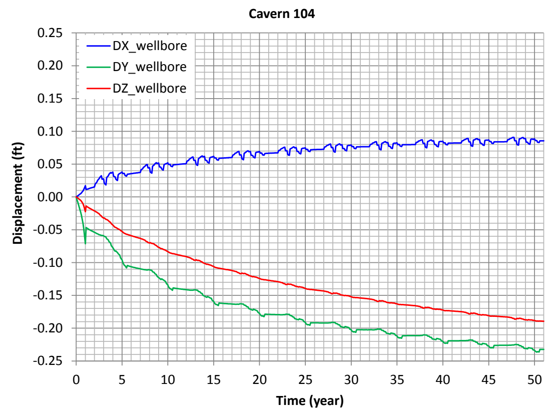
Cavern 104
Displacement (ft)
Time (year)
DX_wellbore
DY_wellbore
DZ_wellbore

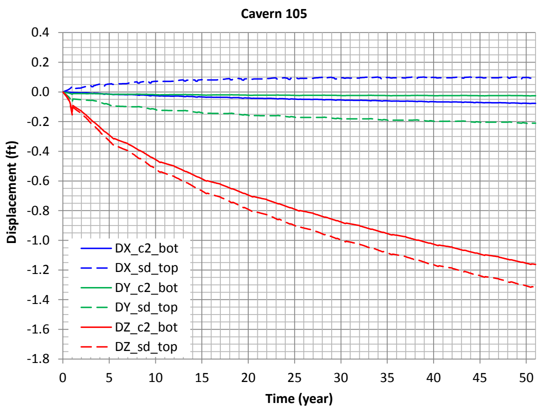
Cavern 105
Displacement (ft)
Time (year)
DX_c2_bot
DX_sd_top
DY_c2_bot
DY_sd_top
DZ_c2_bot
DZ_sd_top

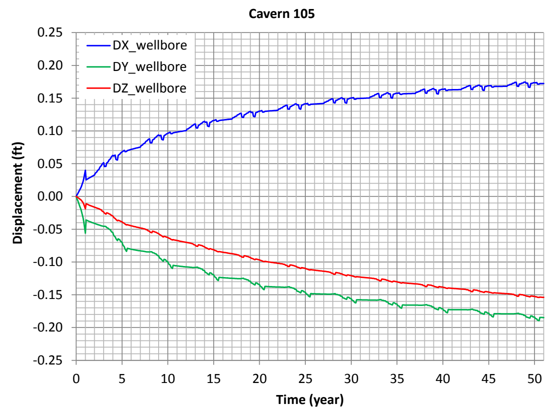
Cavern 105
Displacement (ft)
Time (year)
DX_wellbore
DY_wellbore
DZ_wellbore

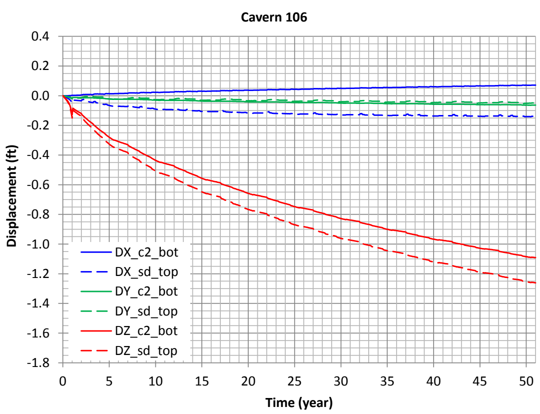
Cavern 106
Displacement (ft)
Time (year)
DX_c2_bot
DX_sd_top
DY_c2_bot
DY_sd_top
DZ_c2_bot
DZ_sd_top

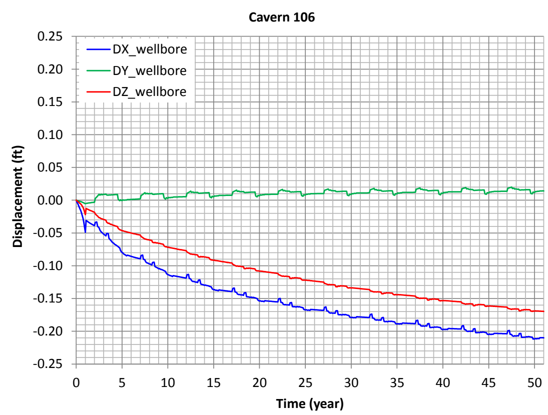
Cavern 106
Displacement (ft)
Time (year)
DX_wellbore
DY_wellbore
DZ_wellbore

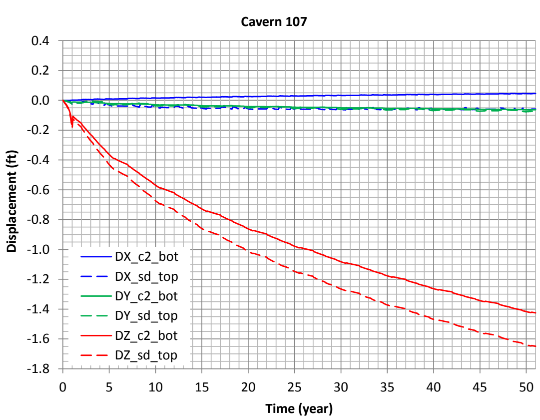
Cavern 107
Displacement (ft)
Time (year)
DX_c2_bot
DX_sd_top
DY_c2_bot
DY_sd_top
DZ_c2_bot
DZ_sd_top

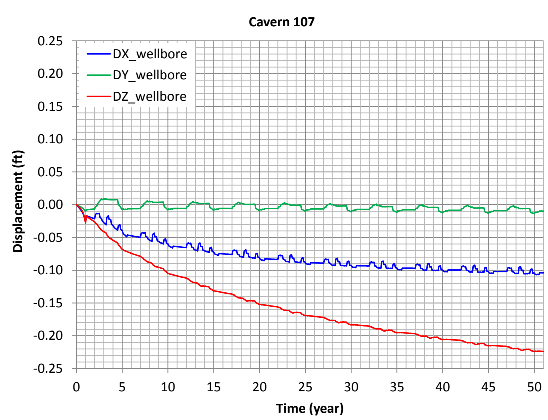
Cavern 107
Displacement (ft)
Time (year)
DX_wellbore
DY_wellbore
DZ_wellbore

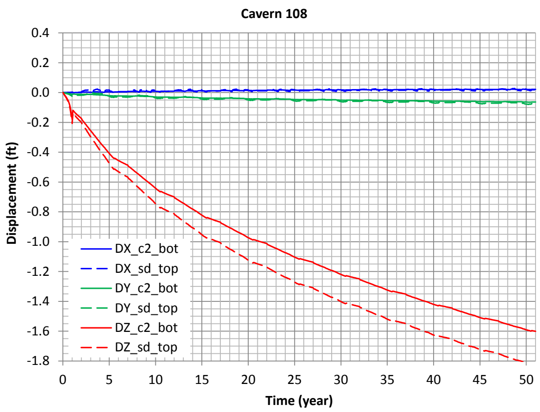

Cavern 108
Displacement (ft)
Time (year)
DX_c2_bot
DX_sd_top
DY_c2_bot
DY_sd_top
DZ_c2_bot
DZ_sd_top

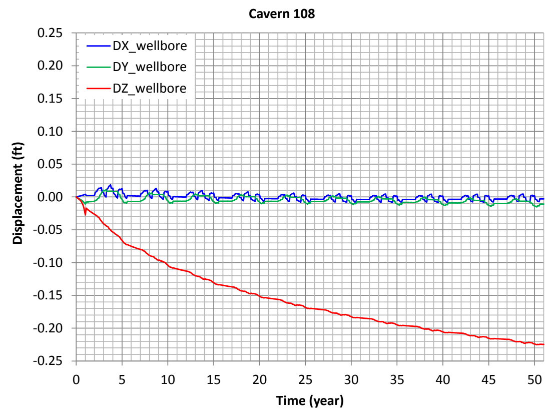

Cavern 108
Displacement (ft)
Time (year)
DX_wellbore
DY_wellbore
DZ_wellbore

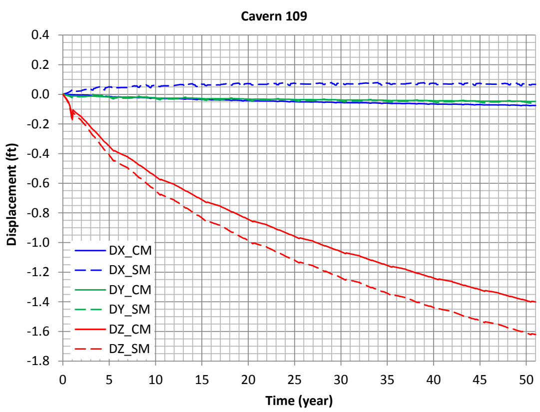

Cavern 109
Displacement (ft)
Time (year)
DX_CM
DX_SM
DY_CM
DY_SM
DZ_CM
DZ_SM

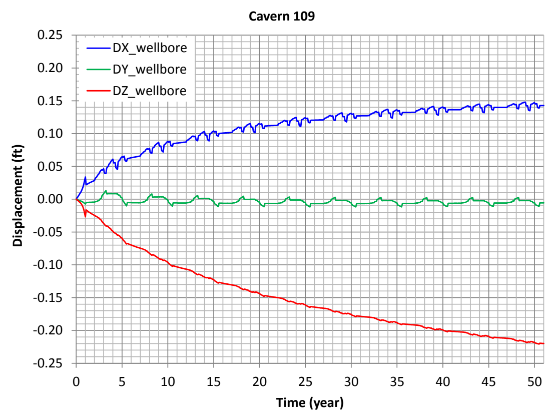

Cavern 109
Displacement (ft)
Time (year)
DX_wellbore
DY_wellbore
DZ_wellbore

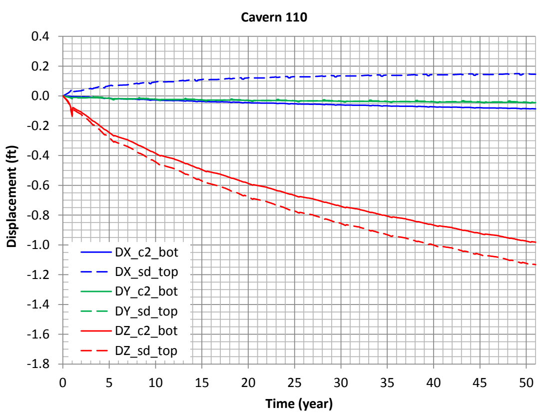

Cavern 110
Displacement (ft)
Time (year)
DX_c2_bot
DX_sd_top
DY_c2_bot
DY_sd_top
DZ_c2_bot
DZ_sd_top

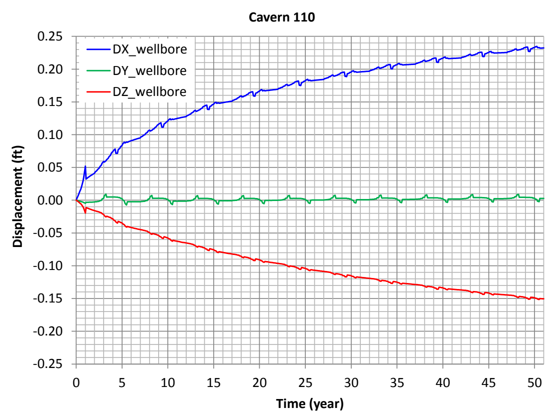

Cavern 110
Displacement (ft)
Time (year)
DX_wellbore
DY_wellbore
DZ_wellbore

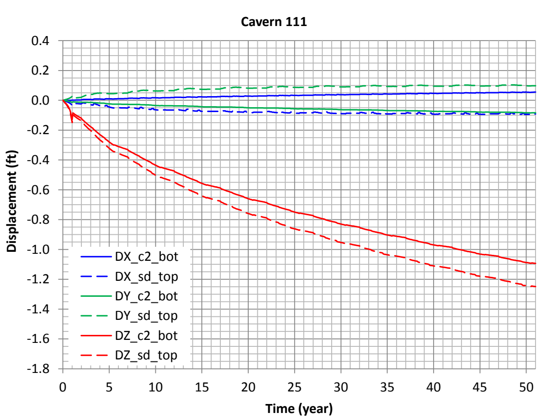

Cavern 111
Displacement (ft)
Time (year)
DX_c2_bot
DX_sd_top
DY_c2_bot
DY_sd_top
DZ_c2_bot
DZ_sd_top

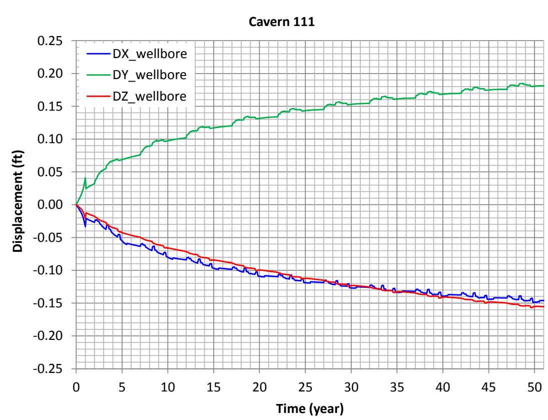

Cavern 111
Displacement (ft)
Time (year)
DX_wellbore
DY_wellbore
DZ_wellbore

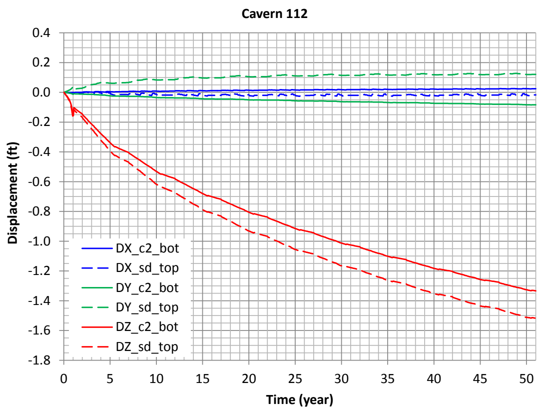
Cavern 112
Displacement (ft)
0.4
0.2
0.0
-0.2
-0.4
-0.6
-0.8
-1.0
-1.2
-1.4
-1.6
-1.8
0 5 10 15 20 25 30 35 40 45 50
Time (year)
DX_c2_bot
DX_sd_top
DY_c2_bot
DY_sd_top
DZ_c2_bot
DZ_sd_top

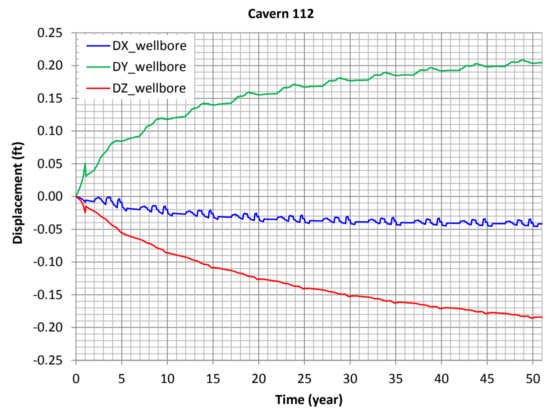
Cavern 112
Displacement (ft)
0.25
0.20
0.15
0.10
0.05
0.00
-0.05
-0.10
-0.15
-0.20
-0.25
0 5 10 15 20 25 30 35 40 45 50
Time (year)
DX_wellbore
DY_wellbore
DZ_wellbore

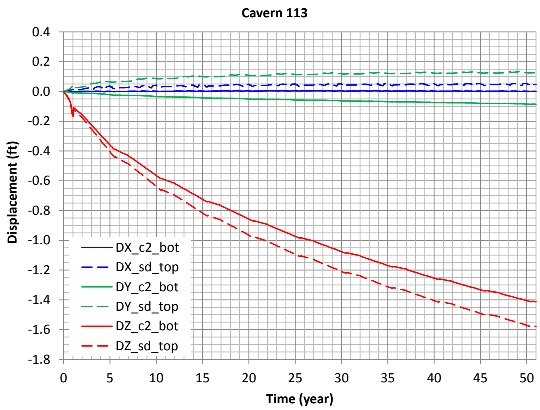
Cavern 113
Displacement (ft)
0.4
0.2
0.0
-0.2
-0.4
-0.6
-0.8
-1.0
-1.2
-1.4
-1.6
-1.8
0 5 10 15 20 25 30 35 40 45 50
Time (year)
DX_c2_bot
DX_sd_top
DY_c2_bot
DY_sd_top
DZ_c2_bot
DZ_sd_top

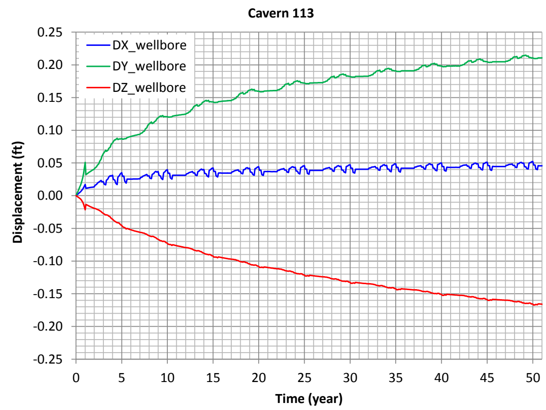
Cavern 113
Displacement (ft)
0.25
0.20
0.15
0.10
0.05
0.00
-0.05
-0.10
-0.15
-0.20
-0.25
0 5 10 15 20 25 30 35 40 45 50
Time (year)
DX_wellbore
DY_wellbore
DZ_wellbore

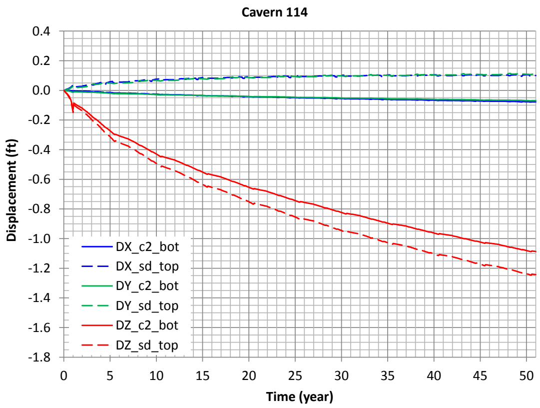
Cavern 114
Displacement (ft)
0.4
0.2
0.0
-0.2
-0.4
-0.6
-0.8
-1.0
-1.2
-1.4
-1.6
-1.8
0 5 10 15 20 25 30 35 40 45 50
Time (year)
DX_c2_bot
DX_sd_top
DY_c2_bot
DY_sd_top
DZ_c2_bot
DZ_sd_top

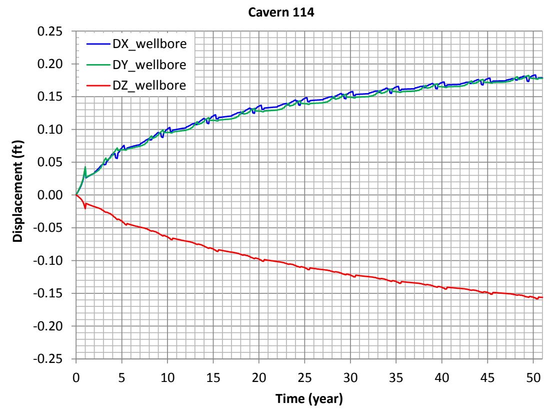
Cavern 114
Displacement (ft)
0.25
0.20
0.15
0.10
0.05
0.00
-0.05
-0.10
-0.15
-0.20
-0.25
0 5 10 15 20 25 30 35 40 45 50
Time (year)
DX_wellbore
DY_wellbore
DZ_wellbore

APPENDIX III: PREDICTED DISPLACEMENTS FROM THE MODELS WITH/WITHOUT WELLBORES

Appendix III-1: Relative Displacements at N_{CI} and N_{SI}

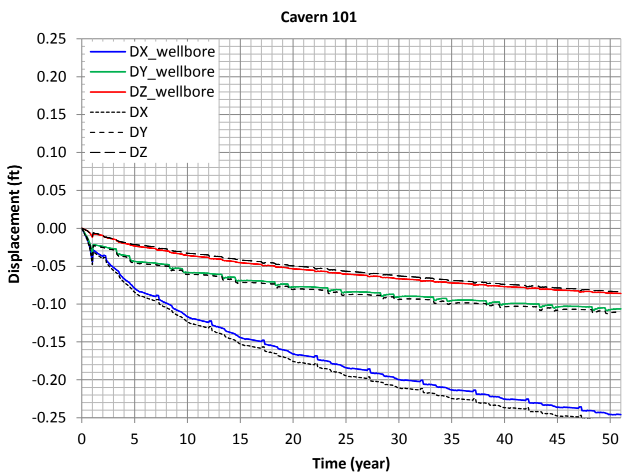

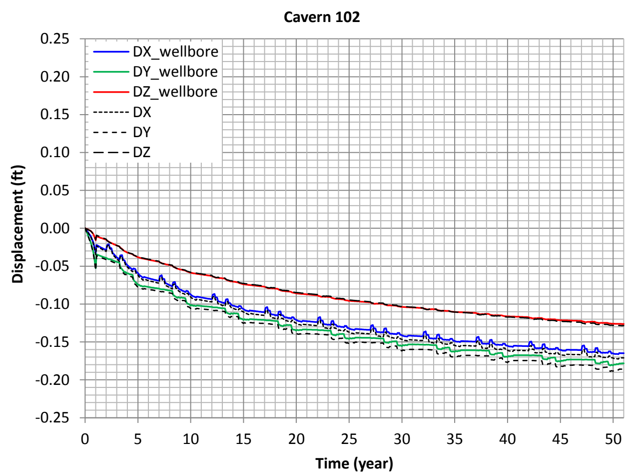

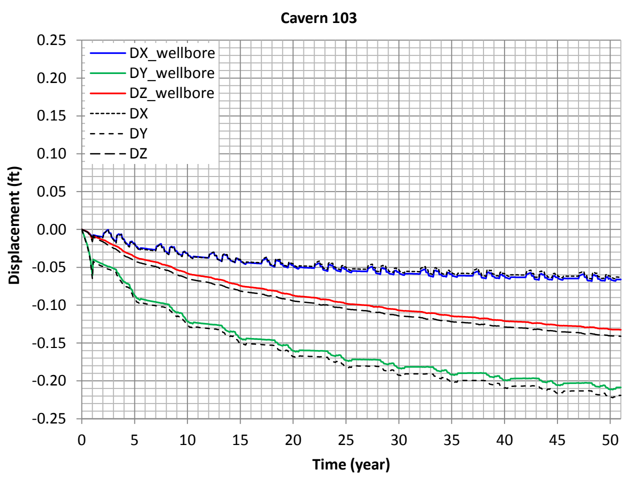

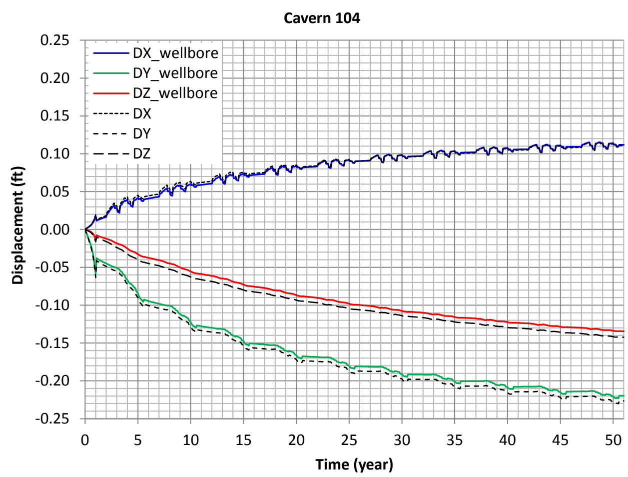

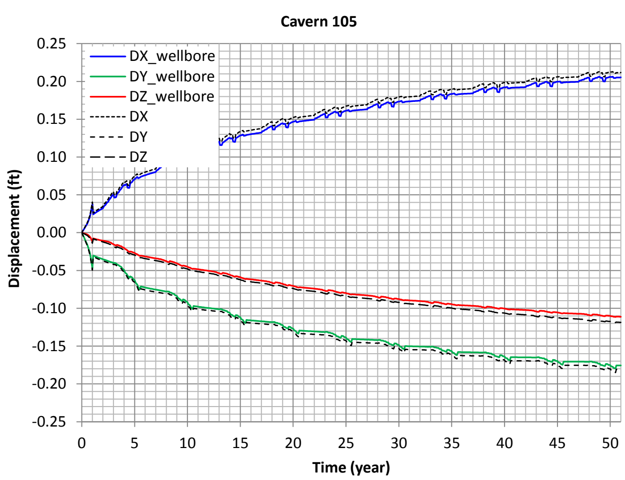

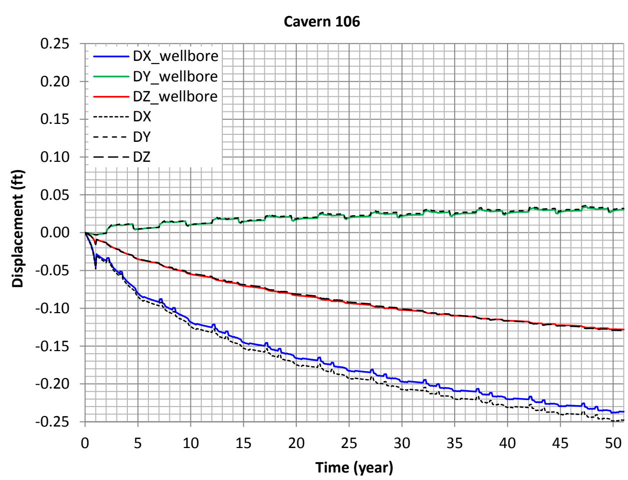

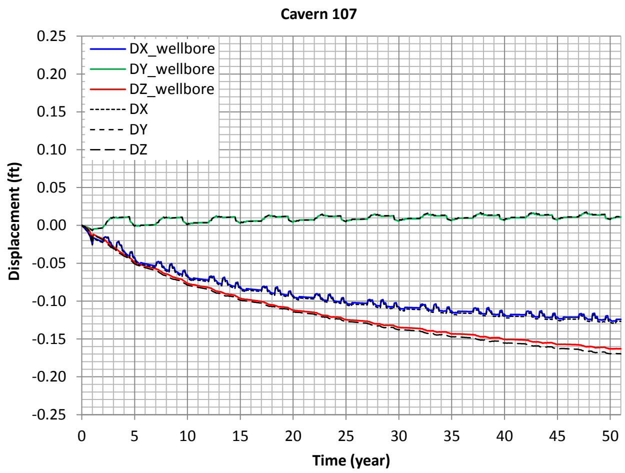
Cavern 107
0.25
0.20
0.15
0.10
0.05
0.00
-0.05
-0.10
-0.15
-0.20
-0.25
Displacement (ft)
0
5
10
15
20
25
30
35
40
45
50
Time (year)
DX_wellbore
DY_wellbore
DZ_wellbore
DX
DY
DZ

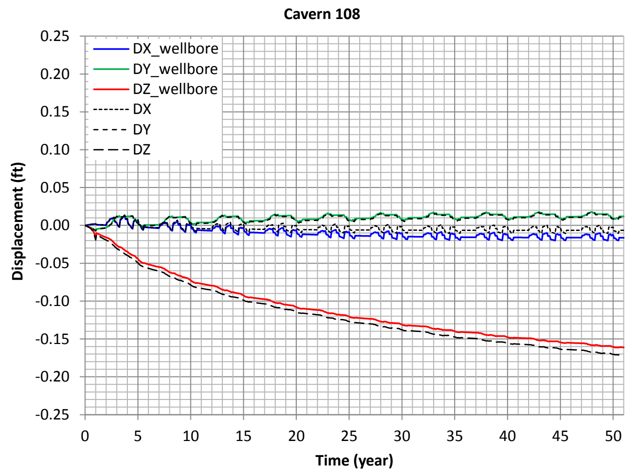
Cavern 108
0.25
0.20
0.15
0.10
0.05
0.00
-0.05
-0.10
-0.15
-0.20
-0.25
Displacement (ft)
0
5
10
15
20
25
30
35
40
45
50
Time (year)
DX_wellbore
DY_wellbore
DZ_wellbore
DX
DY
DZ

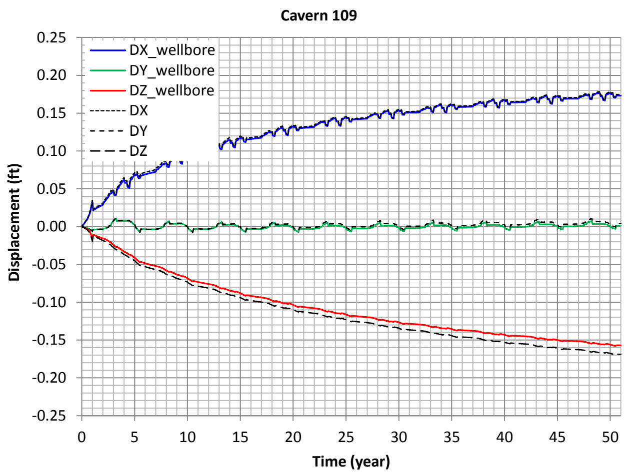
Cavern 109
0.25
0.20
0.15
0.10
0.05
0.00
-0.05
-0.10
-0.15
-0.20
-0.25
Displacement (ft)
0
5
10
15
20
25
30
35
40
45
50
Time (year)
DX_wellbore
DY_wellbore
DZ_wellbore
DX
DY
DZ

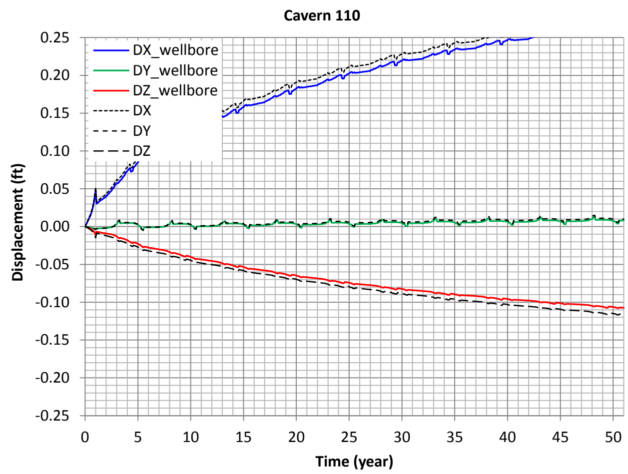
Cavern 110
0.25
0.20
0.15
0.10
0.05
0.00
-0.05
-0.10
-0.15
-0.20
-0.25
Displacement (ft)
0
5
10
15
20
25
30
35
40
45
50
Time (year)
DX_wellbore
DY_wellbore
DZ_wellbore
DX
DY
DZ

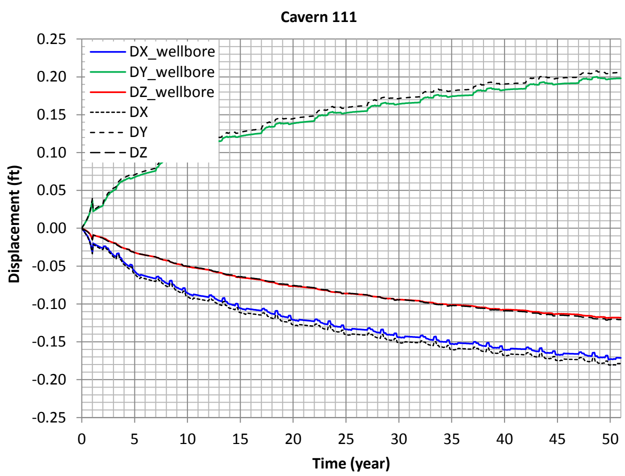
Cavern 111
0.25
0.20
0.15
0.10
0.05
0.00
-0.05
-0.10
-0.15
-0.20
-0.25
Displacement (ft)
0
5
10
15
20
25
30
35
40
45
50
Time (year)
DX_wellbore
DY_wellbore
DZ_wellbore
DX
DY
DZ

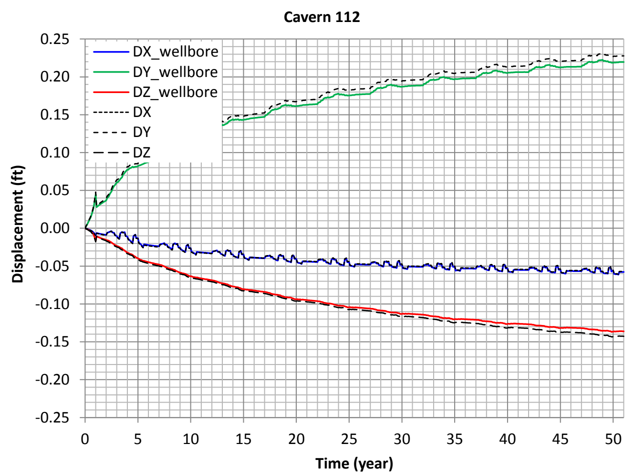
Cavern 112
0.25
0.20
0.15
0.10
0.05
0.00
-0.05
-0.10
-0.15
-0.20
-0.25
Displacement (ft)
0
5
10
15
20
25
30
35
40
45
50
Time (year)
DX_wellbore
DY_wellbore
DZ_wellbore
DX
DY
DZ

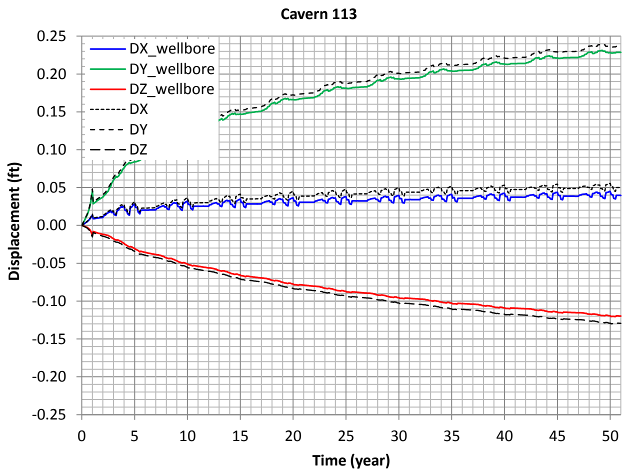
Cavern 113
DX_wellbore
DY_wellbore
DZ_wellbore
DX
DY
DZ
Displacement (ft)
Time (year)
0.25
0.20
0.15
0.10
0.05
0.00
-0.05
-0.10
-0.15
-0.20
-0.25
0
5
10
15
20
25
30
35
40
45
50

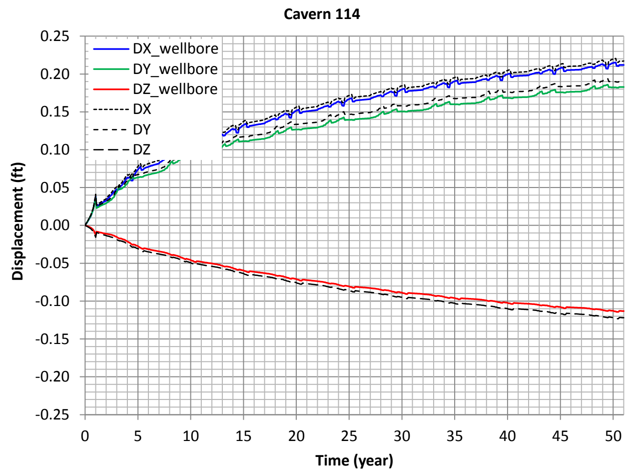
Cavern 114
DX_wellbore
DY_wellbore
DZ_wellbore
DX
DY
DZ
Displacement (ft)
Time (year)
0.25
0.20
0.15
0.10
0.05
0.00
-0.05
-0.10
-0.15
-0.20
-0.25
0
5
10
15
20
25
30
35
40
45
50

Appendix III-2: Relative Displacements at N_{CM} and N_{SM}

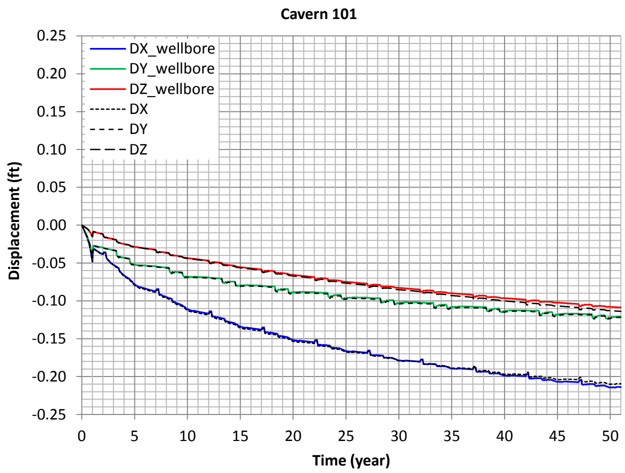

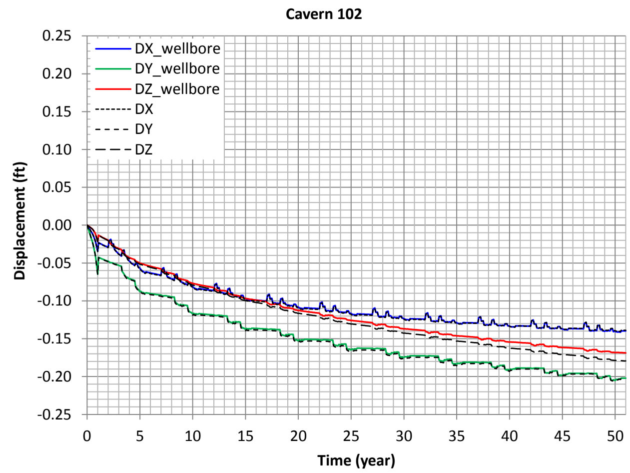

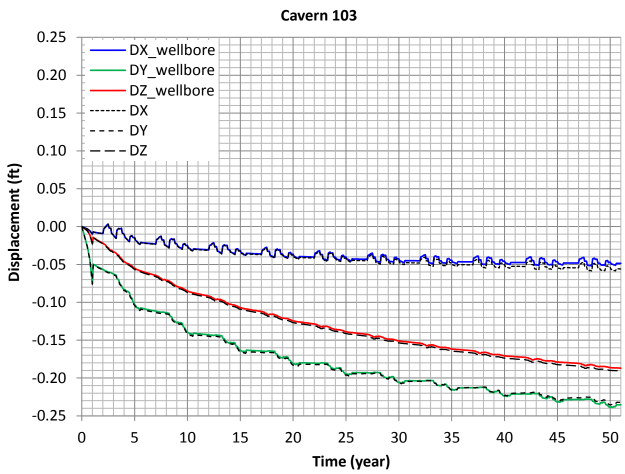

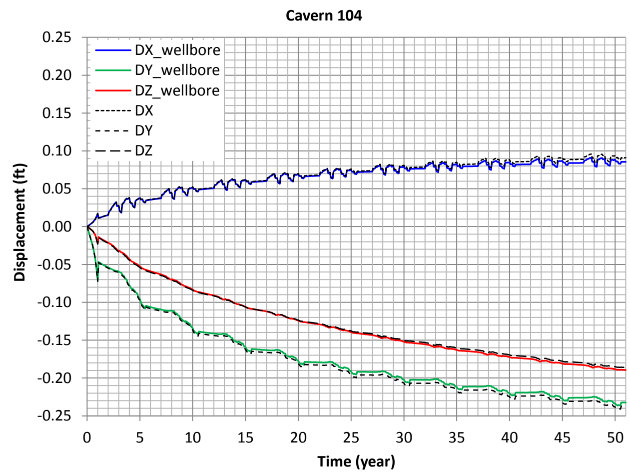

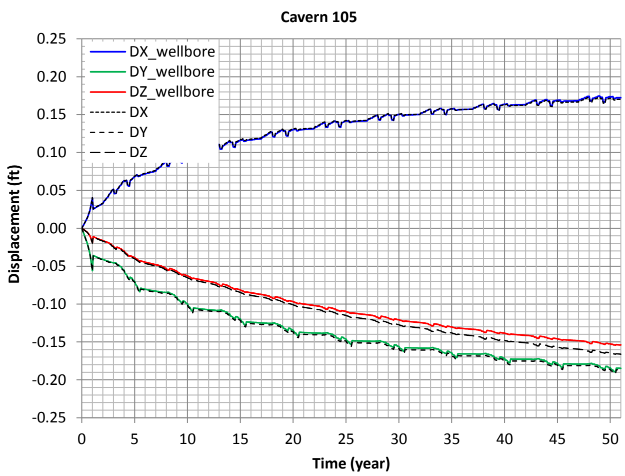

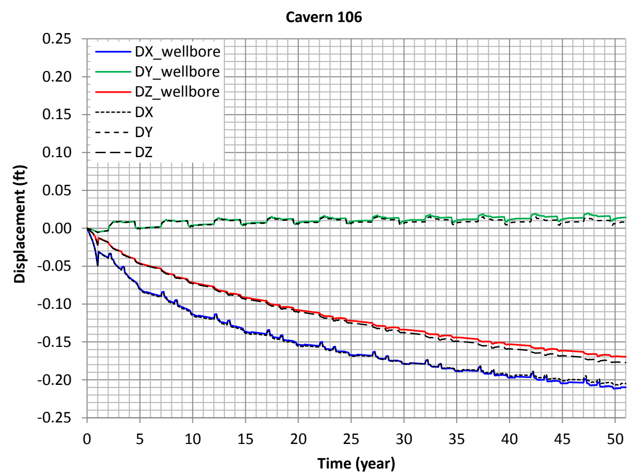

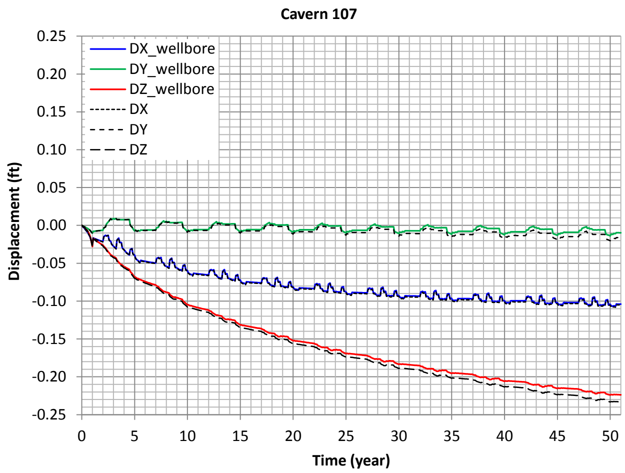
Cavern 107
DX_wellbore
DY_wellbore
DZ_wellbore
DX
DY
DZ
Displacement (ft)
Time (year)

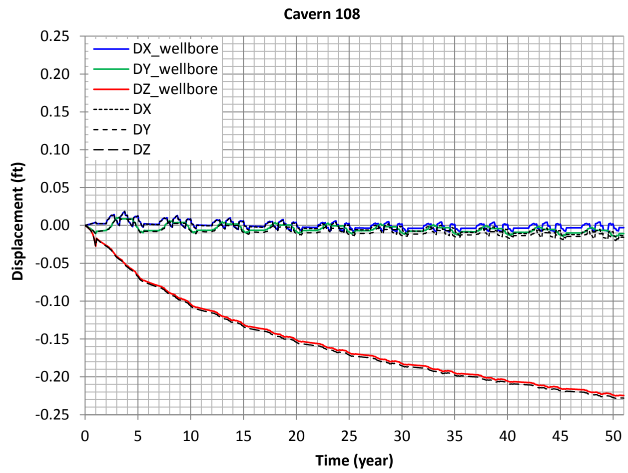
Cavern 108
DX_wellbore
DY_wellbore
DZ_wellbore
DX
DY
DZ
Displacement (ft)
Time (year)

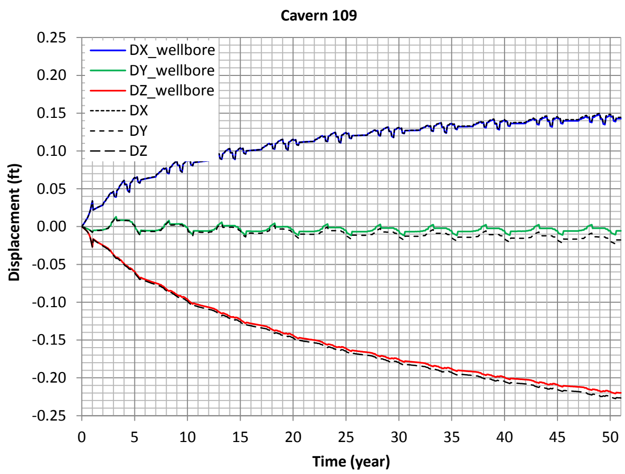
Cavern 109
DX_wellbore
DY_wellbore
DZ_wellbore
DX
DY
DZ
Displacement (ft)
Time (year)

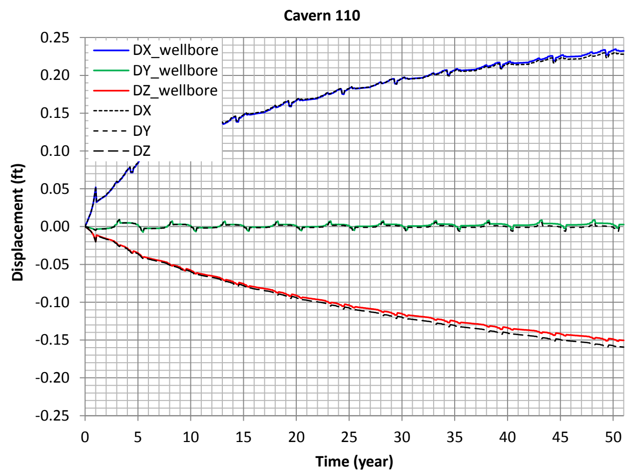
Cavern 110
DX_wellbore
DY_wellbore
DZ_wellbore
DX
DY
DZ
Displacement (ft)
Time (year)

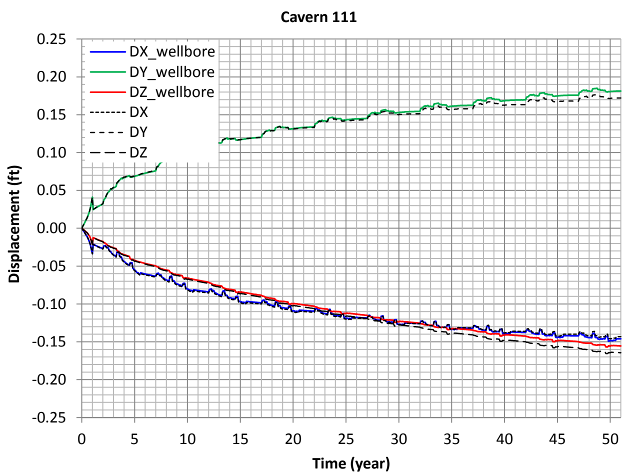
Cavern 111
DX_wellbore
DY_wellbore
DZ_wellbore
DX
DY
DZ
Displacement (ft)
Time (year)

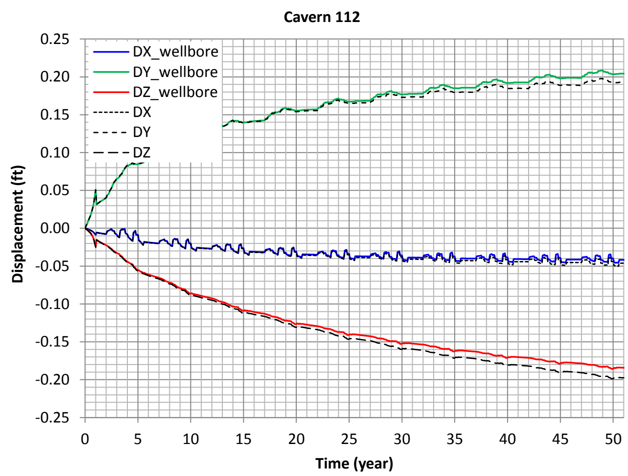
Cavern 112
DX_wellbore
DY_wellbore
DZ_wellbore
DX
DY
DZ
Displacement (ft)
Time (year)

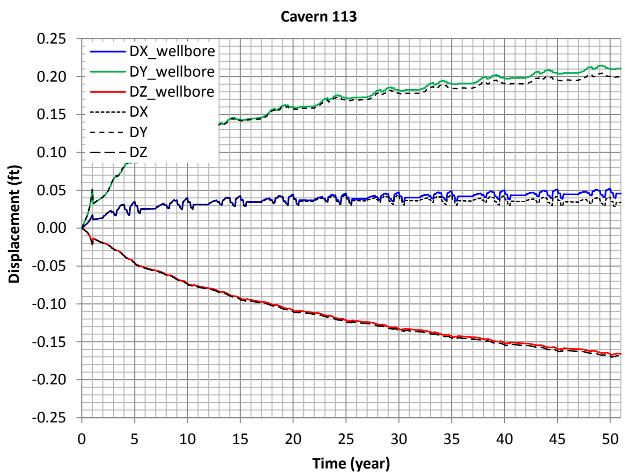
Cavern 113
DX_wellbore
DY_wellbore
DZ_wellbore
DX
DY
DZ
Displacement (ft)
Time (year)

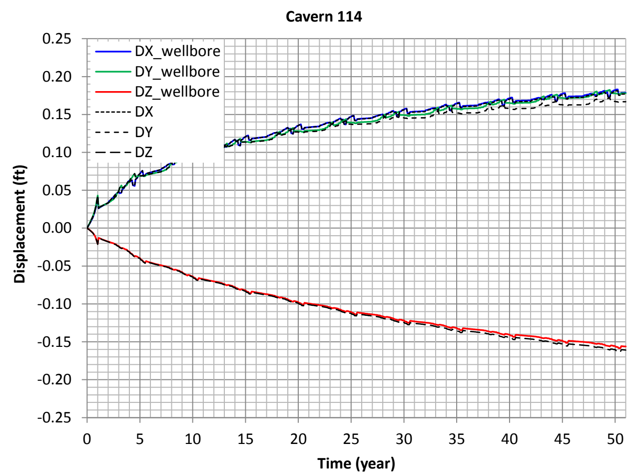
Cavern 114
DX_wellbore
DY_wellbore
DZ_wellbore
DX
DY
DZ
Displacement (ft)
Time (year)

DISTRIBUTION

External Distribution

Electronic copies to:

Wayne Elias (wayne.elias@hq.doe.gov) for distribution to DOE SPR Program Office, Washington, DC

Diane Willard (diane.willard@spr.doe.gov) for distribution to DOE and DM SPR Project Management Office, New Orleans, LA

Sandia Distribution

Print copy				
0	MS0346	M. Nemer	1512	(electronic copy)
0	MS0706	D. K. Rudeen	6211	(electronic copy)
0	MS0706	D. J. Borns	6912	(electronic copy)
1	MS0706	D. L. Lord	6912	(print and electronic copies)
0	MS0706	Anna C.S. Lord	6912	(electronic copy)
0	MS0735	E. K. Webb	6910	(electronic copy)
0	MS0750	G. Bettin	6912	(electronic copy)
0	MS0750	P. D. Weber	6912	(electronic copy)
0	MS0750	K. A. Gutierrez	6912	(electronic copy)
5	MS0750	C. L. Kirby	6913	(print and electronic copies)
1	MS0751	B. L. Roberts	6912	(print and electronic copies)
0	MS0751	M. Y. Lee	6914	(electronic copy)
3	MS0751	B. Y. Park	6914	(print and electronic copies)
1	MS0751	S. R. Sobolik	6914	(print and electronic copies)
0	MS1033	S. J. Bauer	6914	(electronic copy)
1	MS1395	C. G. Herrick	6211	(print and electronic copies)
0	MS0899	Technical Library	9536	(electronic copy)

Sandia National Laboratories